ELECTRONIC PROPERTIES OF II-VI SUPERLATTICES AND III-V TUNNEL STRUCTURES

Thesis by

Yu-shu George Wu

In Partial Fulfillment of the Requirements
for the Degree of
Doctor of Philosophy

California Institute of Technology
Pasadena, California

1988

(Submitted August 3, 1987)

To Lih-Ju

Acknowledgements

I would like to thank Professor T. C. McGill for his guidance during the years I have stayed at Caltech as a member of his research group. I have profited from valuable discussions with Professor McGill regarding my research as well as other aspects of life. I have enjoyed the use of his super facilities, the computer system in partcular, upon which my work constantly depends. I am thankful for his carefully reading of my papers and this thesis and for making numerous useful suggestions. I wish to express my deep gratitude to Vere Snell, who had served the group nicely and efficiently. Many thanks to Carol McCollum and Marcia Hudson for their help in various ways.

I am very grateful to Dr. D. L. Smith of Los Alamos National Laboratory. Dr. Smith is always willing to spend appreciable amount of time to answer my questions. Many discussions with him were quite eye-opening. I have thus learned a lot. I wish to thank him for being an important collaborator in a substantial fraction of my research projects.

I am indebted to Dr. C. Mailhiot of Xerox Webster Research Center. Dr. Mailhiot introduced me to one of the most interesting research area. His frontier theoretical work has been indispensable to my research. I wish to thank him for lots of valuable cooperation.

I also wish to acknowledge Drs. A. R. Bonnefoi, R. T. Collins, R. H. Hauenstein, S. R. Hetzler, A. Prabhakar, T. E. Schlesinger, and A. Zur for valuable discussions. I have also profited from fruitful interactions with W. J. Boudeville, D. H. Chow, M. K. Jackson, M. B. Johnson, R. H. Miles, Y. Rajakarunanayake and T. K. Woodward.

Finally, I would like to thank my family for their constant support and encouragement.

Abstract

This thesis deals with the electronic properties of a semiconductor superlattice and with electronic tunneling in a semiconductor heterostructure. Chapter 2 presents the theoretical formalism of k.p method for calculating band structures for strained-layer superlattices. A strained-layer superlattice is defined as a structure made up of alternating layers of at least two materials with different lattice constants. In this type of superlattice, a uniform strain, instead of misfit defects, accommodates the difference in the lattice constants. A strain affects the band structure since it changes the atomic position, and hence, crystal field which is the sum of all atomic potentials. The realization of strain effects in the model makes possible the understanding of physical properties of strained-layer superlattices, for example, optical properties and transport phenomena, which both are functions of the band structure. The study of ZnTe-CdTe system illustrates interesting strain effects in a strained-layer ZnTe/CdTe superlattice. The ZnTe/CdTe system has potential applications for visible-light sources and photodetectors. Because this system has a large lattice mismatch ($\approx 6\%$), the theoretical study shows that strain plays an important role in optical properties.

Chapter 3 presents the theoretical formalism of k.p method for calculating band structures for semimagnetic semiconductor superlattices. A semimagnetic semiconductor superlattice is defined as a superlattice with one or more constituent materials containing magnetic impurities. When placed in a magnetic field, this type of superlattice exhibits interesting and possibly useful properties such as band gap reduction. These features are associated with the exchange interaction between the itinerant band electrons and localized d electrons on magnetic impurities. The exchange interaction in the theory is included within mean field approximation. Dependences of the band structure on the magnetic field and temperature follow the mean field approximation.

Chapter 4 presents the results of theoretical study of HgTe-CdTe superlattices. The HgTe-CdTe system has interesting features which make it a candidate superior to the HgCdTe alloy for infrared application. Based on the calculated band structure, the optical properties of the HgTe/CdTe superlattice are discussed. The optical absorptions in the superlattice and alloy are studied and compared. It is shown that the superlattice could have absorptions comparable to or larger than those of the alloy. The effects of strain on the optical properties and transport phenomena are discussed. It is found that the transport phenomena may be greatly affected by even a small strain in the HgTe-CdTe superlattice, where the relative difference between the lattice constants is only 0.3%. The optical properties of the HgTe-CdTe superlattice is studied for a wide range of valence band offset which is defined as the valence band edge of HgTe relative to that of CdTe and whose value is currently an unsettled issue. Both the band gap and absorptions of the superlattice are found to decrease rapidly for both negative and large positive values of offset.

Chapter 5 considers the wide-gap $Cd_{1-x}Mn_xTe/Cd_{1-y}Mn_yTe$ superlattice and the narrow-gap $Hg_{1-x}Mn_xTe/Cd_{1-y}Mn_yTe$ superlattices. Currently, the wide-gap system is of great interest because of the possibility of using it as magnetically tunable laser material. In the system spin-splitting is enhanced by the exchange interaction between the localized 3d electrons of Mn^{++} and band electrons. The spin-splitting reduces the band gap opposing to the Landau level shift which enlarges the gap. However, the spin-splitting is found to dominate in the system. In consequence, the band gap decreases in a magnetic field. However, the relative change in the band gap is shown to be small. This makes suspect the idea of fabricating magnetically tunable laser out of this system. Interesting results concerning dependences of magnetic effects on temperature, magnetic field and layer thicknesses are presented. Generally speaking, temperature random-

izes the spin oreintation while magnetic field aligns Mn^{++} spins. In thin-layer limit, the magnetic effect in the superlattice is found to be just that of an alloy corresponding in composition to the superlattice. In contrast, the narrow-gap system is found to have larger tunability. Due to small effective mass of electrons, the Landau level shift is found to be important. Results regarding dependences of magnetic effects on temperature, magnetic field and valence band offset are shown.

Chapter 6 presents the theory and results of electronic tunneling in AlGaAs multi-barrier structures. The observation of negative differential resistance of the structure has been reported. However, basic mechanisms of current conduction in the structure have not been fully understood. We have made study of inelastic electronic tunneling due to electron-phonon coupling in a double-barrier structure. The current induced by the inelastic tunneling of electrons is calculated. The main result is that the inelastic process results in a much larger current than the elastic process at the voltage bias where no resonant tunneling occurs. Dependences of the inelastic contribution on doping level and layer thickness are discussed.

Parts of this thesis have been or will be published under the following titles:

Chapter 2:

Photoluminescence Studies of ZnTe-CdTe Strained-Layer Superlattices,

R. H. Miles, G. Y. Wu, M. B. Johnson, and T. C. McGill, Appl. Phys. Lett. **48**, 1383 (1986).

Chapter 3:

k.p Theory for Semimagnetic Superlattices,

D. L. Smith, G. Y. Wu, T. C. McGill, and C. Mailhiot, in preparation for publication in Phys. Rev. **B**.

Chapter 4:

Optical Properties of HgTe-CdTe Superlattices,

G. Y. Wu, C. Mailhiot, and T. C. McGill, Appl. Phys. Lett. **46**, 72 (1985).

Strain Effects in HgTe-CdTe Superlattices grown on CdTe Substrates,

G. Y. Wu and T. C. McGill, Appl. Phys. Lett. **47**, 634 (1985).

Band Offsets and the Optical Properties of HgTe-CdTe Superlattices,

G. Y. Wu and T. C. McGill, J. Appl. Phys. **58**, 3914 (1985).

Superlattices: Progress and Prospects,

T. C. McGill, G. Y. Wu and S. R. Hetzler, Proceedings of 1985 U. S. Workshop on the Physics and Chemistry of Mercury Cadmium Telluride, J. Vac. Sci. Technol., 2091 (1985).

IR Absorption Measurement and Analysis of HgTe-CdTe Superlattices,

J. P. Baukus, A. T. Hunter and O. J. Marsh, C. Jones, G. Y. Wu, S. R. Hetzler and T. C. McGill, Proceedings of 1985 U. S. Workshop on the Physics and Chemistry of Mercury Cadmium Telluride, J. Vac. Sci. Technol., 2110 (1985).

Chapter 5:

Theoretical Study of the Electronic Properties of Semimagnetic Superlattices,

G. Y. Wu, D. L. Smith, C. Mailhiot, and T. C. McGill, Appl. Phys. Lett. **49**, 1551 (1986).

Theoretical Study of the Electronic Properties of Semimagnetic Superlattices,

G. Y. Wu, D. L. Smith, C. Mailhiot, and T. C. McGill, Proceedings of 1986 U.S. Workshop on the Physics and Chemistry of Mercury Cadmium Telluride, to be published in J. Vac. Sci. Technol. **A**, (1987).

Chapter 6:

Phonon-Assisted Inelastic Tunneling in Double Barrier Structures,

G. Y. Wu and T. C. McGill, in preparation for publication in Solid State Commun.

Contents

Appendices

Chapter 1

Electronic Properties of II-VI Superlattices and GaAs/AlAs Tunnel Structures

1.1 Introduction

Recent advances in crystal growth techniques have made it possible to produce multilayer microstructures such as superlattices and heterostructures. Superlattices are structures made up of alternating layers of materials. Molecular beam epitaxy (MBE) and chemical vapor deposition (CVD) are both popular techniques for growing high quality multi-layer structures. Layers in these structures are a few tens of Å thick. The de Broglie wave length associated with the motion of an electron in such structures is comparable to the layer thickness. Thus quantum size effects are expected to be important in such systems.

Following the pioneering work of Esaki[1], various types of superlattices have been proposed. Their properties are tailorable. The band structure, for example, varies with layer thicknesses. Hence, the band gap, the effective mass, and the optical matrix element are subject to control. Effects on electronic energy levels due to superlattice structure can be pictured by considering a periodic array of quantum wells. In an isolated well, quantization of electronic motion results in a series of discrete levels, which are localized in the well. Localized states contained in adjacent wells can interact with each other, resulting in mini-bands. Thus a few subbands are derived from a single free electron energy band. The subband width primarily depends on the strength of the interaction, which can be controlled by adjusting barrier thickness. The band gap is primarily determined by the size of quantum confinement, which can be varied by changing well width.

In general, semiconductor superlattices are classified into three categories: type-I, type-II, and type-III superlattices, according to relative positions of band edges of constituent materials. In Figure (1.1), we show band diagrams for the three types of superlattices. Relative positions of band edges of constituent materials are plotted. Electronic and optical properties displayed by the three types of superlattices are different.

In a type-I superlattice, both electrons and holes are confined to the same layer. Wave functions of electrons and holes overlap substantially, enhancing radiative recombination rate. A well known example of type-I superlattice is the GaAs/AlAs superlattice. GaAs layers, being energy wells, hold both electrons and holes, while AlAs layers act as barriers and expel free carriers. Due to large overlap of spatial positions, electrons and holes in GaAs layers recombine with ease, resulting in intense radiation. The wavelength of the emitted radiation can be tuned by changing layer thicknesses. The GaAs/AlAs multi-layer structure as lasing device has been an important subject in quantum electronics.

In a type-II superlattice, electrons and holes are separated. An example is the InAs/GaSb superlattice, in which electrons are confined to the InAs layer while holes are confined to the GaSb layer. Wave functions of electrons and

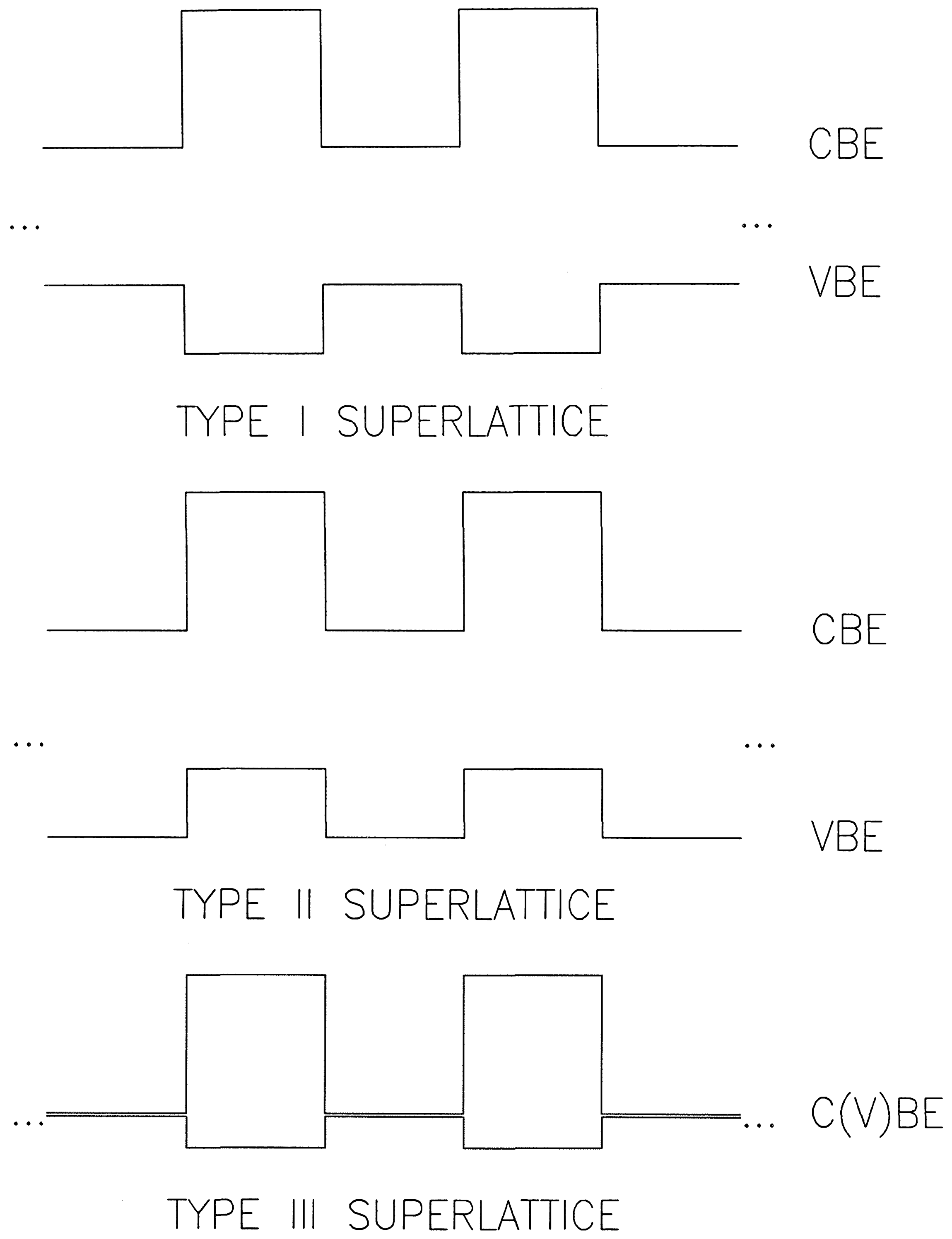

Figure 1.1: Band diagrams. Both conduction and valence band edges of constituent materials are shown for three types of superlattices.

holes do not overlap much. But carriers can be driven to interfaces by an electric field and radiatively recombine there. Hence electroluminescence devices can be made of type-II superlattices. A type-II superlattice may exhibit semiconductor-semimetal transition as layer thicknesses are increased. The InAs/GaSb superlattice is an example. The valence band edge of GaSb is higher in energy than the conduction band edge of InAs. In the limit of thin-layer superlattice, quantum effects seperate conduction subbands from valence subbands. A band gap exists, making the superlattice a semiconductor. On the other hand, in the limit of thick-layer superlattice, the subbands overlap. The band gap vanishes, making the superlattice a semimetal.

A type-III superlattice has a band diagram different from either of the superlattices discussed earlier. One of the constituent materials is semimetallic. The HgTe/CdTe superlattice is an example of type-III superlattice. The HgTe has a zero energy gap. The superlattice has a band gap which, depending on layer thicknesses, varies from zero to the band gap of CdTe. It covers the energy range of infrared light. With wide HgTe and thin CdTe layers, the superlattice has electronic properties similar to those of HgTe. On the other hand, with thin HgTe and wide CdTe layers, it has properties similar to those of CdTe. The HgTe/CdTe superlattice also exhibits semimetal-semiconductor transition.

Constituent materials of most superlattices do not lattice-match. The GaAs/AlAs and the HgTe/CdTe superlattices are examples of nearly lattice-matched superlattices. The relative difference in lattice constant is less than one percent (0.14% for the GaAs/AlAs superlattice and 0.3% for the HgTe/CdTe superlattice). On the other hand, the CdTe/ZnTe superlattices, for example, consist of constituent materials with relatively large lattice constant difference. The relative difference is 6.2%. A lattice-mismatched system may contain misfit defects. However, it could accommodate lattice-mismatch through the formation of a uniform strain. Growth of such systems, called strained-layer superlattices, has been demonstrated. The size of strain can be adjusted to control the band gap[2].

In recent years, semimagnetic semiconductors (SMSCs) as a class of novel materials have raised a lot of interest[3]. Narrow-gap SMSCs such as $Hg_{1-x}Mn_xTe$ and wide-gap SMSCs such as $Cd_{1-x}Mn_xTe$ have been investigated. The Mn^{++} ions contain five $3d$ electrons which are aligned in accordance with the Hund's rule. A 5/2 spin is associated with each Mn^{++} ion. Without the presence of any magnetic field, electronic and optical properties of these systems are similar to the nonmagnetic HgTe and CdTe. The band gap of $Hg_{1-x}Mn_xTe$ or $Cd_{1-x}Mn_xTe$, however, increases with x, the fraction of Mn^{++}. When an external magnetic field is applied, a SMSC displays unique behavior. The localized spins are aligned by the magnetic field. The exchange interaction between a mobile band electron and the net spin may greatly affects the energy of an electronic level. It could be exploited for adjusting optical properties. This is the basic idea behind magnetically tunable devices. With superlattices made of SMSCs, more degrees of freedom are gained for tailoring properties of materials.

To understand electronic properties of superlattices, various methods have been developed. Examples are tight binding method, pseudopotential method, and $\vec{k} \cdot \vec{p}$ theory. Each method has its own advantages. Under certain circumstances, simple calculations are possible. For example, for a GaAs/AlAs superlattice, since conduction and valence bands are well separated in energy, it is justified to use a one-band Kronig-Penny model for obtaining dispersion relations for conduction and valence subbands. However, when the energy separation is small, a multi-band calculation becomes necessary.

In the tight binding method, wave functions are normally expanded in terms of *one s* and *three p* orbitals associated with each atom. A period in the superlattice is envisioned as a large unit cell for which the tight binding Hamiltonian is constructed. This method often has difficulties with getting correct conduction bands. Wave functions of conduction band states obtained are somewhat localized while in reality they spread in space. The effective mass of electrons calculated with tight binding method is usually too large. However, this problem can be avoided by the inclusion of second- or even third-nearest neighbors in the calculation. The tight binding method provides information about electronic properties on atomic scale, such as local density of states. This information is useful for study of defects, surface, and interface.

In pseudopotential calculation, atomic pseudopotentials are used for setting up the Hamiltonian. This method, due to the presence of superlattice periodicity, usually employs lots of plane waves as basis functions for expansion. It requires a powerful computer, particularly in the case of thick-layer superlattices. It has been developed for *ab initio* self-consistent calculation of electronic properties. Relative positions of energy band edges in heterostructures (band offsets) have been so determined. Pseudopotential method also resolves electronic properties on atomic scale, allowing the study of surface and interface properties.

To study the properties of a superlattice, we have developed a theoretical method called superlattice $\vec{k} \cdot \vec{p}$ theory[4]. In this method, band gap and optical matrix element of constituent materials are input parameters, which are determined by fitting optical data. The bulk band structure calculated with these parameters can be used to predict optical properties accurately. It provides effective masses of electrons and holes for bulk materials in better agreement with measured values than tight binding method. It has been extended to deal with band structures for both strained-layer and semimagnetic semiconductor superlattices. In Chapter 2, we present the theory incorporating strain effects. In Chapter 3, we develop the theory for calculating band structures for semimagnetic semiconductor superlattices.

The $\vec{k}\cdot\vec{p}$ theory has been applied to several II-VI superlattice syatems. One in which we may find infrared application is the HgTe-CdTe superlattice. As mentioned early, the HgTe/CdTe superlattice is a type-III superlattice. By adjusting layer thicknesses, its band gap may vary from 0 to $1.6eV$, with the corresponding wavelength covering 8-$14\mu m$, the atomospheric window for the infrared. The HgTe-CdTe superlattice was proposed in late 70's by Schulman and McGill in our group[5]. As pointed out by Smith, McGill, and Schulman, it has advantages not offered by the conventional infrared material, the HgCdTe alloy[6]. The HgCdTe alloy, while capable of infrared absorption, is plagued by some problems. For example, the wavelength cutoff for absorption is sensitive to composition fluctuation produced during growth. Moreover, the leakage current in a p-n junction is increased with decrease in the band gap. The superlattice, on the other hand, has a band gap which varies smoothly with layer thicknesses, allowing a better control of cut-off. The leakage current can be made small by increasing CdTe layer thickness. Thus, the superlattice offers promising features which may advance infrared technology. A detailed discussion of optical properties is provided in Chapter 4 for further assessment of the superlattice.

With band diagram similar to that of a HgTe/CdTe superlattice, the $Hg_{1-x}Mn_xTe/Cd_{1-y}Mn_yTe$ superlattice can be made to have a narrow energy gap. The band gap can be tuned by a magnetic field. It may serve as magnetically tunable infrared material. On the other hand, the $Cd_{1-x}Mn_xTe/Cd_{1-y}Mn_yTe$ superlattice has a large band gap. It has been proposed as lasing device, with wavelength of emission tunable with a magnetic field. In Chapter 5, we present discussions on magnetic effects and optical properties of the two superlattice systems. The theory for calculating band structures of semimagnetic semiconductor superlattices is applied to the two systems.

While electronic properties of a superlattice may be understood with the various energy band theories previously mentioned, a complementary point of view is provided by tunneling theory. Electrons at gap states cannot tunnel very far. On the other hand, those which tunnel with transmission of unity belong to superlattice eigenstates. In reality, due to the presence of defects, scattering occurs. Only a finite number of layers are traversed between two consecutive scattering. Hence, in case a high density of defects exists, a theory of tunneling through a multi-layer structure is more appropriate. However, when the superlattice is sufficiently free of defects, electrons may travel through a number of periods. In that case, tunneling theory merges with energy band theory.

Besides raising scientific interest, multi-layer tunnel structures also offer potential applications. The GaAs/AlAs/GaAs/AlAs/GaAs structure, as negative differential resistance (NDR) device[7,8], has attracted much attention. An explanation on the origin of NDR, based simply on elastic tunneling in which the total energy and the parallel momentum of the electron are both conserved, has been made by Tsu and Esaki[7]. However, the current-conducting mechanism can also be inelastic. This may modify the theory of Tsu and Esaki. To understand the effects of inelastic processes, we have investigated electronic tunneling induced by electron-phonon interaction. In Chapter 6, we present results of study of phonon-assisted inelastic tunneling in the double barrier structure.

In Section (1.2), we will discuss the principle involved in the superlattice $\vec{k}\cdot\vec{p}$ theory. In Section (1.3), introduction to properties of a few II-VI superlattices will be given, which are HgTe/CdTe superlattices, $Hg_{1-x}Mn_xTe/Cd_{1-y}Mn_yTe$ superlattices, and $Cd_{1-x}Mn_xTe/Cd_{1-y}Mn_yTe$ superlattices. In Section (1.4), we will describe concepts involved in electronic tunneling in a double barrier structure.

1.2 Superlattice $\vec{k} \cdot \vec{p}$ Theory

For study of optical properties, $\vec{k} \cdot \vec{p}$ theory is particularly dependable. The method employs perturbation theory. The perturbation consists of $\vec{k} \cdot \vec{p}$ term and the difference in crystal potentials of constituent materials. Wave functions are calculated to the first order and the energy dispersion is evaluated to the second order in the perturbation. When the band gap is large, $\vec{k} \cdot \vec{p}$ theory can be reduced to one-band Kronig-Penny model. When the band gap is small and the coupling between conduction and valence bands is strong, a multi-band model is necessary. However, the principle involved in the superlattice $\vec{k} \cdot \vec{p}$ method is nearly the same as in a one-band Kronig-Penny model. Discussing the one-band calculation serves to illustrate the $\vec{k} \cdot \vec{p}$ theory.

In the Kronig-Penny model, the equation describing the electronic motion is the following:

$$\left[-\frac{\hbar^2}{2m_i^*}\nabla^2 + V_i\right]\psi(\vec{r}) = E\psi(\vec{r}), \tag{1.1}$$

where i labels a constituent material, m_i^* is the effective mass, V_i is the energy band edge, and ψ is the envelope function. Here, the effective mass is assumed to be isotropic. The total wave function Φ is

$$\Phi(\vec{r}) = \psi(\vec{r})u(\vec{r}), \tag{1.2}$$

where $u(\vec{r})$ is the cell-periodic Bloch function, which is assumed to be the same for both constituent materials, i.e., $u_1 = u_2 = u$. The difference in the two Bloch functions complicates the problem. We will address this issue later.

To solve Eq. (1.1), we usually proceed as follows. We take the direction perpendicular to the layer as z-direction. The envelope function is separable. Due to translational symmetry in x and y directions, we write it as

$$\psi = \exp(i\vec{k}_{\|} \cdot \vec{r}_{\|})\psi_z, \tag{1.3}$$

where $\vec{k}_{\|}$ is the parallel component of the wave vector, and ψ_z contains all of z-dependence. When putting Eq. (1.3) in the equation of motion, we get an equation for ψ_z, the perpendicular component of the envelope function. We give the equation for ψ_z in the following:

$$-\left[\frac{\hbar^2}{2m_i^*}\frac{d^2}{dz^2}+V_i\right]\psi_z=\left(E-\frac{\hbar^2 k_{\|}^2}{2m_i^*}\right)\psi_z. \tag{1.4}$$

The equation obviously has solutions in the form of $\exp(ik_z z)$. Normally in a bulk crystal without any boundary, k_z with complex value is not allowed. Only solutions with real k_z satisfy the Born-von Karman boundary condition. However, in a superlattice, the bulk solutions do not have to be freely propagating, due to the presence of interfaces. In other words, complex as well as real k_z are allowed.

The way the above equation is solved is different from that normally taken in the calculation of a bulk band structure. To calculate a bulk band structure, we select a real Bloch vector $\vec{k}$ first, and then solve the Hamiltonian equation for the energy E. However, in the superlattice problem, we input an energy and a $\vec{k}_{\|}$ and solve for generally complex k_z.

Having solved the equation for ψ_z, ψ_z is expressed as a linear combination of the bulk solutions, propagating or evanescent. We need to connect the envelope function across the interface. This has been an interesting subject in heterojunction problem. One set of boundary conditions which have been often used are the continuity of the envelope function and the current at the interface. That is,

$$\psi_z, \qquad -\frac{i\hbar}{2m_i^*}\left(\psi_z^*\frac{d\psi_z}{dz}-\psi_z\frac{d\psi_z^*}{dz}\right) \tag{1.5}$$

are continuous. Or equivalently,

$$\psi_z, \qquad \frac{1}{m_i^*}\frac{d\psi_z}{dz} \tag{1.6}$$

are continuous. The boundary condition involving the derivative can also be obtained by integrating the equation for ψ_z (Eq. (1.4)) across the interface.

Since a superlattice displays translational symmetry in z-direction, we can associate with that a quantum number q, which is the z-component of the wave vector. The Bloch condition states that

$$\psi(z+d) = \exp(iqd)\psi(z), \tag{1.7}$$

where d is the superlattice periodicity. With both boundary conditions and Bloch condition, the energy dispersion $E(\vec{k}_{\|}, q)$ can be established.

Having illustrated basic principles involved in superlattice $\vec{k}\cdot\vec{p}$ theory, we now address the issue regarding the difference in the Bloch functions. In a first-order calculation, it is legitimate to neglect the difference. However, to calculate the energy dispersion to a higher order, the inclusion of the difference is necessary. The difference in the Bloch functions for constituent materials can be attributed to the difference in their crystal potentials. Pseudopotential calculation, which gives the Bloch functions explicitly, helps to handle this problem. The information so obtained is used as input for $\vec{k}\cdot\vec{p}$ calculation.

As strain effects are present, the $\vec{k}\cdot\vec{p}$ Hamiltonian is modified. In a strained-layer superlattice, the presence of strain does not change the symmetry of the superlattice. Each electronic state is labeled by k_x, k_y, and k_z as for an unstrained crystal. However, band edges of constituent materials and dispersion relations are changed. These changes can be described by deformation potentials. In Chapter 2, we will show how the $\vec{k}\cdot\vec{p}$ Hamiltonian is modified and how the difference in the Bloch functions is taken into account. The strained-layer CdTe/ZnTe superlattice will be taken as an example to illustrate strain effects.

On the other hand, when magnetic effects are introduced, fundamental modification of band structure is induced. Landau levels are formed. The quantum numbers for labeling each bulk eigenstate are k_x, N, and k_z. Here, N is the

Landau level index. In Chapter 3, we will show how to set up the effective-mass equation for the envelope function. We will elaborate to modify the current continuity condition. Some of the derivations will be included in Appendix A.

1.3 II-VI superlattices

In this section, we will discuss properties of several II-VI superlattices which make them uniquely suitable for some applications. The discussion on HgTe/CdTe superlattices will center on optical properties. We will look into the potential of $Hg_{1-x}Mn_xTe/Cd_{1-y}Mn_yTe$ superlattice as the magnetically tunable version of the HgTe/CdTe superlattice. We will discuss another semimagnetic system, the $Cd_{1-x}Mn_xTe/Cd_{1-y}Mn_yTe$ superlattice, which was proposed for use as magnetically tunable laser.

The potential of the HgCdTe alloy and the HgTe/CdTe superlattice as infrared materials is attributed to unique band structures of HgTe and CdTe. The CdTe is a wide-gap semiconductor. The valence band states at the zone center (Γ point) of the Brillouin zone are four-fold degenerate. Two of them are heavy-hole states and the other two are light-hole states. The conduction band states are two-fold degenerate. The two conduction band states are primarily derived from *s* orbitals of Cd while the four valence band states are primarily derived from *p* orbitals of Te. Under the operation of the tetrahedral group, these degenerate states transform within the subspace of functions they form. The valence band states constitute a basis for Γ_8 irreducible representation of the tetrahedral group. The conduction band states form a basis for the Γ_6 representation.

On the other hand, the HgTe is a semimetal. Symmetries in HgTe band structure are inverted. The valence band and the conduction band are degenerate at Γ point, both belonging to Γ_8 representation, while Γ_6 states which are s-like are lower in energy. The inversion of symmetry results in a negative $\Gamma_6 - \Gamma_8$ gap. Hence, within virtual crystal approximation, the HgCdTe alloy may have a $\Gamma_6 - \Gamma_8$ band gap, negative or positive depending on its composition. The band gap can be tuned for infrared detection. By forming superlattice structures, it is also possible to obtain band gap suitable for infrared application.

To study optical properties, an important parameter is $\epsilon_2(\omega)$, the imaginary part of the dielectric function, since it determines optical absorption. The calculation of $\epsilon_2(\omega)$ forms a major part of Chapter 4. Optical properties are functions of band structure. The valence band offset, describing the relative positions of valence band edges of constituent materials on the energy scale, is an important parameter which determines the band structure. This parameter has not been pinned down yet for HgTe/CdTe superlattices. Another factor which affects the band structure is the presence of strain, which is due to lattice mismatch in the HgTe/CdTe system. In Chapter 4, we examine variations in electronic properties of this system induced by effects of strain and change in band offset.

The $Hg_{1-x}Mn_xTe/Cd_{1-y}Mn_yTe$ superlattice is the magnetic version of the HgTe/CdTe superlattice. This semimagnetic superlattice also has a band gap which covers the range of infrared light. The band gap of this system can be adjusted by changing layer thicknesses as well as applying a magnetic field. In the presence of a magnetic field, Landau levels are formed. More importantly, the localized Mn^{++} spins are partly aligned by the field. A nonzero net spin is established. The exchange interaction between the aligned spins and an itinerant band electron, lifting spin degeneracy, splits energy levels. This effect can be represented by introducing an equivalent internal magnetic field. Magnetic effects are magnified through the internal field. Mean field theory can be used to relate the internal field to the external one. There are other factors affecting the internal magnetic field. Thermal effects, for example, which tend to randomize the orientations of localized magnetic moments, decrease the internal field. It is also possible to tune magnetic effects by changing Mn^{++} composition. Increasing the composition enhances the internal field. However, the Mn^{++} ions in a SMSC are antiferromagnetically coupled. With large Mn^{++} composition, the alignment of moments is reduced by the antiferromagnetic coupling.

The band gap of a semimagnetic superlattice varies with Landau level shift and spin-splitting. Landau level shift tends to enlarge the band gap, while spin-splitting tends to reduce the band gap. Enhanced by the exchange interaction, spin-splitting usually dominates. A central issue in the application of semimagnetic superlattices is the magnitude of the relative change in the band gap, achievable with a currently available magnetic field, which is on the order of a few Tesla. In Chapter 5, we discuss the tunability of the band gap by a magnetic field for the $Hg_{1-x}Mn_xTe/Cd_{1-y}Mn_yTe$ superlattice. In this system, the electron has a small effective mass, resulting in a large Landau level shift.

The $Cd_{1-x}Mn_xTe/Cd_{1-y}Mn_yTe$ superlattice can emit intense radiation with energy above $1.6eV$, the band gap of CdTe. The constituent material which has the smaller band gap acts as energy well for both electrons and holes. Both types of carriers are trapped there. Radiative recombination of free carriers can be made intense enough for the structure to lase. The energy of the emission depends on the strength of the external magnetic field, which affects the energy levels. In this system, with large electron effective mass, the Landau level shift is small. The band gap is reduced primarily due to enhanced spin-splitting. In Chapter 5, we will look into the $Cd_{1-x}Mn_xTe/Cd_{1-y}Mn_yTe$ superlattice for its potential as magnetically tunable lasing material.

1.4 GaAs/AlAs Tunnel Structures

In this section, we discuss the concepts involved in the tunneling theory. Discussion will be concentrated on the GaAs/AlAs/GaAs/AlAs/GaAs structure. In such a structure, the middle GaAs layer is energetically preferable to electrons, while the AlAs layers are energy barriers. This results in quantization of electronic motion perpendicular to the layers. There are eigenstates with energies less than the barrier height and primarily localized in the GaAs well.

Electronic tunneling through a double barrier structure can be classified into elastic and inelastic processes. In an elastic process, both the energy and the parallel component of momentum are conserved. If either one of them is changed, it is an inelastic process. In Fig. (1.2), we illustrate both processes. The inelastic process shown in the figure creates a phonon in the barrier. Other types of inelastic tunneling are also possible. Plasmons or other elementary excitations can be excited during tunneling. Impurities can scatter tunneling electrons too.

For an electron impinging onto the structure, the transmission coefficient is normally exponentially small. The propagation of the wave in each barrier is characterized by an imaginary wave vector

$$i\kappa = i\frac{\sqrt{2m^*(V - E_l)}}{\hbar}, \tag{1.8}$$

where V is the barrier height, and E_l is the energy associated with the longitudinal motion of the electron. The wave is attenuated by $\exp(-\kappa d)$ in traversing through each barrier, where d is the barrier thickness. But the transmission is near unity when the energy of the electron coincides with one of the quasi-bound levels. When the device is so biased that a quasi-bound level is aligned with the Fermi sea in the GaAs electrode, a large tunneling current is produced. With a deviation from such a bias, the current drops very rapidly. This results in NDR.

In inelastic tunneling, even when the Fermi sea is not aligned with any quasi-

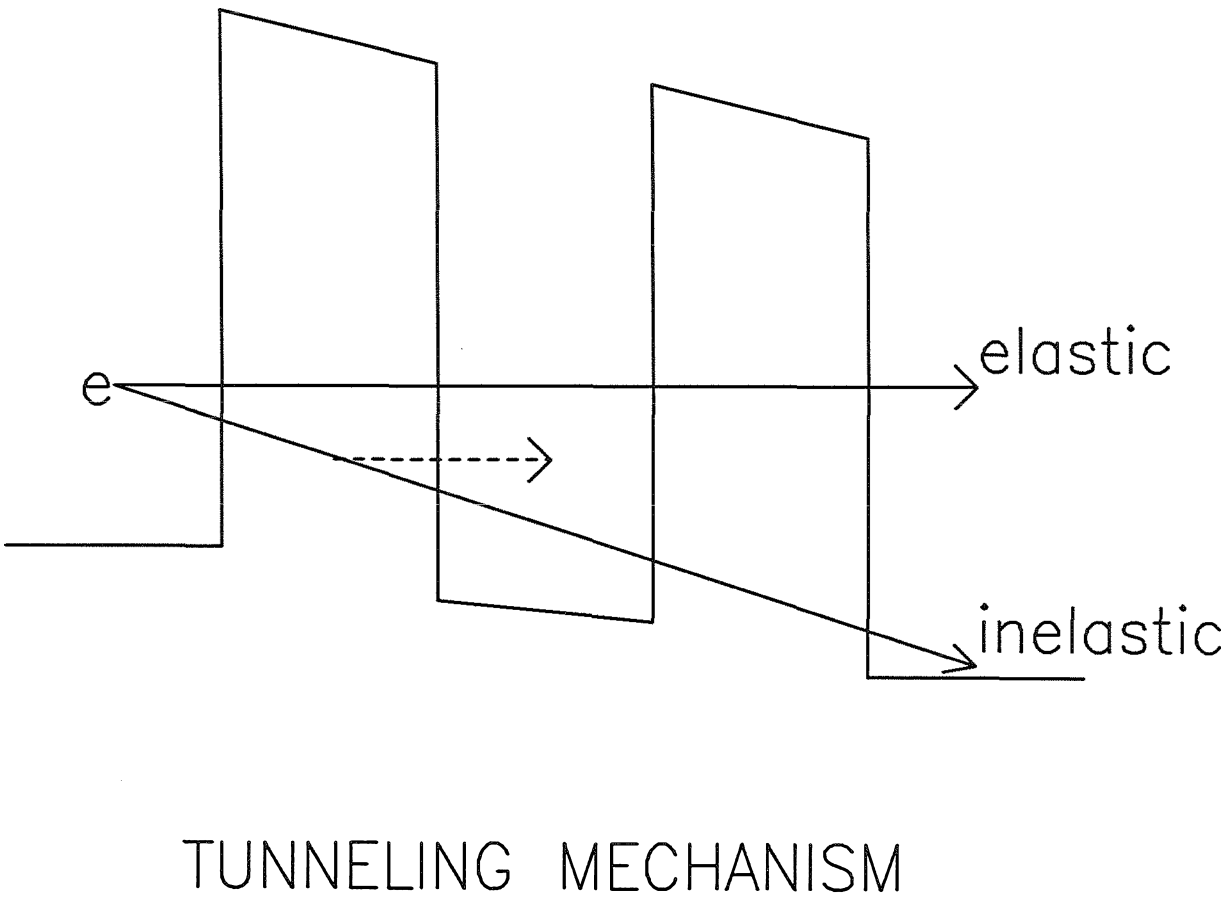

Figure 1.2: Tunneling mechanisms in a double barrier structure. Both elastic and inelastic processes are shown.

bound level, electrons injected into the GaAs well may still utilize the levels as channels for tunneling, thus enhancing the current. The tunneling electron can excite an optical or acoustical phonon through electron-phonon coupling. A longitudinal acoustical (LA) phonon, for example, deforms the crystal globally and, hence, changes the crystal field. This results in the deformation potential coupling between an electron and a LA phonon. Similarly, an longitudinal optical (LO) phonon can set up a dipole field which acts on the electron. This polar coupling is much stronger than other types of electron-phonon interaction. Inelastic tunneling decreases the peak to valley ratio characterizing the current-voltage curve predicted by Tsu-Esaki model.

The Transfer Hamiltonian method is well suited for calculations of inelastic tunneling. For a single barrier structure, electrons are viewed as quasi-particles confined to the two regions separated by the barrier. The quasi-particle states are not stationary states. Their amplitudes decay with time, since they can tunnel from one side to the other side of the barrier. The transition rate is determined by Fermi's golden rule. The transmission is proportional to the overlap in the barrier of wave functions of the initial and the final states in the tunneling process. The validity of the method lies in the fact that the transimission is small. In Chapter 6, we will employ transfer Hamiltonian method to analyze phonon-assisted tunneling and illustrate the importance of inelastic tunneling in the double barrier problem. Derivations of expressions for currents are presented in Appendix B.

1.5 Summary of Thesis

In Chapter 2, we will develop the superlattice $\vec{k}\cdot\vec{p}$ theory for strained-layer superlattices. Two versions of the theory will be given: first-order and second-order theories. In the first-order theory, analytical dispersion relations are given for superlattice subbands. This theory allows us to study the energy gap as a function of layer thicknesses and, hence, is of importance to superlattice engineering. In the other version, a numerical method is required for evaluation of the band structure. However, the difference in Bloch functions is taken into account and energy dispersion is obtained to a higher order of accuracy. Band structures of strained CdTe, strained ZnTe, and strained-layer CdTe/ZnTe superlattices will be calculated as examples. Transport properties are compared for unstrained and strained cases and qualitative difference is shown to be likely induced by the strain. It is found that the strain in the ZnTe pushes the light-hole band upwards, while in the CdTe it pulls the light-hole band downwards. As a result, the band diagram for a CdTe/ZnTe superlattice may vary, the change depending on layer thicknesses of CdTe and ZnTe. This produces a discontinuous dependence of band gap on layer thicknesses.

In Chapter 3, the $\vec{k} \cdot \vec{p}$ theory for semimagnetic semiconductor superlattices will be presented. The exchange interaction between localized magnetic moments and band electrons is treated within mean field theory. Effective-mass equation is derived for envelope functions. Boundary conditions are established. The eigenvalue equation for superlattice wave function is derived. As applications, band structures of $Cd_{1-x}Mn_xTe$ and $Hg_{1-x}Mn_xTe/Cd_{1-y}Mn_yTe$ superlattices are calculated. Spin-splitting in the energy band structure due to exchange interaction is shown. Complex structure in the band structure is illustrated.

In Chapter 4, we present discussions on electronic properties of HgTe/CdTe superlattices. $\epsilon_2(\omega)$ for superlattices and alloys are calculated and compared. We also study effects on optical properties induced by a variation in the valence band offset. Strain in the superlattice is included in the calculation of band structures. Optical properties are compared for unstrained and strained superlattices. It is found that the superlattice may have absorptions comparable to or larger than those for the alloy. Strain effects are shown to be unimportant for optical properties. However, they may push the light-hole subband upwards and induce large conductivity. The band gap is near maximum at zero valence band offset. Optical absorptions are found to be insensitive to variation in the valence band offset. However, absorption decreases very rapidly as the valence band edge of HgTe becomes lower than that of CdTe. This is attributed to the occurrence of separation of electrons and holes.

In Chapter 5, electronic properties of $Hg_{1-x}Mn_xTe/Cd_{1-y}Mn_yTe$ and $Cd_{1-x}Mn_xTe/Cd_{1-y}Mn_yTe$ superlattices are discussed. Magnetic effects, including their temperature and layer thickness dependence, are shown. Variations in the band gap due to Landau level shift and spin-splitting are compared. Relative change in band gap with a large magnetic field at a low temperature is calculated for both systems. For $Hg_{1-x}Mn_xTe/Cd_{1-y}Mn_yTe$ superlattices, we also show magnetic effects as functions of the valence band offset. It is found that the presence of a magnetic field reduces the band gap. The relative change in the band gap is 2.5% for the $Cd_{1-x}Mn_xTe/Cd_{1-y}Mn_yTe$ system and 10% for the $Hg_{1-x}Mn_xTe/Cd_{1-y}Mn_yTe$ system. The reduction in the band gap is attributed to spin-splitting, which is enhanced by exchange interaction. The Landau level shift, although unimportant, is found to be larger in the $Hg_{1-x}Mn_xTe/Cd_{1-y}Mn_yTe$ system than in the other system. This is attributed to the light effective mass of electron. Magnetic effects are found to decrease with an increase in temperature for both systems.

In Chapter 6, we first discuss shortly the theory for elastic tunneling. Order of magnitude estimates are made for the peak to valley ratio. Inelastic tunneling assisted by barrier phonons is studied with transfer Hamiltonian method. Two representative types of coupling are considered: a strong one which is polar optical coupling between electrons and logitudinal optical phonons, and a weak one which is deformation potential coupling between electrons and longitudinal acoustical phonons. We also show J_{res}/J_{off}, the ratio of currents at and off resonance. This ratio is calculated with and without the inclusion of phonon-assisted tunneling. The dependence of this ratio is also studied as a function of the doping level at the electrode. Polar coupling is shown to induce a much larger current than deformation potential coupling. The ratio of currents is found to be changed by orders of magnitude by inelastic tunneling. However, it is relatively insensitive to variation in doping level at the electrode.

References

1. L. Esaki and R. Tsu, IBM J. Res. Develop. **14**, 61 (1970).
2. G. C. Osbourn Phys. Rev. **B 27**, 5126 (1983).
3. J. K. Furdyna, J. Vac. Sci. Technol. **A4**, 2002 (1986).
4. D. L. Smith, and C. Mailhiot, Phys. Rev. **B 33**, 8345 (1986).
5. J. N. Schulman and T. C. McGill, Appl. Phys. Lett., **34**, 663 (1979).
6. D. L. Smith, T. C. McGill, and J. N. Schulman, Appl. Phys. Lett., **43**, 180 (1983).
7. R. Tsu and L. Esaki, Appl. Phys. Lett., **22**, 562 (1973).
8. L. L. Chang, L. Esaki, and R. Tsu, Appl. Phys. Lett., **24**, 593 (1974).

Chapter 2

$\vec{K} \cdot \vec{P}$ Theory of Band Structures of Strained-Layer Semiconductor Superlattices

2.1 Introduction

2.1.1 Background

In this chapter we present $\vec{k} \cdot \vec{p}$ method of calculating band structures of *strained-layer semiconductor superlattices.* Strained-layer superlattices are made up of alternating layers of semiconducting materials which are lattice-mismatched. Lattice-mismatch either can cause misfit defects in the superlattice or can be accomodated by forming an uniform strain in each individual layer. It is the latter which we will be considering in the chapter. Technically, there is always some lattice-mismatch in a superlattice whose composition varies spatially. In GaAs/AlAs and HgTe/CdTe superlattices, the relative difference between lattice constants of constituent materials is a few thousandths (0.14% for GaAs/AlAs superlattices and 0.3% for HgTe/CdTe superlattices). In CdTe/ZnTe superlattices, the lattice mismatch is about 6.2%.

A strain in the crystal changes atomic positions and, hence, changes the crystal potential. The change in the crystal potential, in turn, changes the energy band structure. Bardeen has proposed the idea of using deformation potentials for describing strain effects. The change in the conduction band edge is described by

$$\delta E_c = a\Delta \tag{2.1}$$

under hydrostatic stress, where Δ is volume dilation, and a is the change in the conduction band edge per unit dilation and is called the deformation potential. Similar equations hold for valence band edges. When shear stress is also present, more deformation potential parameters are used to represent strain effects. They are all on the order of a few electron volts. We can make order of magnitude estimate of strain effects in GaAs/AlAs or HgTe/CdTe superlattices. Since the strain components are a few thousandths, the change in the bulk band structure is, from Eq. (2.1), on the order of a few milli-electron volts, compared to the band gap which is on the order of one electron volt. On the other hand, a relatively large strain is present in the CdTe/ZnTe superlattice. The change in the bulk band structure is on the order of a few tens of milli-electron volts. Strain effects in CdTe/ZnTe superlattices are thus bigger than those in GaAs/AlAs or HgTe/CdTe superlattices.

In either case, strain could play an important role in transport phenomena in the superlattice. Generally speaking, the presence of strain not only shifts edges of conduction and valence bands, but it could also invert relative positions of heavy-hole-like and light-hole-like valence bands under certain circumstances. In ordinary zinc-blende semiconductors, valence bands contain light-hole bands and heavy-hole bands, which are degenerate at the zone center. However, the degeneracy could be lifted by the application of stress. For example, an uniaxial compression pushes the light-hole band upwards above the heavy-hole band, while an uniaxial tension pushes the heavy-hole band upwards above the light-hole band. This could have important effects on transport phenomena. When the crystal is unstrained, holes occupy largely the heavy-hole band at low temperature. However, as an uniaxial compressive stress is applied, majority carriers become light-hole-like, causing a relatively large conductivity. On the other hand, when an uniaxial tensile stress is applied, majority carriers are heavy-hole-like, causing a relatively small conductivity. Thus, the application of a stress could significantly alter the conductivity.

Optical properties of a direct gap semiconductor, however, are not necessarily sensitive to the occurrence of strain. Let us take absorption for example. Absorption function α is defined by

$$I(z) = I_0 \exp(-\alpha z), \tag{2.2}$$

where I_0 is the intensity of the incident light, and $I(z)$ is the intensity of light after traversing a depth of z. The absorption at a certain frequency ω is, roughly speaking, proportional to $D(\hbar\omega)$, i.e.,

$$\alpha(\omega) \propto D(\hbar\omega),$$

where $D(\hbar\omega)$ is the number of pairs of states per unit energy (i.e., joint density of states) available as initial and final states to the direct electronic transition

$$\epsilon_v(\vec{k}) \rightarrow \epsilon_c(\vec{k}) = \epsilon_v(\vec{k}) + \hbar\omega. \tag{2.3}$$

Here, ϵ_v and ϵ_c are the energies of conduction and valence bands at $\vec{k}$, a general point in the reciprocal space. Joint density of states depends, in turn, on band structure over the full Brillouin zone.

In the presence of strain, an energy band is shifted more or less rigidly, at least so near the zone center, since strain-induced change in a band is a smooth function of $\vec{k}$. Joint density of states, being a function of band structure, is shifted as rigidly in energy near the onset (i.e., $E \sim E_g$).

The situation can be best explained in the zero-order approximation, in which energy bands can be taken as parabolic, that is,

$$\begin{aligned} \epsilon_c &= \frac{\hbar^2 k^2}{2m_c}, \\ \epsilon_v &= -\frac{\hbar^2 k^2}{2m_v}. \end{aligned} \tag{2.4}$$

Joint density of states per unit volume is, in the approximation, given by (counting spin degeneracy)

$$\begin{aligned} D(E = \hbar\omega) &= \frac{1}{4\pi^3} \int d^3k \delta \left[\epsilon_c(\vec{k}) + \delta E_c - \epsilon_v(\vec{k}) - \delta E_v - E\right] \\ &= \frac{1}{2\pi^2} (\frac{2m^*}{\hbar^2})^{3/2} \left[E - \epsilon_c(\vec{k} = 0) - \delta E_c + \epsilon_v(\vec{k} = 0) + \delta E_v\right]^{1/2} \end{aligned}$$

under hydrostatic stress, where

$$\frac{1}{m^*} \equiv \frac{1}{m_c} + \frac{1}{m_v}. \tag{2.5}$$

Hence,

$$D_{strained}(\hbar\omega) = D_{unstrained}(\hbar\omega - \delta E_c + \delta E_v). \tag{2.6}$$

Density of states is shifted in energy. So is absorption function near its on-set:

$$\alpha_{strained}(\hbar\omega) = \alpha_{unstrained}(\hbar\omega - \delta E_c + \delta E_v). \tag{2.7}$$

A currently interesting subject is the critical thickness for which a strained-layer superlattice can be grown. From physical considerations, the thickness of the strained-layer superlattice possesses an upper limit. Strain-induced elastic energy increases linearly with the thickness of superlattice. Beyond a certain thickness, misfit defects start to take over uniform strain to lower the energy of the structure. The structure then contains both strain and defects. There have been several theories on critical thickness for growth of a strained epilayer.

However, a theory capable of predicting critical thickness of a strained-layer superlattice has not been satisfactorily developed. We shall not address this issue further except to note that strained-layer superlattices with high quality have indeed been grown, with thickness beyond the critical limit predicted for strained epilayer growth.

The inclusion of strain effects in the theory of superlattice band structures is very important. The theory to be developed here is capable of predicting effects of strain on electronic properties. It is also helpful to data analysis. Photoluminescence measurement, for instance, has been performed with CdTe/ZnTe superlattices[7]. The developed theory has been used to interpret the data[7].

There are several versions of $\vec{k} \cdot \vec{p}$ theory of superlattice band structures. In the chapter we are going to present two of them. One has the analytic capability while the other one is more accurate.

2.1.2 Outline of the Chapter

The $\vec{k} \cdot \vec{p}$ theory is basically a perturbation theory. We can perform first-order or second-order perturbation[1]. The first-order theory provides us with a convenient analytical expression for describing the superlattice band structure at the cost of accuracy. The second-order theory has the capability of describing the band structure to a higher-order accuracy.

In Section 2.2, we describe the first-order theory. In Section 2.3, we present the second-order theory. In Section 2.4, for illustration of strain effects, we present the results of study of the strained-layer CdTe/ZnTe superlattice. In Section 2.5, we summarize the study.

2.2 First-Order Theory

2.2.1 Outline of First-Order Theory

In the first-order theory[2], we start with first-order $\vec{k} \cdot \vec{p}$ calculation of bulk band structures of strained constituent materials. The perturbation is carried out around the zone center ($\vec{k} = 0$). In other words, zone-center states are used as basis functions. Perturbation calculation provides solutions at general $\vec{k} \neq 0$, which are linear combinations of the basis functions.

We then expand the superlattice wave function in terms of bulk solutions, which include both propagating and evanescent states. With bulk solutions as linear combinations of zone-center states, the expansion can ultimately be written in terms of the basis functions. It is then a sum of products of envelope functions and basis functions.

The envelope functions are to be evaluated. In the first-order calculation, we take zone-center states of the two constituent materials to be the same. Superlattice wave functions are matched at the interface. This results in a set of equations for envelope functions. The Bloch condition is also imposed in accordance with the superlattice translational symmetry. This establishes another set of equations for envelope functions. Solutions to the two sets of equations provide superlattice wave functions characterized by superlattice wave vectors.

If only $k_{\|} = 0$ superlattice band structure is concerned, we have an analytic expression for it. This allows us to extract fundamental quantities of the superlattice very conveniently, for example, band gap and longitudinal effective mass. In superlattice engineering, the knowledge of band gap and effective mass as functions of growth parameters such as layer thicknesses is required for devising a superlattice structure with certain desired properties. The analytic expression is indeed very useful for that purpose.

2.2.2 Strained Crystal Band Structures

We start with the Hamiltonian of a strained crystal for the zinc-blende structure[6],

$$H = -\frac{\hbar^2}{2m}\nabla^2 + V(\vec{r}) + H_{s.o.} + H_{st}, \tag{2.8}$$

where V is the crystal potential, $H_{s.o.}$ is the spin-orbit interaction

$$H_{s.o.} = \frac{\hbar}{4m^2c^2}(\nabla V \times \vec{P}) \cdot \vec{\sigma}, \tag{2.9}$$

and H_{st} is the strain-induced term. According to Bloch's theorem, we then write a solution at an arbitrary wave vector $\vec{k}$ in an arbitrary band indexed by n as follows:

$$\psi_{n\vec{k}}(\vec{r}) = e^{i\vec{k}\cdot\vec{r}}u_{n\vec{k}}(\vec{r}),$$

where $u_{n\vec{k}}$ satisfies the periodic condition

$$u_{n\vec{k}}(\vec{r}) = u_{n\vec{k}}(\vec{r} + \vec{R}) \tag{2.10}$$

where $\vec{R}$ is a lattice vector. Substituting Eq. (2.10) into time-independent Schrodinger equation, neglecting k-dependent spin-orbit interaction and k-dependent strain term, we obtain the $\vec{k} \cdot \vec{p}$ Hamiltonian equation

$$\left(H + \frac{\hbar\vec{k}\cdot\vec{p}}{m} + \frac{\hbar^2k^2}{2m}\right) u_{n\vec{k}}(\vec{r}) = E_n(\vec{k})u_{n\vec{k}}(\vec{r}). \tag{2.11}$$

We will use perturbation theory to treat the above equation. The unperturbed equation is taken to be

$$\left(-\frac{\hbar^2}{2m}\nabla^2 + V(\vec{r})\right) u_{n0}(\vec{r}) = E_{n0}u_{n0}(\vec{r}). \tag{2.12}$$

Solutions to the unperturbed equation are the basis for perturbation calculation. Such solutions can be obtained by pseudopotential method or orthogonalized plane wave method. However, the knowledge of their explicit functional dependence is not required for the first-order calculation, which needs only matrix elements of the perturbation.

We will be concerned only with the superlattice eigenstates derived from near band-gap conduction and valence bands of constituent materials. $u_{n0}(\vec{r})$'s of near band-gap conduction and valence bands are taken as basis functions for perturbation calculation. Other solutions are disregarded. Perturbation calculation will give $u_{n\vec{k}}(\vec{r})$ at a general $\vec{k}$ in terms of these basis functions.

The calculation is carried out to first-order in $\vec{k}$. We need matrix elements of the perturbation, $\hbar\vec{k} \cdot \vec{p}/m$ and H_{st}, which are evaluated between various basis functions. We can compute them if basis functions are given. However, for a number of zinc-blende crystals, these matrix elements have been tabulated. In either case, it will be useful to know symmetry properties of these functions. It leads to selection rules for the matrix elements. In the following paragraph, we sketch symmetry properties of basis functions for a zinc-blende crystal.

Without spin-orbit interaction, the wave functions at the conduction band edge are represented by $|S \uparrow>$ and $|S \downarrow>$ with up and down spin, respectively. They have the symmetry of s-like atomic wave functions under transformations of the symmetry group of a zinc-blende crystal. On the other hand, the wave functions at the valence band edge are represented by $|X \uparrow>$, $|X \downarrow>$, $|Y \uparrow>$, $|Y \downarrow>$, $|Z \uparrow>$, and $|Z \downarrow>$. They transform like the components of a position vector under the symmetry transformations. The knowledge of symmetry properties simplifies calculation of matrix elements. For example, the matrix element $< S \uparrow |p_z|Z \uparrow>$ is nonzero while $< S \uparrow |p_z|X \uparrow>$ is zero since it has odd symmetry under a reflection with respect to x-y plane.

However, with spin-orbit interaction, the above functions no longer diagonalize the Hamiltonian. The interaction couples spin and orbital angular momentum. The wave functions are linearly combined into Kramer basis functions, which, for an unstrained crystal, diagonalize the Hamiltonian at $\vec{k} = 0$ with spin-orbit interaction[1]. We list the Kramer basis functions $|J, M_J>$ in the following:

$$\begin{array}{ll}
S\uparrow; & S\downarrow; \\
|3/2,3/2>=-\frac{1}{\sqrt{2}}(X+iY)\uparrow; & |3/2,-3/2>=-\frac{1}{\sqrt{2}}(X-iY)\downarrow; \\
|3/2,-1/2>=-\frac{1}{\sqrt{6}}[(X-iY)\uparrow+2Z\downarrow]; & |3/2,1/2>=-\frac{1}{\sqrt{6}}[(X+iY)\downarrow-2Z\uparrow]; \\
|1/2,-1/2>=-\frac{1}{\sqrt{3}}[-(X-iY)\uparrow+Z\downarrow]; & |1/2,1/2>=-\frac{1}{\sqrt{3}}[(X+iY)\downarrow+Z\uparrow].
\end{array} \tag{2.13}$$

Now, it is easy to write down $\vec{k}\cdot\vec{p}$ matrix elements with Kramer basis. For example,

$$< S\uparrow|\vec{k}\cdot\vec{p}|3/2,3/2>=-\frac{1}{\sqrt{2}}(k_x+ik_y)p,$$

where

$$p \equiv < S|p_x|X>=< S|p_y|Y>=< S|p_z|Z> . \tag{2.14}$$

In fact, p is the only parameter required for setting up $\vec{k}\cdot\vec{p}$ matrix.

As to the matrix of H_{st}, the strain tensor is required. For illustration, we shall consider the (001) grown free-standing superlattice. We assume the superlattice consists of alternating material layers of thicknesses a and b, respectively. The system in question is assumed to be in its lowest energy state. In other words, the elastic energy of the system is minimized with respect to the lateral lattice constant (i.e. the transverse force on the superlattice is zero) while subject to the constraint that the normal force on each interface is zero. For this configuration, it is easily verified that

$$\begin{aligned}
\epsilon_{xx} &= \epsilon_{yy}, \\
\epsilon_{xy} &= \epsilon_{yz}=\epsilon_{zx}=0,
\end{aligned}$$

while ϵ_{xx} and ϵ_{zz} are related by

$$\epsilon_{zz}=-2\frac{C_{12}}{C_{11}}\epsilon_{xx}, \tag{2.15}$$

where C_{ij}'s are elastic constants of the constituent material. Denoting the constituent materials by a and b, respectively, we have ϵ_{xx} determined by the following expression:

$$\epsilon^a_{xx} = -\frac{\Delta a_0}{a_0}\left[\frac{G^b b}{G^a a + G^b b}\right], \epsilon^b_{xx} = \frac{\Delta a_0}{a_0}\left[\frac{G^a a}{G^a a + G^b b}\right],$$

where

$$\begin{aligned} \Delta a_0 &= a^a_0 - a^b_0, \\ a_0 &= \frac{a^a_0 + a^b_0}{2}, \\ G^l &= 2\left[C^l_{11} + C^l_{12} - \frac{2{C^l_{12}}^2}{C^l_{11}}\right], \end{aligned} \tag{2.16}$$

and a^l_0 refers to a lattice constant.

Now, we are able to establish the Hamiltonian matrix. The presence of strain modifies the matrix. It adds a few matrix elements to the Hamiltonian through the use of deformation potentials. We follow Bir and Pikus[6] in the inclusion of strain effects. (001) grown superlattices are considered. The constituent materials have zinc-blende structure when undeformed. For illustration, we write down only nonzero matrix elements of the Hamiltonian at $k_{\|} = 0$:

$$\begin{aligned}
&< S\uparrow |H| S\uparrow >= E_g + C(\epsilon_{xx} + \epsilon_{yy} + \epsilon_{zz}), \\
&< S\downarrow |H| S\downarrow >= E_g + C(\epsilon_{xx} + \epsilon_{yy} + \epsilon_{zz}), \\
&< 3/2, 3/2|H|3/2, 3/2 >= \frac{l+m}{2}(\epsilon_{xx} + \epsilon_{yy}) + m\epsilon_{zz} \\
&< 3/2, -3/2|H|3/2, -3/2 >= \frac{l+m}{2}(\epsilon_{xx} + \epsilon_{yy}) + m\epsilon_{zz} \\
&< 3/2, 1/2|H|3/2, 1/2 >= \frac{1}{6}[(l+5m)(\epsilon_{xx} + \epsilon_{yy}) + (4l+2m)\epsilon_{zz}] \\
&< 3/2, -1/2|H|3/2, -1/2 >= \frac{1}{6}[(l+5m)(\epsilon_{xx} + \epsilon_{yy}) + (4l+2m)\epsilon_{zz}] \\
&< 3/2, 1/2|H|1/2, 1/2 >= -\frac{1}{3\sqrt{2}}(l-m)(\epsilon_{xx} + \epsilon_{yy} - 2\epsilon_{zz}) \\
&< 3/2, -1/2|H|1/2, -1/2 >= \frac{1}{3\sqrt{2}}(l-m)(\epsilon_{xx} + \epsilon_{yy} - 2\epsilon_{zz}),
\end{aligned}$$

$$
\begin{aligned}
&< S\uparrow|H|3/2,1/2>= iP(-\sqrt{\frac{2}{3}}k_z),\\
&< S\downarrow|H|3/2,-1/2>= iP(-\sqrt{\frac{2}{3}}k_z),\\
&< 1/2,1/2|H|1/2,1/2>= -\Delta+\frac{l+2m}{3}(\epsilon_{xx}+\epsilon_{yy}+\epsilon_{zz}),\\
&< 1/2,-1/2|H|1/2,-1/2>= -\Delta+\frac{l+2m}{3}(\epsilon_{xx}+\epsilon_{yy}+\epsilon_{zz}),
\end{aligned}
$$

where

$$P=-i\frac{\hbar}{m}< S|P_x|X>, \tag{2.17}$$

Δ is the spin-orbit splitting, and l, m, and n are parameters describing deformation potentials. Other nonzero matrix elements are obtained by taking the complex conjugate of those in Eq. (2.17).

Subsequently, we will reduce the 8-dimensional space to 6-dimensional by dropping two basis functions, $|1/2,-1/2>$ and $|1/2,1/2>$, which are split-off states. The spin-orbit splitting is usually so large that split-off bands do not significantly affect superlattice subbands near the superlattice band gap. Matrix elements between split-off states and the six states are included in the 6×6 Hamiltonian matrix by perturbation theory:

$$
\begin{aligned}
&< 3/2,1/2|H|3/2,1/2>_{6\times6}\\
=\;& < 3/2,1/2|H|3/2,1/2>_{8\times8}+\\
&\frac{|< 3/2,1/2|H|1/2,1/2>_{8\times8}|^2}{< 3/2,1/2|H|3/2,1/2>_{8\times8}-< 1/2,1/2|H|1/2,1/2>_{8\times8}},\\
&< 3/2,-1/2|H|3/2,-1/2>_{6\times6}\\
=\;& < 3/2,-1/2|H|3/2,-1/2>_{8\times8}+\\
&\frac{|< 3/2,-1/2|H|1/2,-1/2>_{8\times8}|^2}{< 3/2,-1/2|H|3/2,-1/2>_{8\times8}-< 1/2,-1/2|H|1/2,-1/2>_{8\times8}}
\end{aligned}
\tag{2.18}
$$

Other elements of the 6×6 matrix are simply equal to those of the 8×8 matrix. Given the 6×6 matrix here, it is readily seen that strain effects only renormalize on-diagonal values of the matrix.

It can be verified that the 6×6 problem can further be decomposed into two identical 1×1 and two identical 2×2 problems. The two 1×1 problems are associated with the two heavy-hole states $|3/2, 3/2>$ and $|3/2, -3/2>$, respectively. The two 2×2 problems are associated with $|S\uparrow>$ and $|3/2, 1/2>$, and $|S\downarrow>$ and $|3/2, -1/2>$, respectively. The 1×1 and 2×2 equations for each constituent material are to be solved seperately. Let us consider the 2×2 equation for $|S\uparrow>$ and $|3/2, 1/2>$, for example. Let

$$u_{\vec{k}} = C_s|S\uparrow> + C_p|3/2, 1/2> . \tag{2.19}$$

Then the 2×2 equation becomes

$$\begin{pmatrix} <S\uparrow|H|S\uparrow> -E & <S\uparrow|H|3/2,1/2> \\ <3/2,1/2|H|S\uparrow> & <3/2,1/2|H|3/2,1/2> -E \end{pmatrix} \begin{pmatrix} C_s \\ C_p \end{pmatrix} = 0. \tag{2.20}$$

C_s and C_p are nonzero only when the determinant of the matrix in Eq. (2.20) is set to zero. This results in a relation between E and k_z. There are *two* solutions for each given energy. The solution of the above equation results in the bulk band structure.

2.2.3 Strained-layer Superlattice Band Structure

In a superlattice, the crystal potential $V(\vec{r})$ varies spatially with the superlattice periodicity. Within effective-mass approximation, C_s and C_p become slowly varying functions of z, and k_z is replaced with $\hat{P}_z/\hbar$ where $\hat{P}_z$ is the z-component of momentum operator. Projecting onto the S state one further transforms the system into a differential equation

$$\left[\frac{2P^2}{3\hbar^2}\hat{P}_z[E- <3/2,1/2|H|3/2,1/2>]^{-1}\hat{P}_z + <S\uparrow|H|S\uparrow>\right] C_s(z) = EC_s(z). \tag{2.21}$$

We impose on $C_s(z)$ the Bloch condition

$$C_s(z+md) = \exp(iqmd)C_s(z), \tag{2.22}$$

where d is the superlattice periodicity and m is an integer. We assume that the basis functions for the two constituent materials are the same. In order for the superlattice wave function (which is a sum of products of envelope functions and basis functions) to be continuous at the interface, we require the envelope functions be continuous at the interface. At the interface, we integrate Eq. (2.21) across the boundary and, since C_s is assumed to be continuous, we obtain

$$C_s(z), [E- < 3/2, 1/2|H|3/2, 1/2 >]^{-1} \frac{dC_s(z)}{dz}, \tag{2.23}$$

both continuous at the interface. The superlattice wave function restricted to a single material is a linear combination of the two bulk solutions. Therefore, there are *four* unknown coefficients for a superlattice consisting of two constituent materials. There are *four* equations. Two of them assure the continuity of C_s and (roughly speaking) its derivative at an interface, while the other two apply to the neighboring interface in accordance with the Bloch condition. This results in a set of four simultaneous equations. The function C_s are nonvanishing only if

$$\cos(qd) = \cos(k_a a)\cos(k_b b) - \frac{1}{2}(\eta + \eta^{-1})\sin(k_a a) sin(k_b b),$$

where

$$\eta = \frac{k_a}{k_b} \frac{E- < 3/2, 1/2|H|3/2, 1/2 >_b}{E- < 3/2, 1/2|H|3/2, 1/2 >_a}. \tag{2.24}$$

Here k_a and k_b are determined by setting the determinant of the coefficient matrix in Eq. (2.20) to zero for material a and b, respectively. The above equation is referred to as light-particle dispersion relation. It describes the mini-band structure derived from the S-like and light-hole-like states. The mini-bands include both valence and conduction bands.

The same procedure can be applied to the 1×1 equation for heavy-hole states. Heavy-particle dispersion relation is then obtained. It describes only heavy-hole valence subbands. No conduction subband is derived from heavy-hole states.

Hence, the conduction band edge is determined only by the light-particle dispersion relation. However, the superlattice valence band edge is the higher one of the first heavy-hole and the first light-hole subband edges. The superlattice band gap is determined by the energy difference between the conduction and the valence band edges.

2.3 Second-Order Theory

2.3.1 Outline of Second-Order Theory

In the second-order perturbation theory[3], we start with the empirical pseudopotential Hamiltonian without spin-orbit interaction and strain effects. The Hamiltonian of a constituent material is made up of an unperturbed term and a perturbation. The unperturbed term is the sum of the kinetic energy and the pseudopotential obtained by averaging those of the two constituent materials. The perturbation accounts for the difference between the full Hamiltonian and the unperturbed one.

The eigenstates of the unperturbed Hamiltonian at $\vec{k} = 0$ are taken as basis functions for perturbation calculations. Empirical pseudopotential method (EPM) is used to solve for unperturbed energy eigenvalues and eigenfunctions. The method employs plane waves $\exp(i\vec{G} \cdot \vec{r})$'s, where $\vec{G}$'s are reciprocal lattice vectors of constituent materials[4]. In the actual calculation, we expand a wave function in a truncated basis which includes 113 plane waves. The calculation provides 113 eigenstates. Out of them, basis functions for the perturbation calculation are selected (typically 23, as actually implemented).

Next, spin degeneracy is included. "Near-in" wave functions are then chosen, for example, the two at the conduction band edge and the six at the valence band edge for a zinc-blende structure. The rest of basis functions are called "far-out" states. Only superlattice eigenstates primarily derived from the near-in states are of interest for studying near band-gap optical properties.

We then deal with the perturbation, which includs the $\vec{k} \cdot \vec{p}$ term, spin-orbit interaction, the strain term, and the difference between the material pseudopotential and the averaged one. We employ Löwdin perturbation theory. It treats matrix elements between near-in states exactly. In the theory, however, effects of far-out states are also included. We calculate eigenvalues correct to the second order and wave functions correct to the first order[5]. Band structures of constituent materials are established.

To calculate superlattice eigenstates, complex band structures of constituent materials are required. A scheme is used to transform the Hamiltonian equation into one which has k_z as its eigenvalue. Solving the equation results in k_z which is generally complex. This provides both propagating and evanescent eigenstates. Each state is labeled by the in-plane wave vector k_x, k_y, and ϵ which is the state energy.

Superlattice wave functions are to be solved. They are expressed as linear combinations of bulk solutions at a given energy and in-plane wave vector. They are matched at the interface. The boundary conditions, expressed through the use of current density matrices, ensure the continuity of probability current. We also impose Bloch condition which follows the superlattice translational symmetry. We thus set up an eigenvalue equation. The eigenvalue is $\exp(-iQd)$ where Q is the superlattice wave vector, and d is the superlattice periodicity. The eigenfunction is a superlattice eigenstate. Consequently, the band structure is found for a strained-layer superlattice.

2.3.2 Strained Crystal Band Structure

Pseudopotential Description

The empirical pseudopotential method basically follows that of Bergstresser and Cohen[4]. We start with a reference material which has the Hamiltonian

$$H_R \equiv \frac{\vec{P}^2}{2m} + \frac{1}{2}\left[V_a(\vec{r}) + V_b(\vec{r})\right] = \frac{\vec{P}^2}{2m} + <V> \tag{2.25}$$

where a and b label the constituent materials and $V_l(r)$ is the pseudopotential of material l described in terms of pseudopotential form factors. Alloy materials are treated in a virtual crystal approximation. At this stage, spin-orbit interaction, and deformation potential are not included. The reference Hamiltonian has at $\vec{k} = 0$ eigenfunctions

$$U_\beta(\vec{r}) = \frac{1}{\sqrt{\Omega}} \sum_{\vec{G}} R_{\beta\vec{G}} e^{i\vec{G}\cdot\vec{r}}, \tag{2.26}$$

where β labels the various eigensolutions, Ω is the unit cell volume, $\vec{G}$ is a reciprocal lattice vector and R is an expansion coefficient. The corresponding eigenvalue of U_β is denoted as ϵ_β. For crystals of zinc-blende structure, $U_\beta(\vec{r})$'s belong to Γ_{15} representation at the valence band edge, and to Γ_1 representation at the conduction band edge, in the terminology of group theory. Following the convention, they are made to transform like atomic p functions at the valence band edge, and like atomic s functions f(r) at the conduction band edge, under the operations of the tetrahedral group. They are accordingly denoted as X, Y, Z and S. When spin degeneracy is taken into account, we designate them by X↑, X↓, Y↑, Y↓, Z↑, Z↓, S↑, and S↓. These states will be taken as near-in states while the rest are far-out states.

$\vec{k} \cdot \vec{p}$ Description

The Hamiltonian H_l of constituent material l in the presence of a strain is

$$H_l = H_R + \Delta V^l + H^l_{s.o.} + H^l_{st},$$

where

$$\Delta V^l = V^l - \frac{1}{2}(V^a + V^b). \tag{2.27}$$

Here $H^l_{s.o.}$ represents the spin-orbit interaction, and H^l_{st} represents the stress interaction in material l^6.

Now with the eigenstates of the reference Hamiltonian as basis functions, the $\vec{k} \cdot \vec{p}$ Hamiltonian matrix of material l can be constructed. We will use Lowdin perturbation theory to treat the perturbation $\Delta V + \hbar\vec{k} \cdot \vec{p}/m$. In this theory the near-in states play the role of degenerate states. However, the theory modifies the near-in states for each material to include effects of the far-out states. We will use the notation $U_d(r)$, where d runs over the eight states, to label the near-in states. We construct, in each material, the cell-periodic functions,

$$U^l_{dj}(r) = U_d(r) + \sum_\beta W^l_{d\beta j} U_\beta(r),$$

where

$$W^l_{d\beta j} = \frac{< U_\beta|\Delta V^l + \hbar\vec{k}_j \cdot \vec{p}|U_d >}{\epsilon_d - \epsilon_\beta}, \tag{2.28}$$

where the sum over β does not include the explicitly treated states labeled by d, and $\vec{k}_j$ is a point in $\vec{k}$ space. The Bloch and evanescent states in each material are written as

$$\psi^l_j = \frac{e^{i\vec{k}^l_j \cdot \vec{r}}}{\sqrt{N}} \sum_d C^l_{dj} U^l_{dj}(\vec{r}), \tag{2.29}$$

where N is the number of bulk primitive cells (two atoms in the zinc-blende structure) in the superlattice. The cell-periodic states U are normalized to a unit cell and the C's are taken so that $[(\psi_{j*})^* \psi_j]$ integrates to unity over the superlattice volume. We construct the 8 × 8 matrices defined by

$$H^l_{dd'}(\vec{k}^l_j) \equiv < U_d | e^{-i\vec{k}^l_j \cdot \vec{r}} H_l e^{i\vec{k}^l_j \cdot \vec{r}} | U^l_{d'j} > . \tag{2.30}$$

Then we add to the above $\vec{k} \cdot \vec{p}$ Hamiltonian matrices the spin-orbit interaction and a term which describes the strain effects through the use of deformation potentials. The matrix elements of the spin-orbit interaction and the strain term are given empirically. The expansion coefficient C's are found by solving the eigenvalue equation

$$[H^l_{dd'}(\vec{k}^l_j) - \epsilon \delta_{dd'}] C^l_{d'j} = 0, \tag{2.31}$$

where ϵ is the state energy.

Normally, the eigenstates, with k_z being real, describe propagating states in a bulk semiconductor. The Born-von Karman periodic boundary condition forbids the existence of any evanescent states. But in a superlattice, the wave function restricted in a single material does not have to be freely propagating. Evanescent states are also allowed. This point becomes obvious when we think of the quantum mechanics of a step potential barrier. In that case, when an electron does not have sufficient kinetic energy to overcome the barrier height, the wave function is evanescent inside the barrier. It has the form exp($-\kappa$z) with a complex wave vector $i\kappa$. Generalizing this situation to the superlattice problem, we need to calculate complex band structures of constituent materials first. Next, a mathematical scheme for conveniently calculating the complex band structure will be presented.

The Complex Band Structure of a Constituent Material

For the purpose of complex band structure calculation, it is convenient to display the k dependence of $H^l_{dd'}(\vec{k}^l_j)$ explicitly. In the second-order $\vec{k} \cdot \vec{p}$ perturbation theory, the Hamiltonian matrix $H^l_{dd'}(\vec{k}^l_j)$ is quadratic in $k^l_{\perp j}$. We rewrite

Eq. (2.31) as

$$[H^2_{dd'}(k^l_j)^2 + H^{1l}_{dd'}(k^l_j) + H^{0l}_{dd'}]C^l_{d'j} = 0, \tag{2.32}$$

where the matrix H^2 is the same for the two materials. Here, the symbol k_j, without a vector sign, refers to the normal component of the wave vector. Each of the three H matrices is Hermitian. Eq. (2.32) can be transformed into an eigenvalue equation for k^l_j, viz.,

$$\begin{pmatrix} 0 & 1 \\ -[H^2]^{-1}H^0 & -[H^2]^{-1}H^1 \end{pmatrix} \begin{pmatrix} C \\ kC \end{pmatrix} = k \begin{pmatrix} C \\ kC \end{pmatrix}, \tag{2.33}$$

Note that in this equation we have doubled the dimension of the matrix. In a typical calculation, with the Kramer basis functions as near-in states, the H matrices are 8×8 matrices. Thus the matrix in the last equation is 16×16. We refer to Eq. (2.33) as 16-band model. This results in sixteen eigenvalues of k_j for each given set of k_x, k_y, and ϵ.

Note that because the various H matrices in Eq. (2.32) are Hermitian, if k satisfies Eq. (2.32), so does k^*. Orthogonality relations for the eigenvalue equation are particularly important. The orthogonality condition is found by considering two eigenvalues k_j and k_{i^*} ($k_{i^*} = k^*_i$), writing the two eigenvector equations, taking the Hermitian adjoint of the second equation, overlapping each equation with the other's eigenvector, and subtracting. This procedure gives

$$(k_j - k_i)C^\dagger_{i^*}[H^2(k_j + k_i) + H^1]C_j = 0. \tag{2.34}$$

Thus, k_j equals k_i or else the vector product vanishes. The vector product has a simple physical interpretation. It is the z component of the current-density operator averaged over a unit cell,

$$\begin{aligned} J^l_{i^*j} &\equiv \ < \psi^l_{i^*}|J_z(r)|\psi^l_j >_A \\ &= \frac{1}{\hbar\Omega}C^\dagger_{i^*}[H^2(k_j + k_i) + H^1]C_j, \end{aligned} \tag{2.35}$$

where ψ_j^l is given by Eq. (2.29) and the subscript A implies an average over a unit cell. The orthogonality condition can then be written as

$$J^{l}_{i^{*}j} = J^{l}_{j^{*}j}\delta_{ij}. \tag{2.36}$$

2.3.3 Superlattice Band Structure

In the description of the individual materials making up a superlattice, there is an arbitrary energy zero. When describing an interface between two materials, the energy scales of the two materials must be the same. We include an offset energy between the valence band maxima of the two materials. We take this energy offset to be given empirically.

We describe the matching between bulk eigenstates of the individual materials to construct the eigenstates of the interface using the z component of the current density operator averaged over a unit cell. In analogy with Eq. (2.35), we define

$$< \psi^{l}_{i^{*}} | J_z(t) | \psi^{l'}_{j} >_A = J^{ll'}_{i^{*}j} e^{i(k^{l'}_{j} - k^{l}_{i})t}. \tag{2.37}$$

In the above equation, the interface is taken to be a distance t from the origin.

We expand an interface eigenstate Ψ with a given energy and $\vec{k}_{\|}$ in terms of the individual bulk material eigenstates (both propagating and evanescent) with those values of ϵ and $\vec{k}_{\|}$,

$$\Psi(r) = \sum_j A_j \psi_j(r) + \sum_i B_i \phi_i(r), \tag{2.38}$$

where A_j and B_i are expansion coefficients and ψ_j (ϕ_i) are the eigenstates in material a (b) at the given values of ϵ and $\vec{k}_{\|}$. The notation in Eq. (2.38) means that the sum on ψ is taken for r in material a and the sum on ϕ is taken for r in material b. When calculating $< \psi_j | J | \Psi >_A$ at the interface, we have

$$< \psi_{j^{*}} | J | \Psi >_A = < \psi_{j^{*}} | J | \sum_k A_k \psi_k >_A = < \psi_{j^{*}} | J | \sum_i B_i \psi_i >_A . \tag{2.39}$$

By the orthogonality condition,

$$A_j = \sum_i \frac{1}{J^a_{j^*j}} J^{ab}_{j^*i} B_i, \tag{2.40}$$

where the interface is taken to contain the origin. Thus we are able to relate the expansion coefficients in the two constituent materials. The same argument could as well be applied in a different order to give B_i in terms of A_j.

Again, we apply the same argument to the neighboring interface at $t = b$ assuming material a sits on the left-hand side of the interface at $t = 0$ while material b sits on its right-hand side. At the interface $t = b$, for a superlattice eigenstate with a superlattice wave vector Q, in accordance with Bloch condition, we have

$$\Psi(t = b) = \sum_j \left[e^{iQ(a+b)} A_j e^{-ik^a_j a} \psi_j(t = 0)\right] + \sum_i \left[B_i e^{ik^b_i b} \phi_i(t = 0)\right]. \tag{2.41}$$

So, the interface-matching condition at $t = b$ is

$$B_i e^{ik^b_i b} = \sum_j \frac{J^{ba}_{i^*j}}{J^b_{i^*i}} e^{-ik^a_j a} e^{iQ(a+b)} A_j, \tag{2.42}$$

Combining Eq. (2.40) and Eq. (2.42) we form an eigenvalue equation

$$\sum_{j'} M_{jj'} A_{j'} = e^{-iQ(a+b)} A_j,$$

where

$$M_{jj'} = \sum_i e^{-ik^a_{j'} a} \frac{1}{J^a_{j^*j}} e^{-ik^b_i b} \frac{1}{J^b_{i^*i}} J^{ab}_{j^*i} J^{ba}_{i^*j'}. \tag{2.43}$$

By solving the above eigenvalue equation numerically, we find the eigenvalue $e^{-iQ(a+b)}$ and the eigenvector A_j. The expansion coefficients B_i in material b are then found from Eq. (2.42).

2.4 Strained-Layer CdTe-ZnTe Superlattices

2.4.1 Introduction

In this section, we present results of application of the previous theory to the strained-layer CdTe/ZnTe superlattice. In this case, the lattice mismatch is relatively large (about 6.2%). The interest in this system is that it has an energy gap in the visible, making it a promising light source and photodetector. The band structures of strained CdTe and ZnTe will be shown. The band gap of the strained-layer CdTe/ZnTe superlattice will be discussed.

2.4.2 Strained CdTe and ZnTe Band Structures

The CdTe layer in the (001) grown superlattice contains a biaxial tensile strain while the ZnTe layer is biaxially compressed. This changes the band structures of the bulk CdTe and the bulk ZnTe.

In Figure (2.1), we show the band structure of strained CdTe. In Figure (2.2), we show band structure of the strained ZnTe. The valence band off-set is taken to be zero for the unstrained system. Without strain, the heavy-hole and the light hole states would be degenerate in both CdTe and ZnTe, typical of an unstrained zinc-blende crystal. The strain is assumed to be evenly distributed in the CdTe and the ZnTe layer. In other words, the lateral lattice constant of the superlattice is taken to be the average of those of CdTe and ZnTe. This can be realized by growing a CdTe/ZnTe superlattice on a substrate of $Cd_{0.5}Zn_{0.5}Te$ much thicker than the superlattice. The lateral lattice constant of the superlattice takes the value of that of the substrate. As shown in the graphs, the heavy-hole band is pushed above the light-hole band in the CdTe, which is under an biaxial tensile stress, while the light-hole band is pushed above the heavy-hole band in the ZnTe, which is under an biaxial compressive stress. Since the light-hole states and the heavy-hole states are decoupled at $k_{\|} = 0$ (see Section 2.2), they separately make light-hole and heavy-hole subbands at $k_{\|} = 0$.

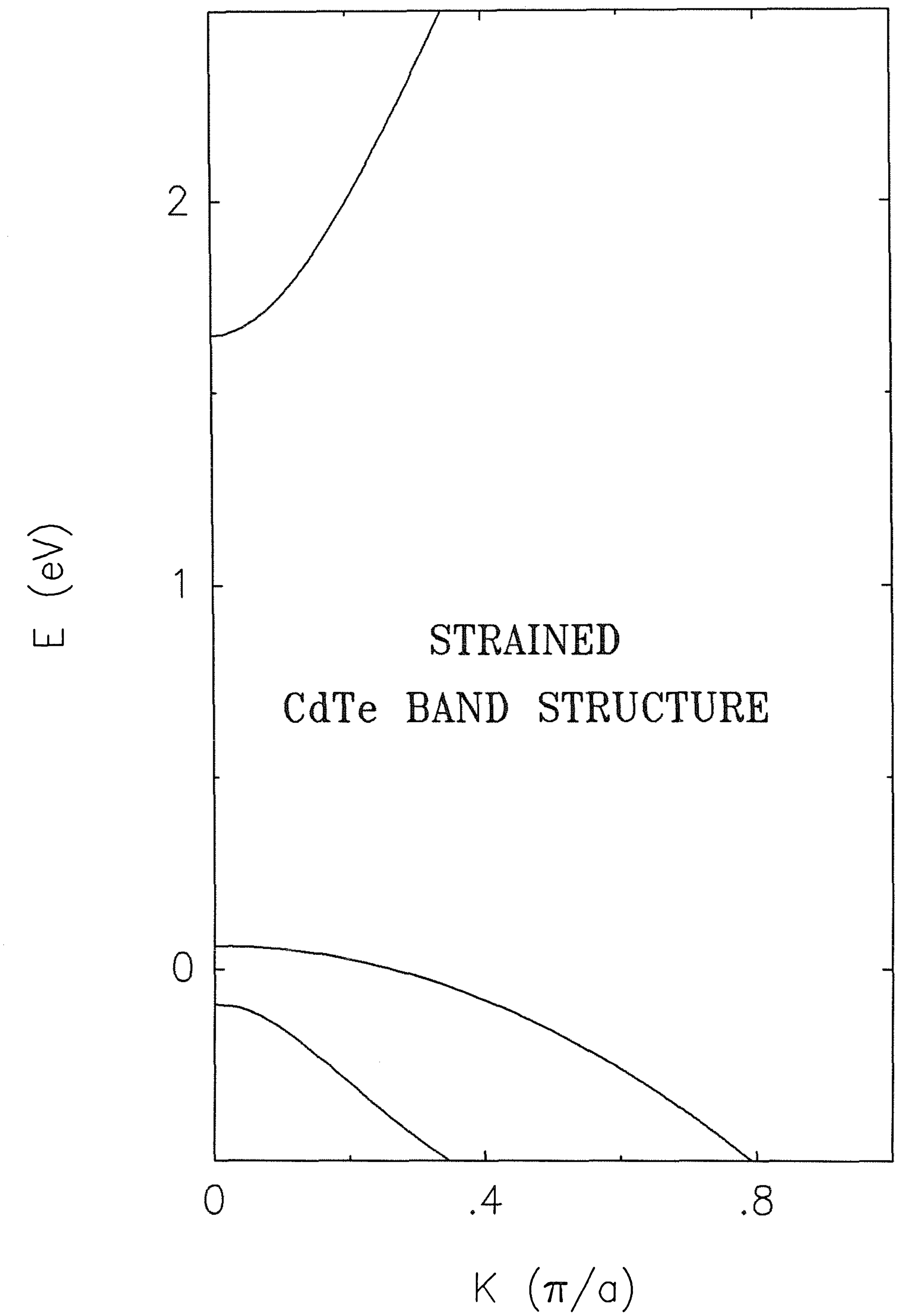

Figure 2.1: Strained CdTe band structure at $\vec{k}_{\parallel} = 0$. The strain is assumed to be distributed evenly in CdTe and ZnTe. The zero energy is taken to be at the valence band edge of the unstrained CdTe.

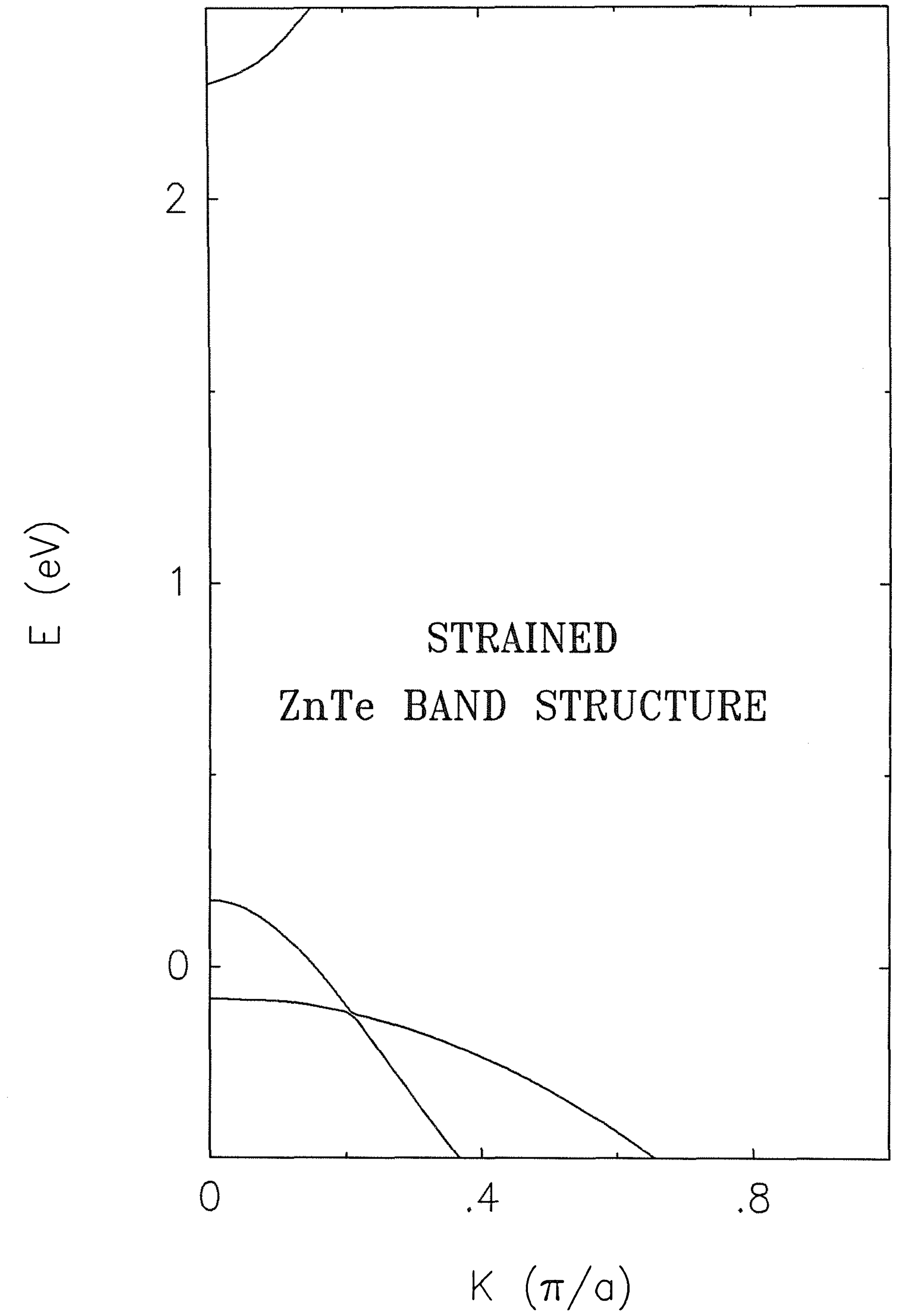

Figure 2.2: Strained ZnTe band structure at $\vec{k}_{\|} = 0$. The strain is assumed to be distributed evenly in CdTe and ZnTe. The zero energy is taken to be at the valence band edge of the unstrained CdTe.

2.4.3 Band Gap of the Superlattice

Since the conduction band edge of CdTe is lower in energy than that of ZnTe, the electron is confined in CdTe. The lowest conduction subband is somewhere between the conduction band edges of CdTe and ZnTe. On the other hand, strain makes the heavy-hole band of CdTe higher than that of ZnTe. The heavy hole is confined to CdTe. Due to the heavy effective mass, the first heavy-hole subband of the superlattice is close to the heavy-hole band of CdTe, with the edge of the superlattice subband being lower because of quantum confinement. On the other hand, strain makes the light-hole band of ZnTe higher than that of CdTe. The light hole is confined to ZnTe. The edge of the first light-hole subband of the superlattice is lower than that of ZnTe.

The superlattice valence band edge is determined by the higher one of the heavy-hole and light-hole subbands. In the case where the heavy-hole subband is higher, the superlattice band gap is equal to the energy difference between edges of the conduction and the heavy-hole subbands. In the case where the light-hole subband is higher, the gap is equal to the energy difference between edges of the conduction and the light-hole subbands. The relative positions of the heavy-hole and the light-hole subbands depend on the size of quantum confinement, which, in turn, depends on layer thicknesses. This results in a superlattice band gap whose functional dependence on layer thicknesses is *discontinuous.*

Results of the calculation of the CdTe-ZnTe superlattice band gap as a function of the thicknesses of CdTe and ZnTe layer are shown for the unstrained (Figure 2.3) and the free-standing strained-layer superlattice[7] (Figure 2.4). The valence band off-set is taken to be zero for the unstrained system. However, the presence of strain effectively changes the value of valence band off-set. We assume the change in the valence band off-set is determined by the shift of bulk energy bands described by deformation potentials. Notice that in a CdTe-ZnTe

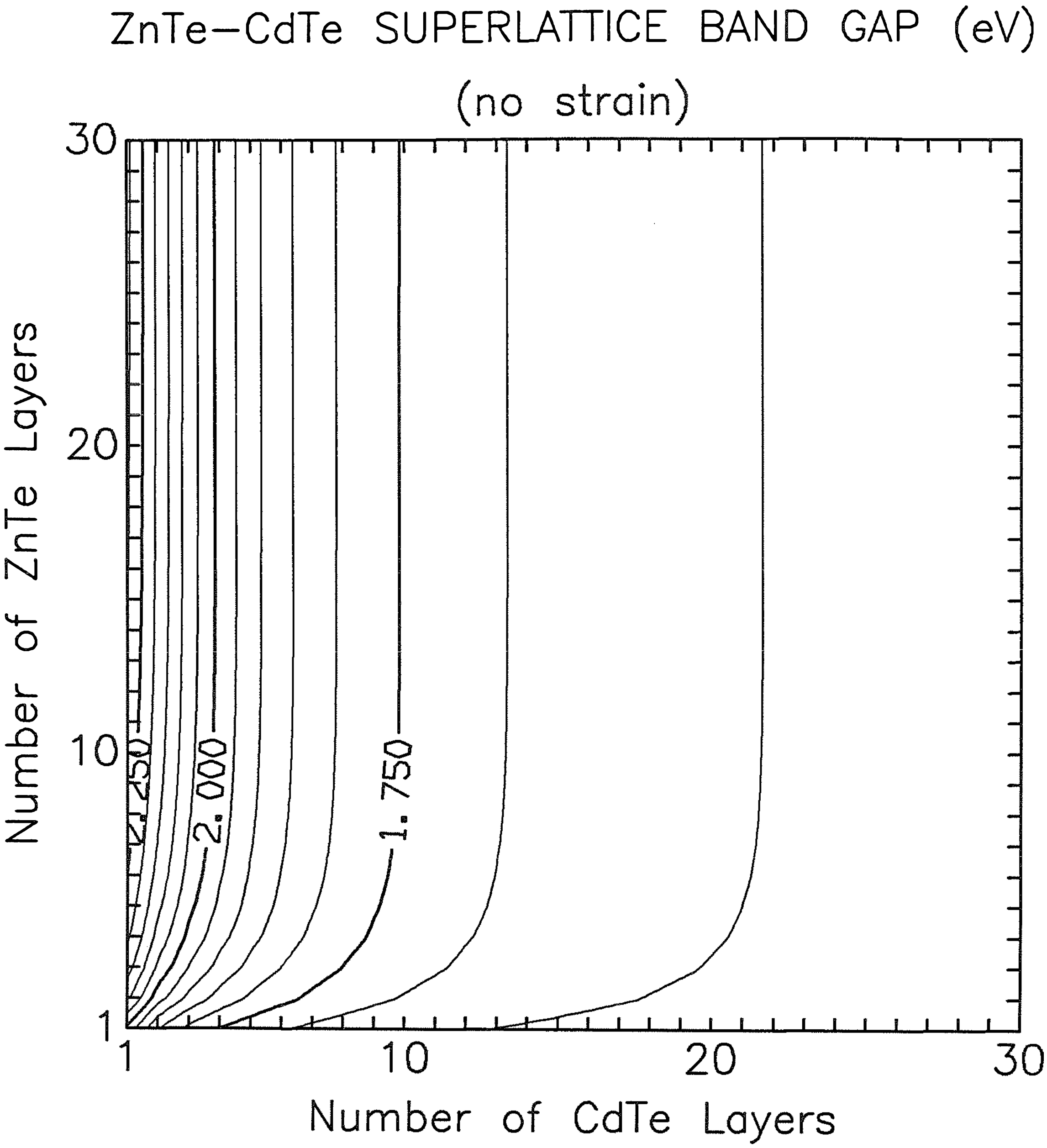

Figure 2.3: Unstrained CdTe/ZnTe superlattice band gap as a function of layer thicknesses. The zero energy is taken to be at the valence band edge of the unstrained CdTe. The valence band off-set is taken to be zero.

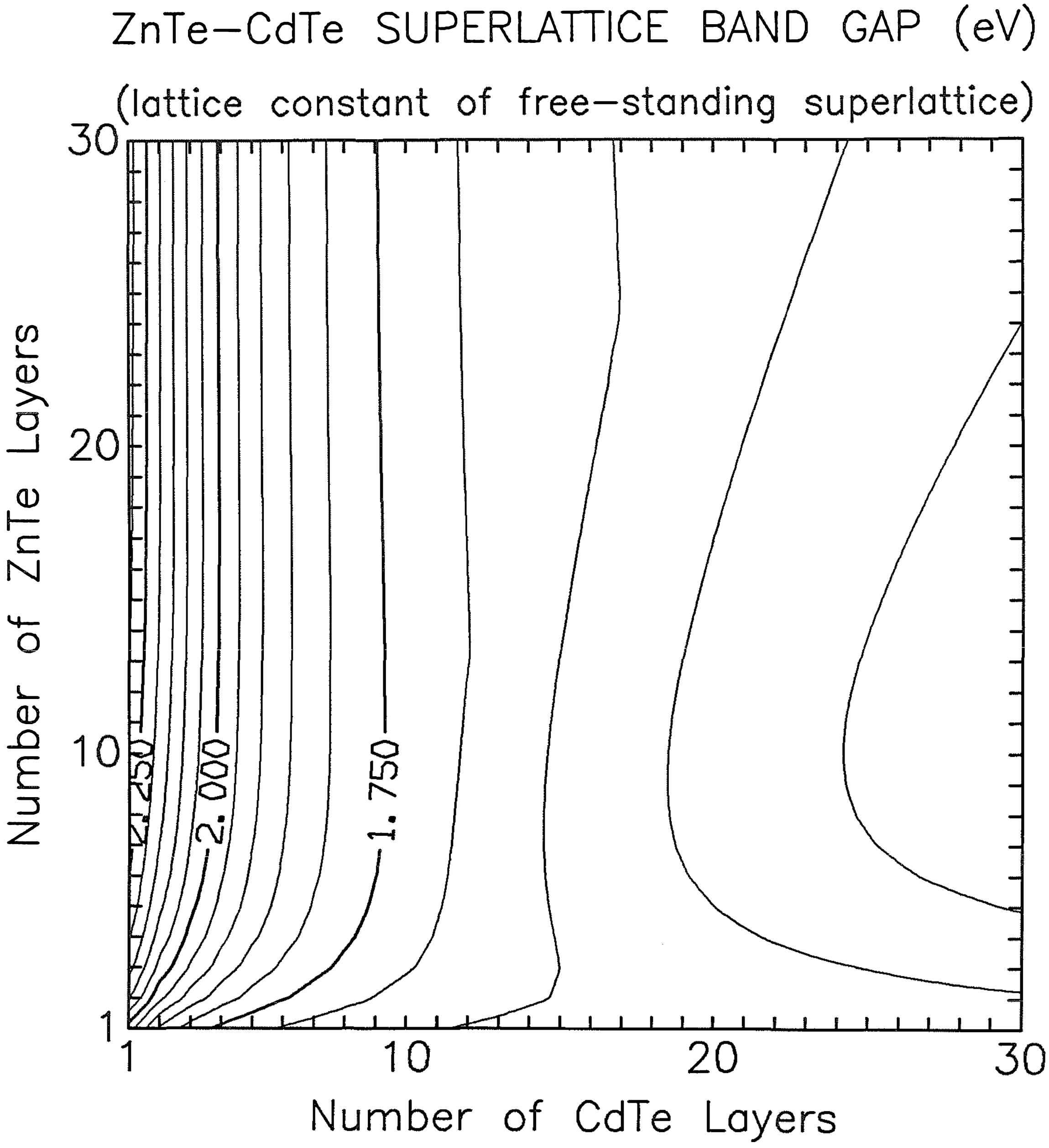

Figure 2.4: Free-standing strained CdTe/ZnTe superlattice band gap as a function of layer thicknesses. The zero energy is taken to be at the valence band edge of the unstrained CdTe.

superlattice, the ZnTe layer acts like potential barrier while the CdTe layer acts like a potential well. This explains why in Figure (2.3) and Figure (2.4) the band gap changes relatively fast with CdTe layer number while it changes relatively slowly with ZnTe layer number. We also see how different the two graphs are. The structure in the plot for the strained case is due to the discontinuous functional dependence of the gap on layer thicknesses.

The presence of strain also affects the luminescence intensity. When the highest valence subband is heavy-hole-like, the electron and the (heavy) hole are both confined in CdTe. They recombine to radiate more readily than in a bulk CdTe. This gives rise to higher luminescence intensity from the superlattice than that from the CdTe crystal. On the other hand, when the highest valence subband is light-hole-like, the electron and the (light) hole are separated in different layers. The radiative recombination becomes less likely in the superlattice and the luminescence intensity is weaker.

In fact, the superlattice band structure may be different if the band off-set is not small as have been assumed in the previous discussion. However, the study of the specific free-standing CdTe/ZnTe system demonstrates what effects strain could have on optical properties.

2.5 Summary

In summary, we have developed the $\vec{k}\cdot\vec{p}$ theory of band structures of strained-layer superlattices. Two versions of the theory are presented. In one version, the theory provides analytical expressions for dispersion relations of light-particle and heavy-particle subbands. It allows us to calculate the dependence of the band gap on growth parameters such as layer thicknesses in a quick way. That is very useful in devising a proper superlattice with desired properties. On the other hand, the theory in the other version is less analytical but more accurate. We start with the calculation of complex band structures of constituent materials. An eigenstate is labeled by k_x, k_y, and k_z. Generally complex k_z is computed for each given set of k_x, k_y, and energy. Continuity of current at an interface is expressed through the use of current density matrices. This results in an eigenvalue equation for superlattice eigenstates with the eigenvalue $\exp(-iQd)$, where Q is a superlattice wave vector in the growth direction. Solution of the equation results in the superlattice band structure. A superlattice eigenstate is labeled by k_x, k_y, and Q.

We have applied the theory to the CdTe/ZnTe superlattice. It is found that the degeneracy of heavy-hole and light-hole bands is lifted by the presence of strain in the layers. The light-hole band is lower than the heavy-hole band in CdTe, which has the larger lattice constant, while the light-hole band is higher than the heavy-hole band in ZnTe, which has the smaller lattice constant. The band gap has discontinuous dependence of layer thicknesses, which is due to strain-induced splitting of valence band edges. Luminescence intensity from the superlattice is increased when effects of strain are such that electrons and holes are confined to the same layer. It is decreased when electrons and holes are seperated by the strain.

Strain effects in the HgTe/CdTe superlattice have also been studied with the theory developed in this chapter. The results will be presented in Chapter 4.

References

1. E. O. Kane, in *Semiconductors and Semimetals*, edited by R. K. Willardson and A. C. Beer (Academic, New York, 1966), Vol. 1, p. 75.
2. G. Bastard, Phys. Rev. **B 25**, 7584 (1982).
3. D. L. Smith, and C. Mailhiot, Phys. Rev. **B 33**, 8345 (1986).
4. M. L. Cohen and T. K. Bergstresser, Rev. Rev. **141**, 789 (1966).
5. P. O. Löwdin, J. Chem. Phys. **19**, 1396 (1951).
6. See, for example, G. L. Bir and G. E. Pikus, *Symmetry and Strain-Induced Effects in Semiconductors* (Wiley, New York, 1974).
7. R. H. Miles, G. Y. Wu, M. B. Johnson, and T. C. McGill, Appl. Phys. Lett. **48**, 1383 (1986).

Chapter 3

$\vec{k} \cdot \vec{p}$ Theory of Band Structures of Semimagnetic Semiconductor Superlattices

3.1 Introduction

3.1.1 Background

In this chapter, we develop $\vec{k} \cdot \vec{p}$ method for calculating band structures of *semimagnetic semiconductor superlattices* (SMSCSL). SMSCSL is defined as a superlattice (SL) made up of alternating layers of semiconducting materials, with one or more of which being semimagnetic semiconductors (SMSC). A SMSC, usually a ternary alloy like $Cd_{(1-x)}Mn_xTe$, contains randomly distributed substitutional magnetic ions, Mn^{++} for example. It displays interesting and useful electrical and optical properties, particularly when being placed in a magnetic field. The presence of substitutional magnetic ions in SMSC leads to *spin-spin exchange interaction* between localized magnetic moments and band electrons. This, in turn, has rather important consequences on band structures.

Without the presence of any external magnetic field, a SMSC behaves just like a non-magnetic alloy. In the presence of a magnetic field, an electron performs orbital motion. Its energy is quantized and forms so-called Landau levels. The energy levels are spin-split by the interaction between electron spin and magnetic field. More importantly, because the localized spins in a SMSC are preferentially aligned in the opposite direction of magnetic field, an internal field is effectively created, which acts upon band electrons in addition to the external field. Spin-splitting of electronic energy levels could be , therefore, greatly enhanced.

With superlattices made up of alternating layers of SMSCs, properties of materials become more tailorable. Recently, $Cd_{1-x}Mn_xTe/Cd_{1-y}Mn_yTe$ and $Hg_{1-x}Mn_xTe/Cd_{1-y}Mn_yTe$ superlattices have attracted much attention. The $Cd_{1-x}Mn_xTe/Cd_{1-y}Mn_yTe$ superlattice has been proposed as a candidate for magnetically tunable laser material. The $Hg_{1-x}Mn_xTe/Cd_{1-y}Mn_yTe$ superlattice has been considered as magnetically tunable infrared material. Interesting measurements with these systems have been made. For the understanding of properties of semimagnetic semiconductor superlattices, it is very important to develop a theory to guide the work and to interprete the measured data.

3.1.2 Outline of the Chapter

We restrict our attention to the case where the magnetic field is directed along the growth axis of SMSCSL, since it happens to be most potentially useful as well as tractable in terms of computation time. Other cases, where the magnetic field is not directed in the growth direction of the superlattice, require that further approximations be made or that huge amount of computer time be consumed. They are not explicitly considered here, for they do not as well illuminate magnetic effects on the band structure of a SMSCSL. For illustration, moreover, we consider only (001) grown unstrained superlattices whose repeat cycle consists of two materials of zinc-blende structure. Multi-layer superlattices, however, can be treated in a smilar fashion. The case of a strained-layer SMSCSL will be left out, since it can be dealt with by a straightforward combination of theories in Chapter 2 and in this chapter.

The nonmagnetic part of the Hamiltonian of a SMSC will be treated within the *virtual crystal approximation.* The magnetic part, i.e., the exchange interaction between localized d-level electrons and band electrons, will be dealt with within *mean field theory*[3]. However, we should note that, by using experimental values of band gaps and magnetic susceptibilities, the theory will take into account empirically higher-order effects, which result in band gap bowing and antiferromagnetic cluster formation.

Since the presence of a magnetic field adds a spatially varying vector potential to the Hamiltonian, the translational symmetry of the bulk crystal is no longer in the symmetry group. A wave function becomes a sum of products of slowly varying functions (envelope functions) and cell-periodic Bloch functions. *Effective-mass theory* is used to calculate envelope functions and energy eigenvalues.

Bulk solutions to the effective-mass equation are linearly combined to form superlattice wave functions. Boundary conditions are so formulated that the current is continuous at the interface. Imposing boundary conditions and Bloch condition results in an eigenvalue equation. Superlattice eigenstates and eigenvalues are evaluated by solving the equation.

With the developed theory, we calculate band structures of $Cd_{1-x}Mn_xTe$ and the $Hg_{1-x}Mn_xTe/Cd_{1-y}Mn_yTe$ superlattice. Band structures with and without the presence of magnetic field are shown.

In Section (3.2), we describe the $\vec{k} \cdot \vec{p}$ theory of band structures of semimagnetic semiconductors. Examples of band structures obtained by this method are presented for $Cd_{1-x}Mn_xTe$. In Section (3.3), we describe the $\vec{k} \cdot \vec{p}$ theory of band structures of semimagnetic semiconductor superlattices. In Section (3.4), examples of band structures obtained by this method are presented for a $Hg_{1-x}Mn_xTe/Cd_{1-y}Mn_yTe$ superlattice. In Section (3.5), we summarize the study.

3.2 Theory of Band Structures of Semimagnetic Semiconductors

3.2.1 Outline of the Section

The theory is a second-order perturbation theory[1]. The Hamiltonian of a SMSC in a magnetic field is made up of an unperturbed term and a perturbation. A reference material is chosen such that it has the pseudopotential formed by averaging those of constituent materials. Its Hamiltonian is regarded as unperturbed. Eigenstates of the reference Hamiltonian are basis functions for perturbation calculation. Empirical pseudopotential method (EPM) is performed to solve for unperturbed energies and wave functions. It employs a truncated but still very large plane-wave basis $\exp(i\vec{G}\cdot\vec{r})$'s, where $\vec{G}$'s are reciprocal lattice vectors of constituent materials. The wave function does not include a spin part yet. Diagonalization of the reference Hamiltonian matrix results in a number of energy bands of the reference material. In a typical calculation, *one hundred and thirteen* plane waves are used. The lowest *twenty-three* energy bands are kept for calculation of superlattice band structure. The lowest conduction band and the highest three valence bands are among them.

Spin degeneracy is then included. A set of wave functions are selected, for example, the two at the conduction band edge and the six at the valence band edge, in the case of zinc-blende structure. They are called "near-in" states while the rest are called "far-out" states. Only those superlattice eigenstates will be of interest which are primarily derived from the near-in states. In light of this, Löwdin perturbation theory is used. Effects of near-in states are included exactly, while those of far-out states are included only to first order. This establishes the effective-mass Hamiltonian equation for near-in envelope functions. With Löwdin perturbation theory, the wave function is calculated correctly to the first order and the eigenvalue is calculated correctly to the second order. Solving the equation gives band structures of constituent materials. Each eigenstate is labeled by k_x, k_z, and N, which is the Landau level index, instead of k_x, k_y and k_z as in the nonmagnetic problem.

However, to calculate the superlattice problem, complex band structures of constituent materials are required. The effective-mass Hamiltonian equation is transformed into an eigenvalue equation, which has k_z (the direction of magnetic field is taken to be +z) instead of energy as the eigenvalue. Solving the equation results in complex band structures of constituent materials.

3.2.2 Reference Material and Pseudopotential Calculation

The empirical pseudopotential calculation basically follows that of Cohen[2]. We start with a reference material which has the Hamiltonian

$$H_R \equiv \frac{\vec{P}^2}{2m} + \frac{1}{2}\left[V_a(\vec{r}) + V_b(\vec{r})\right] = \frac{\vec{P}^2}{2m} + \langle V \rangle \tag{3.1}$$

where a and b label the constituent materials, and $V_l(r)$ is the pseudopotential of material l described in terms of pseudopotential form factors. Alloy materials are treated in a virtual crystal approximation. At this stage, spin-orbit interaction, spin-field interaction, and exchange interaction are not included. The reference

Hamiltonian has at $\vec{k} = 0$ eigenfunctions

$$U_\beta(\vec{r}) = \frac{1}{\sqrt{\Omega}} \sum_{\vec{G}} R_{\beta\vec{G}} e^{i\vec{G}\cdot\vec{r}}, \tag{3.2}$$

where β labels the various eigensolutions, Ω is the unit cell volume, $\vec{G}$ is a reciprocal lattice vector, and R is an expansion coefficient. The corresponding eigenvalue of U_β is denoted as ϵ_β. For crystals of zinc-blende structure, $U_\beta(\vec{r})$'s belong to Γ_{15}-representation at the valence band edge, and to Γ_1-representation at the conduction band edge, in the terminology of group theory. They are made to transform like atomic p functions at the valence band edge, and like atomic s functions f(r) at the conduction band edge, under the operations of the tetrahedral group. They are accordingly denoted as X, Y, Z and S. When spin degeneracy is taken into account, we designate them by X↑, X↓, Y↑, Y↓, Z↑, Z↓, S↑, and S↓. These states will be taken as the near-in states while the rest belong to the far-out states.

3.2.3 Effective-Mass Theory of a Bulk Semiconductor in a Magnetic Field

The Hamiltonian

The Hamiltonian H$_l$ of constituent material l in the presence of a magnetic field $\vec{B}$, which is taken to be in z-direction, is

$$\begin{aligned} H_l \;=\; & \frac{(\vec{P} + e\vec{A}/c)^2}{2m} + \langle V\rangle + [V_l - \langle V\rangle] + \frac{\hbar}{4m^2c^2}\left[\nabla V \times (\vec{P} + \frac{e}{c}\vec{A})\right]\cdot\vec{\sigma} \\ & + \frac{e\hbar}{2mc}\vec{\sigma}\cdot\vec{B} + H_\epsilon, \end{aligned} \tag{3.3}$$

where $\vec{A}$ is the vector potential of magnetic field $\vec{B}$, and H_ϵ is the exchange interaction between a band electron and localized d-level electrons. H_ϵ is modeled by

$$H_\epsilon = \sum_j J(\vec{r} - \vec{R}_j)\vec{S}_j \cdot \vec{\sigma}, \tag{3.4}$$

where j labels Mn^{++} sites. Within mean field theory and virtual crystal approximation, we have

$$H_\epsilon = X \left[\sum_j J(\vec{r} - \vec{R}_j) \right] \langle S_z \rangle \sigma_z, \tag{3.5}$$

where X denotes Mn^{++} composition, and j runs over all cation sites since Mn^{++} ions substitute only cations of the crystal in question. Note that $\langle S_x \rangle = \langle S_y \rangle = 0$ since $\vec{B}$ points to z-direction.

Effective-mass Equation

Now with eigenstates of the reference Hamiltonian as basis functions, perturbation calculation can be performed to solve

$$H_l \Phi_l = E_l \Phi_l, \tag{3.6}$$

for each constituent material. Because the Hamiltonian H_l does not possess the translational symmetry of a crystal, the wave function Φ_l becomes a sum of products of envelope functions and cell-periodic Bloch functions:

$$\Phi_l = \sum_\beta C_\beta f_\beta(\vec{r}) U_\beta(\vec{r})$$

with normalization

$$\int_{unit\ cell} U_\beta^*(\vec{r}) U_\beta(\vec{r}) d^3r = \int_\Omega f_\beta^*(\vec{r}) f_\beta(\vec{r}) d^3r = 1. \tag{3.7}$$

The magnetic field B is assumed to be such that the bulk lattice constant is much smaller than the cyclotron radius

$$a \ll (\hbar c/eB)^{1/2},$$

so the cyclotron motion encircles many unit cells. In such case the envelope wave function of an electron has a narrow distribution in $\vec{k}$-space. $f_\beta(\vec{r})$'s are slowly varying on the scale of a unit cell. In other words, $f_\beta(\vec{k}) \approx 0$ when $|\vec{k}| \approx |\vec{G}|$. When putting Eq. (3.7) in Eq. (3.6), we obtain a set of equations for $C_\beta f_\beta(\vec{r})$'s.

We divide the amplitudes $f_\beta(\vec{r})$'s into two sets corresponding to the near-in states and far-out states. We label them by "d" and "α", respectively. We now look for solutions made up mostly of the d-states, i.e., those which contain $C_d f_d(\vec{r})$'s as zeroth-order terms and $C_\alpha f_\alpha(\vec{r})$'s as first-order terms. The use of Löwdin perturbation theory allows us to decouple equations for "d" states from those for "α" states. Zeroth-order terms $C_d f_d$'s satisfy the *effective-mass Hamiltonian equation*:

$$
\begin{aligned}
&\sum_d \Pi_{d'd;l} C_d f_d(\vec{r}) \\
\equiv\ & \sum_d \Bigg[(\epsilon_d \delta_{dd'} + (\vec{P} + \frac{e}{c}\vec{A}) \cdot \overline{\overline{D}} \cdot (\vec{P} + \frac{e}{c}\vec{A}) + \frac{(\vec{P} + e\vec{A}/c)}{m} \cdot \overline{V} + \langle U_{d'} | \Delta V_l | U_d \rangle \\
& + \sum_\alpha \frac{\langle U_{d'} | \Delta V_l | U_\beta \rangle \langle U_\beta | \Delta V_l | U_d \rangle}{\epsilon_0 - \epsilon_\beta} + \frac{\hbar}{4m^2c^2} \langle U_{d'} | (\nabla V \times \vec{P}) \cdot \vec{\sigma} | U_d \rangle \\
& + \frac{e\hbar}{2mc} \langle U_{d'} | \vec{\sigma} \cdot \vec{B} | U_d \rangle + \langle U_{d'} | H_\epsilon | U_d \rangle \Bigg] C_d f_d(\vec{r}) \\
=\ & E_l C_{d'} f_{d'}(\vec{r}),
\end{aligned}
$$

where

$$
\overline{\overline{D}} \equiv \frac{\delta_{dd'}}{2m} + \frac{1}{m^2} \sum_\alpha \frac{\langle U_{d'} | \vec{P} | U_\alpha \rangle \langle U_\alpha | \vec{P} | U_d \rangle}{\epsilon_0 - \epsilon_\alpha},
$$

and

$$
\begin{aligned}
\overline{V} \equiv\ & \langle U_{d'} | \vec{P} | U_d \rangle + \sum_\alpha \frac{\langle U_{d'} | \vec{P} | U_\alpha \rangle \langle U_\alpha | \Delta V | U_d \rangle}{\epsilon_0 - \epsilon_\alpha} + \\
& \frac{\langle U_{d'} | \Delta V | U_\alpha \rangle \langle U_\alpha | \vec{P} | U_d \rangle}{\epsilon_0 - \epsilon_\alpha}.
\end{aligned}
\tag{3.8}
$$

$\Pi_{dd';l}$ is defined in Eq. (3.8). Π_l is called the *effective-mass Hamiltonian.* In Eq. (3.8), there are no terms explicitly coupling f_d with f_α. First-order terms $C_\alpha f_\alpha$'s are related to $C_d f_d$'s by

$$
C_\alpha f_\alpha(\vec{r}) = \frac{1}{\epsilon_0 - \epsilon_\alpha} \sum_d [\frac{(\vec{P} + e\vec{A}/c)}{m} \cdot \langle U_\alpha | \vec{P} + \frac{e}{c}\vec{A} | U_d \rangle +
$$

$$\langle U_\alpha|\Delta V_l|U_d\rangle]C_d f_d(\vec{r}), \tag{3.9}$$

where ϵ^0 is the average energy for the near-in states. Derivation of the effective-mass equation is described in Appendix A.

C-number Matrix Form of the Effective-Mass Equation

Before looking for solutions to the effective-mass equation which, in its present form, is a set of coupled differential equations, we need to cast them into a matrix form involving only c-numbers, which can be handled by linear algebra. This can be best accomplished by making use of quantum numbers. Quantum numbers are associated with operators which commute with the Hamiltonian. When such an operator (say, $\hat{O}$) operates upon the wave function, the operator is replaced by the quantum number:

$$\hat{O}\psi = \lambda\psi. \tag{3.10}$$

Thus, if the Hamiltonian in Eq. (3.8) is expressed in terms of such operators, the differential equation can be transformed into an algebraic equation.

First, let us investigate symmetry properties of the SMSC Hamiltonian. They will allow us to find the accompanying quantum numbers. Let us choose Landau gauge and write

$$\vec{A} = (-By, 0, 0). \tag{3.11}$$

We then observe that, in Eq. (3.8), components of the operator $\vec{K} \equiv (\vec{P}+e\vec{A}/c)/\hbar$ satisfy the following commutation relations:

$$[K_x, K_y] = -[K_y, K_x] = \frac{-ieB}{c}, \tag{3.12}$$

while the others being zero. Since the Hamiltonian H_l given in Eq. (3.3) does not gain extra dependence on x or z with the introduction of a magnetic field, it preserves the translational symmetry both in x-direction and in z-direction for a zinc-blende structure. It suggests that we label each eigenstate of H_l with wave vectors k_x and k_z, and write

$$f_d(\vec{r}) = e^{i\,(k_x X + k_z Z)}\, F_d(y). \tag{3.13}$$

Then, the differential operators P_x and P_z in Eq. (3.8) can be replaced by $\hbar k_x$ and $\hbar k_z$, respectively.

Furthermore, we introduce the creation and destruction operators $\hat{a}^\dagger$ and $\hat{a}$, where

$$\begin{aligned} \hat{a}^\dagger &\equiv \sqrt{\frac{\hbar}{2\omega m}}(K_x + i\,K_y), \\ \hat{a} &\equiv \sqrt{\frac{\hbar}{2\omega m}}(K_x - i\,K_y). \end{aligned} \tag{3.14}$$

Here, $\omega \equiv eB/mc$ is the cyclotron frequency. It can be proved that the creation and destruction operators as defined above satisfy the following property:

$$[\hat{a}, \hat{a}^\dagger] = 1. \tag{3.15}$$

We define the number operator

$$N \equiv \hat{a}^\dagger \hat{a}. \tag{3.16}$$

Moreover, with the new variable $y' \equiv y - \hbar k_x / m\omega$, we have

$$\begin{aligned} \hat{a}^\dagger h_n(y') &= \sqrt{n+1} h_{n+1}(y'), \\ \hat{a} h_n(y') &= \sqrt{n} h_{n-1}(y') \\ N h_n(y') &= n h_n(y'). \end{aligned} \tag{3.17}$$

Here, $h_n(y')$ is the harmonic oscillator function with quantum number n:

$$h_n(y') = (\sqrt{\pi} 2^n n!)^{-1/2} e^{-(1/2)(\sqrt{m\omega/\hbar}\, y')^2} H_n\left(\sqrt{\frac{m\omega}{\hbar}} y'\right). \tag{3.18}$$

On the other hand, K_x and K_y can be expressed in terms of the creation and destruction operators:

$$\begin{aligned} K_x &= \sqrt{\frac{m\omega}{2\hbar}}(\hat{a}^\dagger + \hat{a}), \\ K_y &= -i\sqrt{\frac{m\omega}{2\hbar}}(\hat{a}^\dagger - \hat{a}). \end{aligned} \tag{3.19}$$

Now, let us put Eq. (3.19) back in Eq. (3.8) and replace P_z there by $\hbar k_z$. Then $\hat{a}$ and $\hat{a}^\dagger$ are the only operators involving differentiation in $\Pi_{d'd;l}$.

We can form various linear combinations of the basis functions to facilitate the set-up of Hamiltonian matrix. Kramer basis functions prove to be the most convenient for that purpose. We list them in the following:

$$\begin{array}{ll} U_1(\vec{r}) = |S \uparrow\rangle; & U_2(\vec{r}) = |i\,S \downarrow\rangle; \\ U_3(\vec{r}) = |\frac{1}{\sqrt{2}}(X + i\,Y) \uparrow\rangle; & U_4(\vec{r}) = |\frac{i}{\sqrt{2}}(X - i\,Y) \downarrow\rangle; \\ U_5(\vec{r}) = |\frac{1}{\sqrt{6}}[(X - i\,Y) \uparrow + 2Z \downarrow]\rangle; & U_6(\vec{r}) = |\frac{i}{\sqrt{6}}[(X + i\,Y) \downarrow - 2Z \uparrow]\rangle; \\ U_7(\vec{r}) = |\frac{i}{\sqrt{3}}[-(X - i\,Y) \uparrow + Z \downarrow]\rangle; & U_8(\vec{r}) = |\frac{1}{\sqrt{3}}[(X + i\,Y) \downarrow + Z \uparrow]\rangle. \end{array} \tag{3.20}$$

We introduce a column vector with the transpose

$$(C_1 f_1, C_3 f_3, C_5 f_5, C_7 f_7, C_2 f_2, C_4 f_4, C_6 f_6, C_8 f_8). \tag{3.21}$$

It turns out that, with Kramer basis and the column vector, the effective-mass Hamiltonian Π can be written as

$$\begin{pmatrix} \Pi_a & \Pi_c \\ (\Pi_c)^\dagger & \Pi_b \end{pmatrix}, \tag{3.22}$$

where Π_a, Π_b, and Π_c are all 4×4 matrices.

Let N_m be the number density of cations in the parental nonmagnetic material, $\alpha \equiv \langle S|H_\epsilon|S\rangle/\Omega$ and $\beta \equiv \langle X|H_\epsilon|X\rangle/\Omega$ describing exchange interaction between band electrons and localized d-level electrons, $C \equiv \hbar^2/m$, and $s \equiv eB/\hbar c$. Matrix elements of the 4 submatrices can be written in terms of these parameters.

Let us examine, for example, $(\Pi_a)_{11}$:

$$\begin{aligned}(\Pi_a)_{11} &= 2CsA'(N+\frac{1}{2}) + Cs(N+1) + (A'+\frac{1}{2})Ck_z^2 + \\ &\quad \epsilon_c + \Delta\epsilon_c + \frac{1}{2}XN_m\alpha\langle S_z\rangle. \end{aligned} \tag{3.23}$$

In $(\Pi_a)_{11}$, the first and the second terms describe spin-splitting and Landau level shift. The third term represents the motion in z-direction. $\epsilon_c + \Delta\epsilon_c$ is the conduction band edge. The last term is due to exchange interaction. Values of the various terms are calculated with knowledge of the pseudopotential form factors and eigenfunctions of the reference Hamiltonian in Section (3.2.2).

Here, the average spin $\langle S_z\rangle$ is empirically determined by Brillouin function:

$$\langle S_z\rangle = -S^* B_s(t),$$

where S^* is the effective saturation spin of the magnetic ion and

$$B_s(t) = \frac{2S+1}{2S}\coth(\frac{2S+1}{2S}t) - \frac{1}{2S}\coth(\frac{1}{2S}t), \tag{3.24}$$

with $t = g\mu SB/k_BT^*$. Here, S is the saturation spin of a magnetic impurity, e.g., 5/2 for Mn^{++}. g is the gyromagnetic factor of the magnetic ion. T^* is the effective temperature equal to $T + T_{AF}$. S^* and T_{AF} are empirically determined and account for effects of the formation of antiferromagnetic clusters, which effectively reduces the magnetization. Without any cluster formation, $S^* = 5/2$ and $T_{AF} = 0$.

Solutions to the Effective-Mass Equation

The matrix Π_l can be divided into two parts:

$$\Pi_l = \Pi_l^0 + \Pi_l^1. \tag{3.25}$$

While Π_l^1 can be treated by second-order perturbation theory, we shall neglect it as small. If we neglect B in Π and some of the $\hat{a}^{\dagger 2}$ and $\hat{a}^2$ terms in the off-diagonal matrix elements of Π_a and Π_b (see Appendix A), the effective-mass

Hamiltonian Π reduces to Π^0, which can be solved exactly. It can be proved that the eigenvectors of Π^0 has the following form

$$\frac{1}{\sqrt{N_x N_z}} \begin{pmatrix} C_1 h_n(y') \\ C_3 h_{n-1}(y') \\ C_5 h_{n+1}(y') \\ C_7 h_{n+1}(y') \\ C_2 h_{n+1}(y') \\ C_4 h_{n+2}(y') \\ C_6 h_n(y') \\ C_8 h_n(y') \end{pmatrix} \tag{3.26}$$

in terms of linear harmonic oscillator functions $h_n(y')$'s. For $n = -2$, we put $C_1 = C_3 = C_5 = C_7 = C_2 = C_6 = C_8 = 0$. For $n = -1$, we put $C_1 = C_3 = C_6 = C_8 = 0$. For $n = 0$, we put $C_3 = 0$. The operation of Π^0 on the column vector in Eq. (3.26) creates the same vector multiplied by a c-number matrix. This produces a *c-number matrix form* of the effective-mass equation. However, the inclusion of Π^1 in Π will mix an infinite number of vectors with various n.

The c-number matrix form of the eigenvalue equation can be exactly solved by numerical method. We thus find eigenvalues and eigenstates of the effective-mass Hamiltonian of a SMSC. Each eigenstate is labeled by k_x, k_z, and n, where k_z is a real number.

3.2.4 Examples of Semimagnetic Semiconductor Band Structures

In this section, we apply the above theory to the calculation of a SMSC band structure. We present the band structure of $Cd_{0.78}Mn_{0.22}Te$ in Figure (3.1). The magnetic field is zero. The temperature is taken to be zero. The crystal has the zinc-blende structure. The band structure is similar to that of the nonmagnetic

CdTe. Each band is doubly degenerate. The heavy-hole and light-hole bands are degenerate at the zone center. The band gap is about 1.94eV in comparion to 1.6eV for the CdTe band gap. The subsititution of Cd by Mn simply increases the band gap.

The band structure of $Cd_{0.78}Mn_{0.22}Te$ in the presence of a magnetic field of 5T is shown in Figure (3.2). The Landau index is N = 1. The temperature is taken to be zero to allow for the maximum exchange interaction. The two-fold degeneracy of each band is lifted by the magnetic field. Spin-splitting of each band is enhanced by the exchange interaction due to Mn^{++} ions. Valence bands show anti-crossing behaviour.

3.2.5 The Complex Band Structure of a Semimagnetic Semiconductor

Normally, the eigenstates, with k_z being real, describe propagating states in a bulk semiconductor. The Born-von Karman periodic boundary condition forbids the exsistence of any evanescent states. But in a superlattice, the wave function restricted in the layer of a single material does not have to be freely propagating. Evanescent states are allowed. This point becomes obvious when we think of the quantum mechanics of a step potential. In that case, when the electron does not have sufficient kinetic energy to overcome the barrier height, the wave function is evanescent inside the barrier. It has the form $\exp(-\kappa z)$ with a complex wave vector $i\kappa$. Generalizing this situation to superlattice problem, we need complex band structures of constituent materials to calculate superlattice solutions. Next, we present a mathematical scheme for conveniently calculating the complex band structure.

In the second-order $\vec{k} \cdot \vec{p}$ perturbation theory, the effective-mass Hamiltonian matrix Π is quadratic in k_z. For a given set of k_x, k_z, and n, the effective-mass

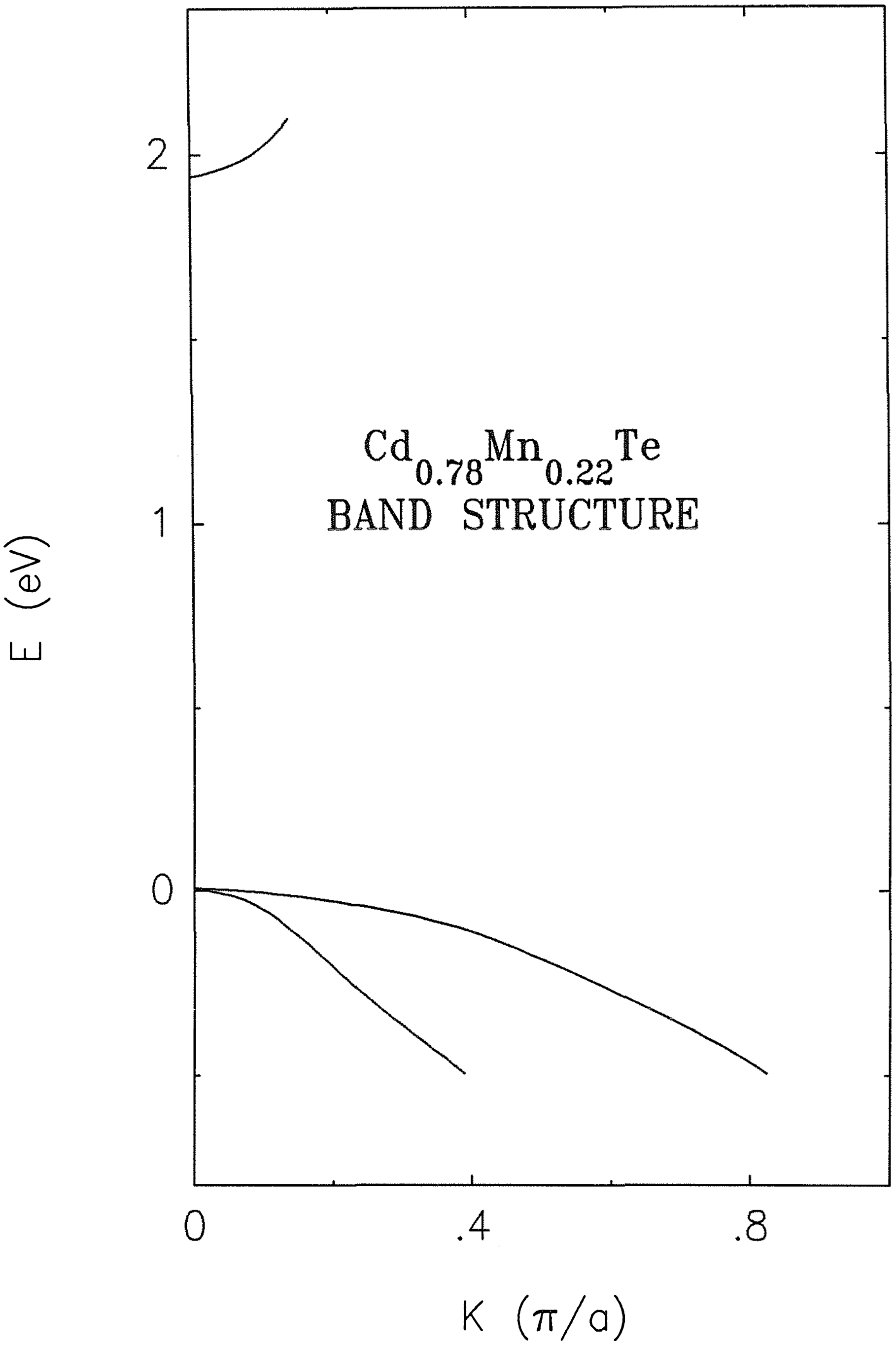

Figure 3.1: The band structure of $Cd_{0.78}Mn_{0.22}Te$ at zero magnetic field. The temperature is taken to be zero. The zero of energy is taken to be at the valence band edge. K is expressed in units of π/a where a is the lattice constant of $Cd_{0.78}Mn_{0.22}Te$.

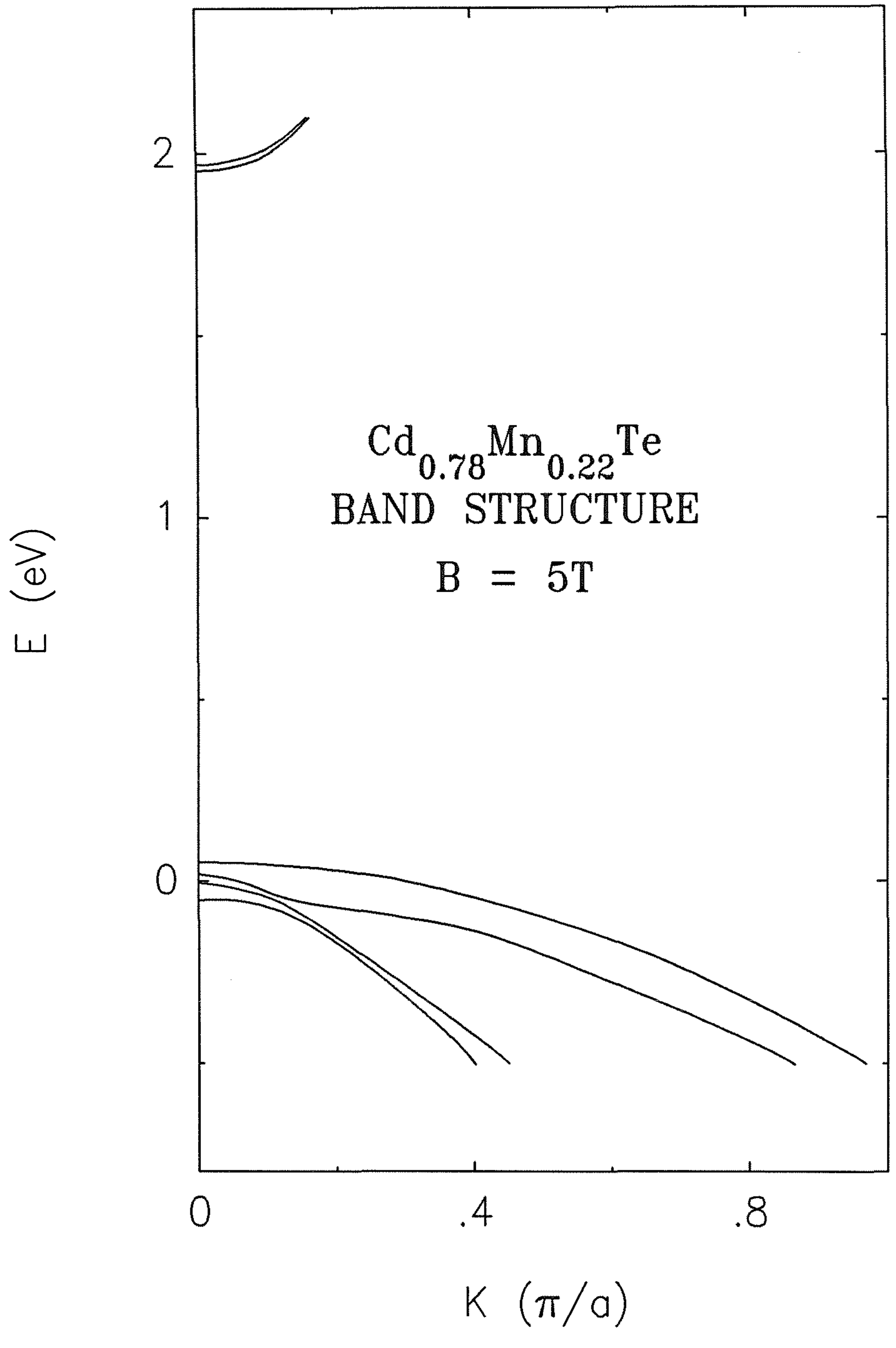

Figure 3.2: The band structure of $Cd_{0.78}Mn_{0.22}Te$ at a magnetic field of 5T. The temperature is taken to be zero. The zero of energy is taken to be at the valence band edge at zero magnetic field. The Landau index is n = 1. K is expressed in units of π/a where a is the lattice constant of $Cd_{0.78}Mn_{0.22}Te$.

equation can be written as

$$EC = \Pi^0 C = \left(H_0 + H_1 k_z + H_2 k_z^2\right) C, \tag{3.27}$$

where H_0, H_1, and H_2 are coefficient matrices and are functions of k_x and n. Here, we use the same symbol Π^0 to denote the corresponding c-number matrix. Eq. (3.27) can be transformed into an eigenvalue equation for k_z, viz.,

$$\begin{pmatrix} 0 & 1 \\ -H_2^{-1}(H_0 - E) & -H_2^{-1}H_1 \end{pmatrix} \begin{pmatrix} C \\ C^{(1)} \end{pmatrix} = k_z \begin{pmatrix} C \\ C^{(1)} \end{pmatrix}, \tag{3.28}$$

where $C^{(1)} \equiv k_z C$. Note that in this equation we have doubled the dimension of the matrix. In a typical calculation, with the Kramer basis functions as near-in states, the H matrices are 8×8 matrices. Thus the matrix in Eq. (3.28) is 16×16. This results in sixteen eigenvalues of k_z for each given set of k_x, n, and E.

Because the various H matrices in Eq. (3.27) are Hermitian, if k_z satisfies Eq. (3.27), so does k_z^*. But it does not necessarily follows that k_z and k_z^* represent different eigenstates. Moreover, if $(C_1 f_1,\ C_3 f_3,\ C_5 f_5,\ C_7 f_7,\ C_2 f_2,\ C_4 f_4,\ C_6 f_6,\ C_8 f_8)$ is the transposed eigenvector corresponding to k_z, then it can be proved that $(-k_z)$ is also an eigenvalue with $(C_1 f_1,\ C_3 f_3,\ C_5 f_5,\ C_7 f_7,\ -C_2 f_2,\ -C_4 f_4,\ -C_6 f_6,\ -C_8 f_8)$ being the transposed eigenvector. The degeneracy of k_z and $(-k_z)$ states can be attributed to the invariance of the Hamiltonian under the operation of reflection with respect to x-y plane.

The invariance of the Hamiltonian can be verified as follows. First, the unitary matrix of the reflection operating on a spinor is $b\sigma_z$, with b being an arbitrary constant with the magnitude of unity. The reflection operation on the spatial part of the wave function changes spatial coordinates x, y and z to x, y and $(-z)$. To verify the invariance of the Hamiltonian, let us examine, for example, the $\vec{\sigma} \cdot \vec{B}$ term in the Hamiltonian. Under the reflection, the magnetic field is not affected, while $\vec{\sigma}$ transforms as follows: $\sigma_x \rightarrow -\sigma_x$, $\sigma_y \rightarrow -\sigma_y$, and $\sigma_z \rightarrow \sigma_z$. Therefore, the $\vec{\sigma} \cdot \vec{B}$ is invariant. We can similarly prove the invariance of other terms in the Hamiltonian.

Therefore, for a given set of k_x, n, and E, we have sixteen eigenvalues, with k_z, $(-k_z)$, k_z^*, and $(-k_z^*)$ always appearing together. If no magnetic field is present, then it can be proved that k_z, $(-k_z)$, k_z^*, and $(-k_z^*)$ always represent different eigenstates, whether k_z is real or imaginary. In such case each real energy band is two-fold degenerate, since there are two different eigenstates for each k_z. Each band is symmetric with respect to $k_z = 0$ due to Kramer degeneracy, i.e., k_z and $(-k_z)$ states are degenerate. However, with a magnetic field, time reversal symmetry is removed. But with the approximation which replaces Π with Π^0, the reflection with respect to x-y plane becomes an element of the symmetry group. With that, k_z and $(-k_z)$ states are degenerate and they represent different states. However, k_z and k_z^* represent the same eigenstate when k_z is real, while k_z and $(-k_z^*)$ represent the same eigenstate when k_z is imaginary.

3.3 Theory of Band Structures of Semimagnetic Semiconductor Superlattices

3.3.1 Outline of the Section

In this section, we describe the calculation of a superlattice band structure based on complex band structures of its constituent materials.

As mentioned in the previous section, an eigenstate in the bulk material can be labeled by three quantum numbers: k_x, k_z, and n. To calculate a superlattice eigenstate, we first select k_x, n, and E, and find all the k_z's through complex band structure calculation. Usually there are sixteen eigenstates for a given energy. A superlattice eigenstate restricted to a constituent material is a linear combination of them.

Upon them we impose boundary conditions and the Bloch condition as well. The boundary conditions are set up through the use of current density matrices. This ensures the continuity of probability current at the interface. The Bloch condition expresses the translational symmetry of the superlattice. It allows us to associate with each eigenstate a wave vector Q in the growth direction of the superlattice. Imposition of these conditions results in an eigenvalue equation. The eigenvalue is $\exp(iQd)$, where d is the superlattice periodicity. The eigenvector is a superlattice wave function. This way we obtain the band structure of a semimagnetic semiconductor superlattice.

3.3.2 Electron Wave Function in a Single Material

Let N_x, N_y, and N_z be numbers of unit cells traversed in going across the sample in x, y, and z direction, respectively. l_y is the y-length of a unit cell. $m(d,n)$ is the index of the oscillator function for d state in n-Landau level. From Eq. (3.9), Eq. (3.13), and Eq. (3.26), the electron wave function for a k_z in material l is given by

$$\begin{aligned}
\Phi_{k_x,k_z,n;l}(\vec{r}) &= \frac{1}{\sqrt{N_x N_z}} e^{i(k_x X + k_z Z)} \left[\sum_d C_d f_d(\vec{r}) U_d(\vec{r}) + \sum_\alpha C_\alpha f_\alpha U_\alpha(\vec{r}) \right] \\
&= \frac{1}{\sqrt{N_x N_z}} e^{i(k_x X + k_z Z)} \sum_d C_d^l F^l_{d;k_x,k_z,n}(\vec{r}),
\end{aligned}$$

with

$$\begin{aligned}
F^l_{d;k_x,k_z,n}(\vec{r}) &= \sqrt{l_y} \left\{ h_{m(d,n)}(y') U_d(\vec{r}) + \frac{\hbar}{m} \sum_\alpha \left[\frac{\left(\vec{K} h_{m(d,n)}(y')\right) \cdot \langle U_\alpha | \vec{P} | U_d \rangle}{\epsilon_0 - \epsilon_\alpha} + \right. \right. \\
&\left. \left. \frac{h_{m(d,n)}(y') \langle U_\alpha | \Delta V^l | U_d \rangle}{\epsilon_0 - \epsilon_\alpha} \right] U_\alpha(\vec{r}) \right\}. \qquad (3.29)
\end{aligned}$$

Normalization of the single material wave function requires that

$$\sum_d |C_d|^2 = 1. \qquad (3.30)$$

To use this wave function in the superlattice problem, however, we need to examine whether extra field is produced by magnetization in the superlattice. From basic magnetostatics,

$$\nabla \cdot \vec{B} = 0. \tag{3.31}$$

In the problem, the magnetic field in a layer is uniform and perpendicular to the layer. Hence, from Eq. (3.31), $\vec{B}$ is continuous at the interface. It follows that the magnetic field is uniform throughout the superlattice. In other words, magnetization in one layer does not influence electronic motion in other layers. The wave function described here is valid for use in the superlattice problem.

3.3.3 Boundary Conditions at Interfaces

Now, we need boundary conditions to connect Φ_l across the interface. Obviously we want J_z, the z-component of the probability current, to be continuous at every interface. The current matrix element between two states, say, $|1\rangle$ and $|2\rangle$, is given by

$$\begin{aligned}\langle 1|J_z|2\rangle &= \frac{1}{2m}\left(\langle 1|P_z + \frac{e}{c}A_z|2\rangle - \langle 2|P_z + \frac{e}{c}A_z|1\rangle\right) \\ &= \frac{1}{2m}\left(\langle 1|P_z|2\rangle - \langle 2|P_z|1\rangle\right),\end{aligned} \tag{3.32}$$

since $A_z = 0$ with Landau gauge. The current density operator $j_z(\vec{r}_0)$ is given by

$$\langle 1|j_z(\vec{r}_0)|2\rangle = \frac{1}{2m}\left[\langle 1|\delta(\vec{r}-\vec{r}_0)P_z|2\rangle - \langle 2|\delta(\vec{r}-\vec{r}_0)P_z|1\rangle\right]. \tag{3.33}$$

Let us define

$$|dk^l_{j,n}\rangle \equiv \frac{1}{\sqrt{N_x N_z}} e^{i(k_x X + k^l_{z;j} Z)} F^l_{d;k_x,k_{z;j},n}(\vec{r}), \tag{3.34}$$

where j denotes one of the sixteen k_z eigenvalues. We shall use the symbol $|dk^l_{j^*,n}\rangle$ to represent the function corresponding to k_z^*. In terms of $|dk^l_{j,n}\rangle$,

$$\Phi_l(\vec{r}) = \sum_d C^l_d |dk^l_{j,n}\rangle. \tag{3.35}$$

Now, let us first calculate $\langle dk^{l}_{j^{*},n}|j_z(\vec{r}_0)|d'k^{l'}_{j',n'}\rangle_A$, the averaged value of the matrix element over a unit cell. Since the superlattice structure preserves the translational symmetry in x-direction, k_x is a quantum number. Hence, in the matrix element, k_x's become the same. For definitiveness, we take $l = a$ and $l' = b$. Putting Eq. (3.34) and Eq. (3.29) in Eq. (3.33), and integrating over y', we get

$$\begin{aligned} &\int dy'_0 \langle dk^{a}_{j^{*},n}|j_z(\vec{r}_0)|d'k^{b}_{j',n'}\rangle_A \\ = \ & \frac{1}{N_x N_z \Omega} e^{i(k^{b}_{j'} - k^{a}_{j})z_0} \frac{1}{\hbar} \left[(H^{a}_{2})_{dd'}(k^{a}_{j} + k^{b}_{j'}) + (H^{a}_{1})_{dd'} - \triangle_{dd'} \right] \delta_{(n,n')} \end{aligned}$$

where

$$\begin{aligned} \triangle_{dd'} \ = \ & \frac{\hbar}{m} \sum_{\alpha} \left[\frac{\langle U_d|P_z|U_\alpha\rangle\langle U_\alpha|\Delta V^b|U_{d'}\rangle}{\epsilon_0 - \epsilon_\alpha} \right. \\ & \left. + \frac{\langle U_d|\Delta V^a|U_\alpha\rangle\langle U_\alpha|P_z|U_{d'}\rangle}{\epsilon_0 - \epsilon_\alpha} \right]. \end{aligned} \tag{3.36}$$

The subscript A means the average over a unit cell of constituent materials. We have listed $\Delta_{dd'}$ in Appendix A.

To calculate the matrix $\int dy'_0 \langle d'k^{a}_{j',n'}|j_z(\vec{r}_0)|dk^{a}_{j^{*},n}\rangle_A$, we simply set the last term in Eq. (3.36) to zero. The matrix $\int dy'_0 \langle d'k^{b}_{j',n'}|j_z(\vec{r}_0)|dk^{b}_{j^{*},n}\rangle_A$ is similarly calculated. The matrix $\int dy'_0 \langle d'k^{b}_{j',n'}|j_z(\vec{r}_0)|dk^{a}_{j^{*},n}\rangle_A$ is found by taking the complex conjugate of $\int dy'_0 \langle dk^{a}_{j^{*},n}|j_z(\vec{r}_0)|d'k^{b}_{j',n'}\rangle_A$.

The boundary condition expressed through the use of current density matrices only couples bulk states with the same n, as indicated by δ function in Eq. (3.36). This allows us to take n as a quantum number for a superlattice eigenstate.

Now, we are in a position to connect wave functions across the interface. Let us consider a heterostructure with only a single interface. In material l, the superlattice wave functions Ψ, with quantum numbers k_x, n, and E, can be written as

$$\Psi(\vec{r}; k_x, n, E) = \sum_{j} D^{l}_{j} \Phi_l(\vec{r}; k_x, n, E, k^{l}_{z;j}), \tag{3.37}$$

where $\Phi_l(\vec{r}; k_x, n, E, k^l_{z;j})$'s are eigenstates in material l given in Eq. (3.29). At the interface, we must have

$$\sum_j D^a_j \Phi^a_j(\vec{r}_0) = \sum_i D^b_i \Phi^b_i(\vec{r}_0). \tag{3.38}$$

Following the same procedure as in Chapter 2, we calculate the current density at the interface and get

$$D^a_j = \sum_i \frac{1}{J^a_{j^*j}} J^{ab}_{j^*i} D^b_i,$$

and similarly

$$D^b_i = \sum_i \frac{1}{J^b_{i^*i}} J^{ba}_{i^*j} D^a_j,$$

where

$$J^{ll'}_{j^*j'} = \sum_{d,d'} (C^l_{dj^*})^* C^{l'}_{d'j'} \langle d k^l_{j^*} | j_z | d' k^{l'}_{j'} \rangle_A. \tag{3.39}$$

From Eq. (3.39), for the two expressions for D^a_j and D^b_i to be consistent, it follows that

$$\sum_i \frac{1}{J^a_{j^*j}} J^{ab}_{j^*i} \frac{1}{J^b_{i^*i}} J^{ba}_{i^*j'} = \delta_{jj'}, \tag{3.40}$$

and

$$\sum_j \frac{1}{J^b_{i^*i}} J^{ba}_{i^*j} \frac{1}{J^a_{j^*j}} J^{ab}_{j^*i'} = \delta_{ii'}. \tag{3.41}$$

3.3.4 Bloch Condition for a Superlattice Wave Function

A superlattice contains infinite number of interfaces. Since the superlattice has translational symmetry in z-direction, a superlattice eigenstate has a superlattice wave vector $\vec{Q}$. From Bloch theorem, the superlattice wave function must satisfy

$$\Psi(\vec{r} + d\hat{z}) = e^{iQd}\Psi(\vec{r}), \tag{3.42}$$

where d is the superlattice periodicity.

3.3.5 Superlattice Eigenvalue Equation

We now choose $z = 0$ at a certain interface, with material A on its left side and material B on its right side. The application of the boundary condition at this interface results in Eq. (3.39). At the next right interface we apply the boundary condition again. With Eq. (3.42) we then obtain at the neighboring interface

$$D_j^a e^{iQ(d_a+d_b)} e^{-ik_j^a d_a} = \sum_i \frac{1}{J_{j^*j}^a} J_{j^*i}^{ab} D_i^b e^{ik_i^b d_b}. \tag{3.43}$$

We combine Eq. (3.39) and Eq. (3.43) together to obtain the *superlattice eigenvalue equation*

$$\sum_{j'} M_{jj'} D_{j'}^a = e^{iQ(d_a+d_b)} D_j^a, \tag{3.44}$$

where

$$M_{jj'} = \sum_i e^{ik_j^a d_a} \frac{1}{J_{j^*j}^a} J_{j^*i}^{ab} e^{ik_i^b d_b} \frac{1}{J_{i^*i}^b} J_{i^*j'}^{ba}. \tag{3.45}$$

This equation can be solved numerically by matrix diagonalization.

3.4 Examples of Semimagnetic Semiconductor Superlattice Band Structures

In this section, we apply the above theory to calculate band structures of the $Hg_{0.95}Mn_{0.05}Te/Cd_{0.78}Mn_{0.22}Te$ superlattice. Cases with and without magnetic field will be shown.

$Hg_{0.95}Mn_{0.05}Te$ is a semimetal with a negative band gap induced by symmetry inversion. $Cd_{0.78}Mn_{0.22}Te$ has the band structure shown Figure (3.1), typical of a zinc-blende structure. The band gap is $1.94eV$. $Hg_{0.95}Mn_{0.05}Te$ has the band structure similar to that of HgTe shown in Chapter 4. The p-s gap is $-0.1eV$.

In Figure (3.3), we show the band structure of the superlattice of $Hg_{0.95}Mn_{0.05}Te/Cd_{0.78}Mn_{0.22}Te$ at $k_{\|} = 0$. The magnetic field is zero. The temperature is taken to be zero. There are five molecular layers of each material in each superlattice unit cell. The Mn^{++} compositions are chosen such that the lattice constants of the two constituent alloys are matched. The strain in each layer is therefore zero.

The mini-band structure is due to zone-folding effect in a superlattice. The first conduction subband, the first light-hole subband, and the first three heavy-hole subbands are shown in the graph. Each subband is actually two-fold degenerate. The band structure shown here is similar to that for a nonmagnetic HgTe/CdTe superlattice, which will be discussed in detail in Chapter 4. The band gap is about 0.7eV.

In Figure (3.4), we show band structure of the $Hg_{0.95}Mn_{0.05}Te/Cd_{0.78}Mn_{0.22}Te$ superlattice at a magnetic field of 5T. The temperature is taken to be zero. The two-fold degeneracy in each band is lifted. There are totally ten subbands shown in the graph. If we compare this graph with Figure (3.3), we see that, near the zone center, the highest and the fourth valence subbands are spin-split bands of the first heavy-hole subband in Figure (3.3). The second and the third subbands are spin-split bands of the light-hole subband. The fifth and the sixth, and the seventh and the eighth are spin-splitted bands of the second and the third heavy-hole subband, respectively. The subbands show anti-crossing behavior. Notice that the conduction subbands are almost degenerate at the zone center in the superlattice. In contrast, the conduction bands in $Cd_{0.78}Mn_{22}Te$ are spin-split as shown in Figure (3.2). This is due to the superlattice structure mixing the s-like and p-like states. The s-like states are split opposite to the way the p-like states are split. The two spin-splittings nearly cancel out each other at the zone center.

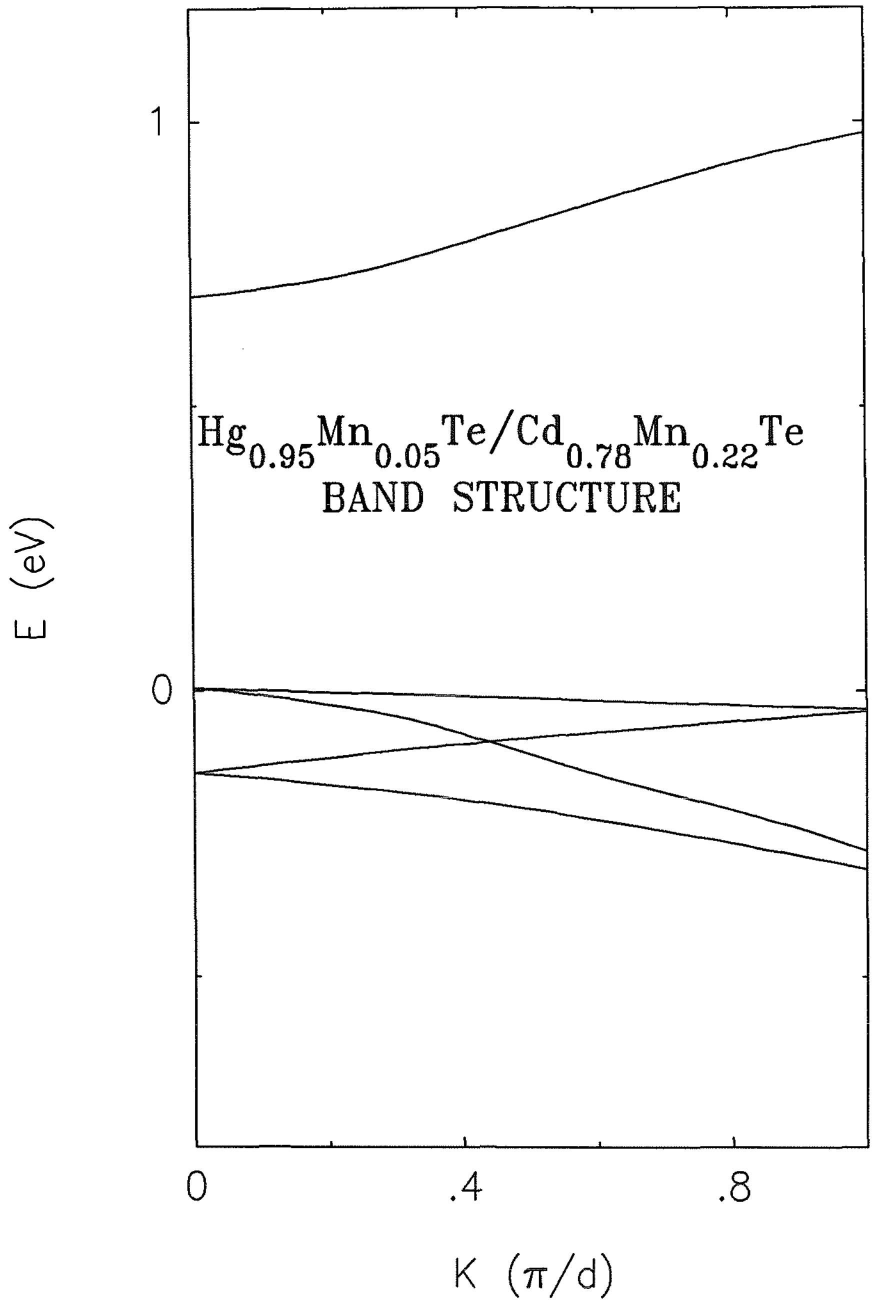

Figure 3.3: The band structure of $Hg_{0.95}Mn_{0.05}Te/Cd_{0.78}Mn_{0.22}Te$ superlattice at $k_{\|} = 0$. There are five molecular layers of each alloy in each superlattice unit cell. The zero of the energy is taken to be the valence band edge of $Cd_{0.78}Mn_{0.22}Te$. The valence band off-set is taken to be zero. K is expressed in units of π/d where d the superlattice periodicity.

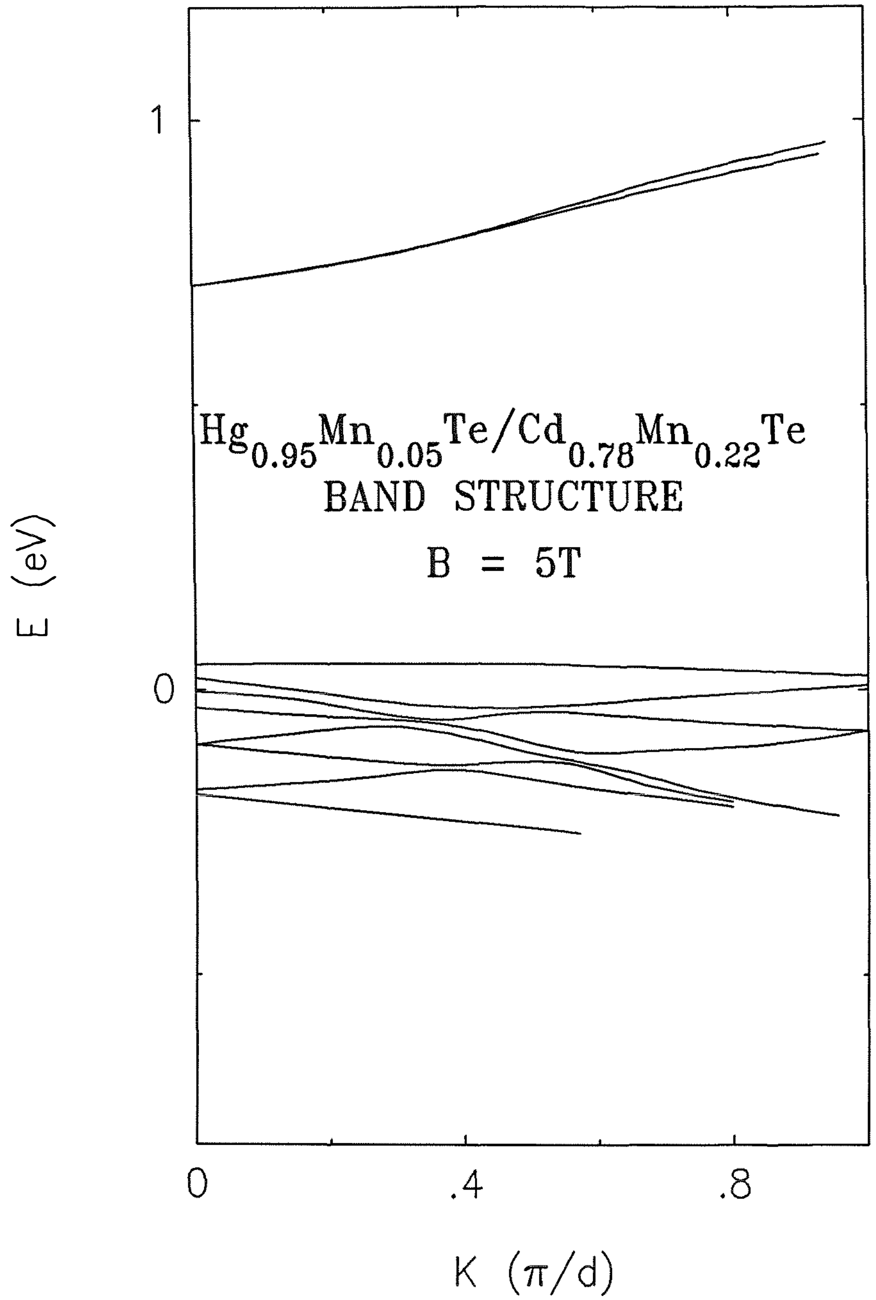

Figure 3.4: The band structure of $Hg_{0.95}Mn_{0.05}Te/Cd_{0.78}Mn_{0.22}Te$ superlattice at $B = 5T$. The Landau index is $n = 1$. There are five molecular layers of each alloy in each superlattice unit cell. The zero of the energy is taken to be the valence band edge of $Cd_{0.78}Mn_{0.22}Te$ at zero magnetic field. K is expressed in units of π/d where d the superlattice periodicity.

3.5 Summary

In summary, the $\vec{k}\cdot\vec{p}$ theory of semimagnetic semiconductor superlattices has been developed. Mean field approximation and virtual crystal approximation are assumed. The effective-mass theory is used to calculate the band structure of a SMSC. The complex band structures of constituent SMSCs are computed prior to the calculation of the superlattice band structure. With approximations, each eigenstate can be labeled by k_x, n and k_z. The complex k_z is calculated for each given set of E, k_x and n. With approximations, only the eigenstates with the same k_x and n are coupled in the presence of the interface. The use of current density matrices ensures the continuity of current at the interface. An eigenvalue equation for the superlattice eigenstate is established. The eigenvalue is $\exp(iQd)$ where Q is the superlattice wave vector in z-direction. The solution to the equation results in the superlattice band structure. Each superlattice eigenstate can be labeled by k_x, n, and Q. The formalism of this chapter can be combined with that of Chapter 2 to treat the band structure of a strained-layer semimagnetic semiconductor superlattice.

Band structures of the bulk $Cd_{0.78}Mn_{0.22}Te$ and the $Hg_{0.95}Mn_{0.05}Te/Cd_{0.78}Mn_{0.22}Te$ superlattice have been shown for both zero and finite magnetic fields. The bands are doubly degenerate with no magnetic field. The degeneracy is lifted by a magnetic field. The bands show anti-crossing behavior.

The method developed in this chapter has been applied to a number of systems, such as $Hg_{1-x}Mn_xTe/Cd_{1-y}Mn_yTe$ and $Cd_{1-x}Mn_xTe/Cd_{1-y}Mn_yTe$ superlattices. The results will be presented in Chapter 5.

References

1. D. L. Smith, G. Y. Wu, T. C. McGill, and C. Mailhiot, Phys. Rev. B (1987), to be published.
2. M. L. Cohen and T. K. Bergstresser, Phys. Rev. **141**, 789 (1966).
3. G. Bastard, C. Rigaux, Y. Guldner, J. Mycielski and A. Mycielski, J. Phys. (Paris) **39**, 87 (1978).

Chapter 4

Theoretical Study of HgTe/CdTe Superlattices

4.1 Introduction

Superlattices of HgTe-CdTe have been proposed as novel materials for application as infrared materials[1,2], particularly those operating at wavelength beyond 10μm. Experimental studies of properties of these superlattices are now underway[3,4]. These man-made systems have the advantage of allowing us to adjust a number of properties of the material so that the interesting features are near optimum for a given application in the infrared. In this chapter, we apply the theory developed in Chapter 2 to analyze the various properties of the HgTe-CdTe superlattice and compare them with those of the alloy.

The conventional infrared material is the HgCdTe alloy, which has disadvantages such as cut-off wavelength fluctuation and relatively large tunneling current. The HgTe has a negative Γ_6-Γ_8 gap while the CdTe has a positive one. Within virtual crystal approximation, the band gap E_g of the $Hg_xCd_{1-x}Te$ alloy is a linear function of the composition: $-0.3x + 1.6(1-x)$. Photons with energy less than the band gap are not absorbed. The cut-off wavelength is determined by the band gap of the alloy:

$$\lambda_c = hc/E_g(x).$$

For detecting infrared light with wavelength of 8-14μm, the band gap must be made near zero. For example, a band gap of 0.1eV gives a cut-off of 12μm. In fact, when the band gap is exactly zero, a singularity exists and the cutoff is infinite. This makes the control of cut-off difficult for infrared absorption. A fluctuation in the composition during growth may result in a relatively large variation in the cut-off. Moreover, in a narrow-gap HgCdTe alloy, effective masses of the light-hole band and the conduction band are directly proportional to the band gap. Thus, as the band gap is made small, so are the effective masses. This increases the leakage current produced by tunneling electrons in a photodiode.

On the other hand, in the case of superlattice, the band gap is controlled by the thicknesses of the HgTe and CdTe layers. The dependence of the cut-off on growth parameters such as layer thicknesses is smooth. Qualitatively, the superlattice can be modeled by a quantum well. The HgTe layers act as potential wells while the CdTe layers are like energy barriers. Or equivalently, the band gap is inversely proportional to the square of the HgTe layer thickness:

$$E_g \propto \frac{1}{L^2}, \tag{4.1}$$

where L is the well thickness. In other words, the cut-off has a square dependence on the HgTe layer thickness:

$$\lambda \propto L^2. \tag{4.2}$$

Although this approximation is not really valid for a HgTe/CdTe superlattice, it does give us some idea about the smooth dependence of the cut-off on growth parameters such as layer thicknesses. Furthermore, the effective mass can be made large with large CdTe layer thickness while the band gap can be made small with wide HgTe layers. With the superlattice, we decouple the unwanted relation between the effective mass and the band gap in the alloy.

The near band-edge optical properties of such superlattices are very important for the applications that are envisioned. The displacement $\vec{D}$ is related to the electric field $\vec{E}$ by

$$\vec{D} = \epsilon \vec{E}, \tag{4.3}$$

in an isotropic dielectric material, where ϵ is the dielectric function. The imaginary part of the dielectric function makes the displacement $\vec{D}$ and the field $\vec{E}$ oscillate in different phases in time. The energy of the field is then absorbed by the material. The optical absorption is roughly proportional to $\epsilon_2(\omega)$, the imaginary part of the dielectric function. For either photoconductive or photovoltaic detectors, the knowledge of light absorption as a function of frequency is required. The function determines amount of the carriers generated by the light and, hence, determines the current or the voltage. The understanding of $\epsilon_2(\omega)$ is thus important for exploration of the superlattice as IR materials.

However, the dielectric function depends on the superlattice band structure which, in turn, depends on the value of the valence band offset. The valence band offset, defined as $\Delta E_v = E_v^{HgTe} - E_v^{CdTe}$ throughout the chapter, describes the relative positions of HgTe and CdTe valence band edges. Therefore, it effectively determines the barrier height in the superlattice problem. In spite of both theoretical and experimental efforts, the precise value of the band offset for this heterostructure is currently not well known.

On the theoretical side, the common anion rule[12,13] states that the location of the valence band edge relative to the vacuum level (energy gap plus electron affinity) depends heavily on the anion of the compound semiconductors and, hence, predicts essentially zero valence band offset for the HgTe-CdTe superlattice. The LCAO theory of Harrison states that the valence band maximum at $\vec{k} = 0$ is given by $E_v = (\epsilon_p^c + \epsilon_p^a)/2 - \{[(\epsilon_p^c - \epsilon_p^a)/2]^2 + V_{xx}^2\}^{1/2}$ where ϵ_p^c is the p-state energy on the metallic atom (cation), ϵ_p^a is the p-state energy on the nonmetallic atom (anion) and the matrix element V_{xx} is an appropriate interatomic matrix element between atomic p states on adjacent atoms[14]. The valence band offset is given by the difference in these absolute energies. The LCAO theory agrees with the common anion rule on the estimated value of the band offset, which is nearly zero. On the other hand, the recent theories of Tersoff[15] and Harrison[16] predict a large valence band offset of $\sim 0.5eV$.

On the experimental side, an early experiment performed by Kuech and McCaldin[17] gave a large value 0.52eV for the upper limit of the valence band offset, but the value could be quite different due to interdiffusion in the sample and inversion at the interface. The recent magneto-optic experiment of Guldner et al[5] concluded that $\Delta E_v = 40meV$. However, recent theoretical work[10] has shown that the failure to include strain in the theoretical work of Guldner et al[5] made the interpretation of their data suspect. On the other hand, the X-ray photoemission spectroscopy (XPS) measurement[6,7] gave 0.35eV for the value of valence band offset.

Thus, the value of the valence band offset could be any number from 0 to 0.5eV. The uncertainty in the band offset leads naturally to the question how sensitive the properties of the superlattice are to the value of band offset.

As to the crystal structure, the lattice constants of HgTe and CdTe are not exactly the same (d^{HgTe} =6.462 Å and d^{CdTe}=6.482 Å), and, hence, there is lattice mismatch in the superlattice. Generally speaking, the layers in the superlattice may be strained with essentially no misfit defect generation if the layers are sufficiently thin and the difference in lattice constants of constituent materials is less than a few percent[18,19]. Superlattices have been grown both on CdTe and

CdZnTe substrates. The CdZnTe substrates are chosen to near lattice match the HgCdTe. The superlattice grown on CdTe produce the largest strain in the HgTe since the HgTe will be under maximum strain and CdTe will be unstrained. We will be considering this case to illustrate strain effects in the superlattice. As commonly known, the strain in the HgTe-CdTe superlattice opens up a band gap in the HgTe and, hence, converts the semimetallic HgTe into a semiconductor. The same phenomenon was found in α-Sn. The conversion of HgTe layers is expected to have effects on the properties of the HgTe-CdTe superlattice.

In Section (4.2), we present the optical properties of the HgTe/CdTe superlattice in terms of the imaginary part of the dielectric function. In Section (4.3), we present the band gap and optical properties of the HgTe-CdTe superlattice as functions of the valence band offset. In Section (4.4), we present a study of strain effects on the band structure, the band gap and optical properties of the HgTe-CdTe superlattice at zero temperature. In Section (4.5), we summarize the study.

4.2 Optical Properties of the HgTe/CdTe Superlattice

In this section, we discuss optical properties of the HgTe/CdTe superlattice, particularly light absorption. The absorption as a function of frequency determines the wavelength cutoff. For intrinsic case, the wavelength cutoff λ_c is determined by the band gap. For wavelengths shorter than λ_c, the incident radiation is absorbed and electron-hole pairs are generated. Hence, knowing the absorption function $\alpha(\omega)$ is important for characterizing an IR material.

The absorption function describes the decay of the incident light intensity as a function of the traversing depth:

$$I(z) = I_0 \exp(-\alpha z).$$

Roughly speaking, the absorption is proportional to the imaginary part of the dielectric function. The absorption function α is related to the imaginary part of dielectric function $\epsilon_2(\omega)$ by the formula

$$\alpha = \frac{\omega \epsilon_2}{cn}, \tag{4.4}$$

where c in the light velocity, and n is the real part of the index of refraction. For a nonabsorptive material, the imaginary part of the dielectric function is zero. The complex index of refraction is

$$n + ik = \sqrt{\epsilon_1 + i\epsilon_2}. \tag{4.5}$$

To determine α, we need not only ϵ_2 but also n, which is a function of both ϵ_1 and ϵ_2. In principle, with the knowledge of $\epsilon_2(\omega)$, the function $\epsilon_1(\omega)$ can be calculated through Kramers-Kronig relation:

$$\epsilon_1(\omega) = \frac{2}{\pi} P \int_0^\infty \frac{s\epsilon_2(\omega)}{s^2 - \omega^2} ds. \tag{4.6}$$

However, this requires full knowledge of $\epsilon_2(\omega)$, i.e., the value of ϵ_2 at any frequency. In practice, we will model $\epsilon_1(\omega)$ very roughly to get some idea about the absorption.

4.2.1 Dielectric Function

We discuss near band edge optical properties. Only interband transitions are considered. Our discussion will center on ϵ_2, which is a second rank tensor. For a zinc-blende crystal, the $\vec{k} \cdot \vec{p}$ theory in first-order approximation gives a band structure which is isotropic in $\vec{k}$ space. Thus ϵ_2 reduces to a scalar. However, the superlattice structure has a unique direction which makes energy bands cylindrically symmetric. Therefore, two independent parameters are necessary for specifying ϵ_2. These two parameters correspond to polarizations of light parallel and perpendicular to the layers, which are denoted as $\epsilon_2^{\parallel}$ and $\epsilon_2^{\perp}$, respectively.

With the assumption that the field spatially varies appreciably only on the scale of a large number of unit cells, perturbation theory gives the expression for ϵ_2:

$$\frac{4\pi^2 e^2}{m^2\omega^2}\sum_{c,v}\int \frac{d^3k}{(2\pi)^3}\delta[E_c(\vec{k}) - E_v(\vec{k}) - \hbar\omega]| < c|\hat{e}\cdot\vec{p}|v > |^2, \tag{4.7}$$

where ω is the photon frequency, c and v refer to degenerate conduction and valence bands, respectively, $\hat{e}$ denotes the direction of polarization and $\vec{p}$ is the momentum operator. If we assume the matrix element is a smooth function of $\vec{k}$, then in the previous equation, we can factor the matrix element out of the integral and get

$$\epsilon_2(\omega) \propto D(\hbar\omega)| < c|\hat{e}\cdot\vec{p}|v > |^2, \tag{4.8}$$

where $D(\hbar\omega)$ is the joint density of states at the energy $\hbar\omega$, describing the number of pairs of states available as initial and final states to the electronic transition

$$E_v(\vec{k}) \rightarrow E_c(\vec{k}) = E_v(\vec{k}) + \hbar\omega.$$

Here only direct transitions are considered. We have neglected the spatial dependence of infrared field, which varies smoothly over a few thousands of Å. Indirect transitions involving phonons or other elementary excitations are higher-order processes, and hence are neglected.

We have studied both $\epsilon_2^{\parallel}$ and $\epsilon_2^{\perp}$ for the superlattice. However, $\epsilon_2^{\perp}$ is found to be smaller than $\epsilon_2^{\parallel}$. For perpendicular polarization, $\langle c1|p_z|hh1\rangle$, the optical matrix element between the heavy-hole-like and conduction subbands, is near zero. Optical transitions between heavy-hole-like and conduction subbands are unlikely. But $\langle c1|p_z|lh1 >$, the matrix element between the first light-hole-like and the first conduction subbands, is finite. Hence, $\epsilon_2^{\perp}$ is primarily determined by optical transitions between the light-hole-like and conduction subbands. Due to the small joint density of states, $\epsilon_2^{\perp}$ is relatively small. However, with parallel polarization, $\langle c1|p_{\|}|hh1 >$ is finite. $\epsilon_2^{\|}$ is determined primarily by optical transitions between the heavy-hole-like and conduction subbands. The large joint density of states results in a relatively large $\epsilon_2^{\|}$. The configuration of parallel polarization is hence preferred for IR detection. The study of optical properties in this chapter will center on $\epsilon_2^{\|}$.

We have calculated ϵ_2 for superlattices in two ways. To evaluate the integral over the first Brillouin zone for ϵ_2, we can perform effective-mass model calculations, assuming that the momentum matrix element is a smooth function of the wavevector, replacing the momentum matrix element with its value at zone center and taking it out of the integral. In the effective-mass approximation, we found that, for the transitions between a valence band i and a conduction band j,

$$\epsilon_2(\omega)_{ij} = A_{ij}\frac{\sqrt{\hbar\omega - E_g}}{(\hbar\omega)^2},$$

where

$$A_{ij} = 4\sqrt{2}(e^2/m^2\hbar)m_{\|}m_{\perp}^{1/2}| < j|\hat{e}\cdot\vec{p}|i > |^2 \tag{4.9}$$

is to be averaged over direction and summed over degenerate bands i and j. Here, $1/m_{\|}$ and $1/m_{\perp}$ are the parallel and perpendicular components to the interface of $1/m_j - 1/m_i$, repectively. m_j and m_i are the effective masses. The dielectric function of the alloy can be calculated in a similar way. In such case, the band structure is taken to be isotropic. So the parallel and perpendicular masses are equal.

We can also employ an interpolation scheme similar to that proposed by Raubenheimer and Gilat[8] and calculate the integral in Eq. (4.7). The difficulty with ordinary schemes for numerical integration (such as Simpson's rule) is that the integral, involving a δ function, makes the numerical convergence very slow. The scheme of Raubenheimer et al speeds up the convergence.

4.2.2 Band Structures of HgTe, CdTe and HgCdTe

Band-edge features for the valence band and conduction band of HgTe and CdTe are shown in Figure (4.1). The valence band edges are tentatively aligned to reflect the smallness of the valence band offset. CdTe is a wide gap semiconductor; whereas, HgTe is a symmetry-induced zero gap semiconductor. In CdTe, the states at the valence band maximum and at the conduction band minimum have Γ_8 and Γ_6 symmetries, respectively. The Γ_6-states are conduction band edge states which transform like atomic s functions. The Γ_8-states include heavy-hole ($|3/2,\pm 3/2\rangle$) and light-hole ($|3/2,\pm 1/2\rangle$) states. The Γ_7-states are split-off ($|1/2,\pm 1/2\rangle$) states. The $\vec{k}\cdot\vec{p}$ matrix element between the $|S\uparrow\rangle$ ($|S\downarrow\rangle$) function of Γ_6 symmetry and the $|3/2,1/2\rangle$ ($|3/2,-1/2\rangle$) function of Γ_8 symmetry pushes the conduction band and the light hole band away from each other. However, in HgTe the states at the valence band maximum and at the conduction band minimum both have Γ_8 symmetry. The states of Γ_6 symmetry lie below the Γ_8 edge in HgTe. This is because the relativistic effect in HgTe is so large that it brings down the Γ_6 states below the Γ_8 states. Again the k.p matrix element makes them curve away from each other. The heavy hole band remains curving down since the heavy-hole states do not couple to the Γ_6 states.

The interband optical matrix element in HgTe at k=0 is given by $\langle\Gamma_8|p|\Gamma_8\rangle$. This matrix element, while not zero, is known to be small. The optical absorption in CdTe is governed by $\langle\Gamma_6|p|\Gamma_8\rangle$ which is quite large. The band structure of a HgCdTe alloy with a positive Γ_6-Γ_8 gap is similar to that of CdTe except that the band gap is smaller. The value of the momentum matrix element remains the same in zero-order approximation. However, the joint density of states, being

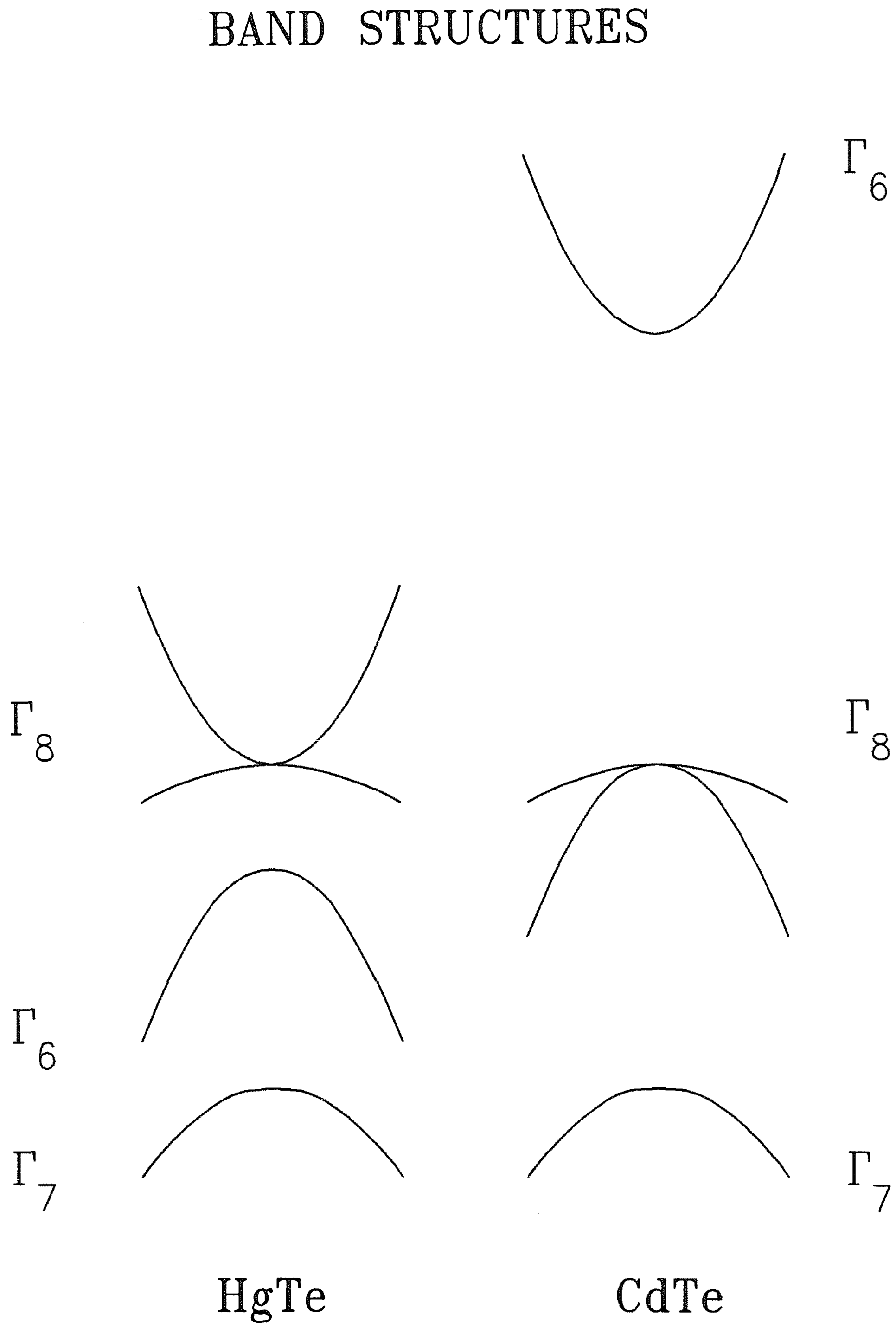

Figure 4.1: Band structure for HgTe and CdTe near the center of the Brillouin zone for HgTe-CdTe superlattices. Band offsets and symmetries of bulk states are also shown.

proportional to $m^{*3/2}$ (or ${E_g}^{3/2}$), is small for the alloy with a small band gap.

4.2.3 Band Structure of a HgTe/CdTe Superlattice

In Figure (4.2), we show the band structure of a representative superlattice. The calculation was carried out for 14 layers of HgTe and 4 layers of CdTe. The band offset is taken to be 40meV and the strain in the layers is taken to be zero. Energy dispersions are shown for both wave vectors perpendicular to the layers k_z (measured in units of π/d_{SL}, where d_{SL} is the total thickness of each repeat of the superlattice, 60Å in this case) and for wave vectors parallel to the layers k_x (measured in units of π/a, where a is the lattice constant of bulk HgTe, approximately 6.42Å). The superlattice has a direct band gap. Zone-folding effects in the superlattice growth direction are clearly illustrated in the graph. This results in a mini-band structure. The dispersion in z-direction is relatively flat. In the superlattice with a small gap, with the assumption of small valence band offset, the valence band states have almost pure Γ_8-character, while the conduction band states have finite Γ_6-character in the HgTe layer and primarily Γ_8-character in the CdTe layer. Hence, the optical matrix element is finite but smaller than that for the alloy. The thicker the HgTe layer, the larger the matrix element. On the other hand, since the CdTe layer is the potential barrier, the thicker the CdTe layer, the larger the perpendicular effective mass and the joint density of states.

4.2.4 Comparison of Superlattices and Alloys

In this section, we present the comparison of optical properties of the HgTe/CdTe superlattice and the HgCdTe alloy. As mention, the alloy has a small joint density of states and a large optical matrix element, while the superlattice has a reduced optical matrix element and a large joint density of states. From

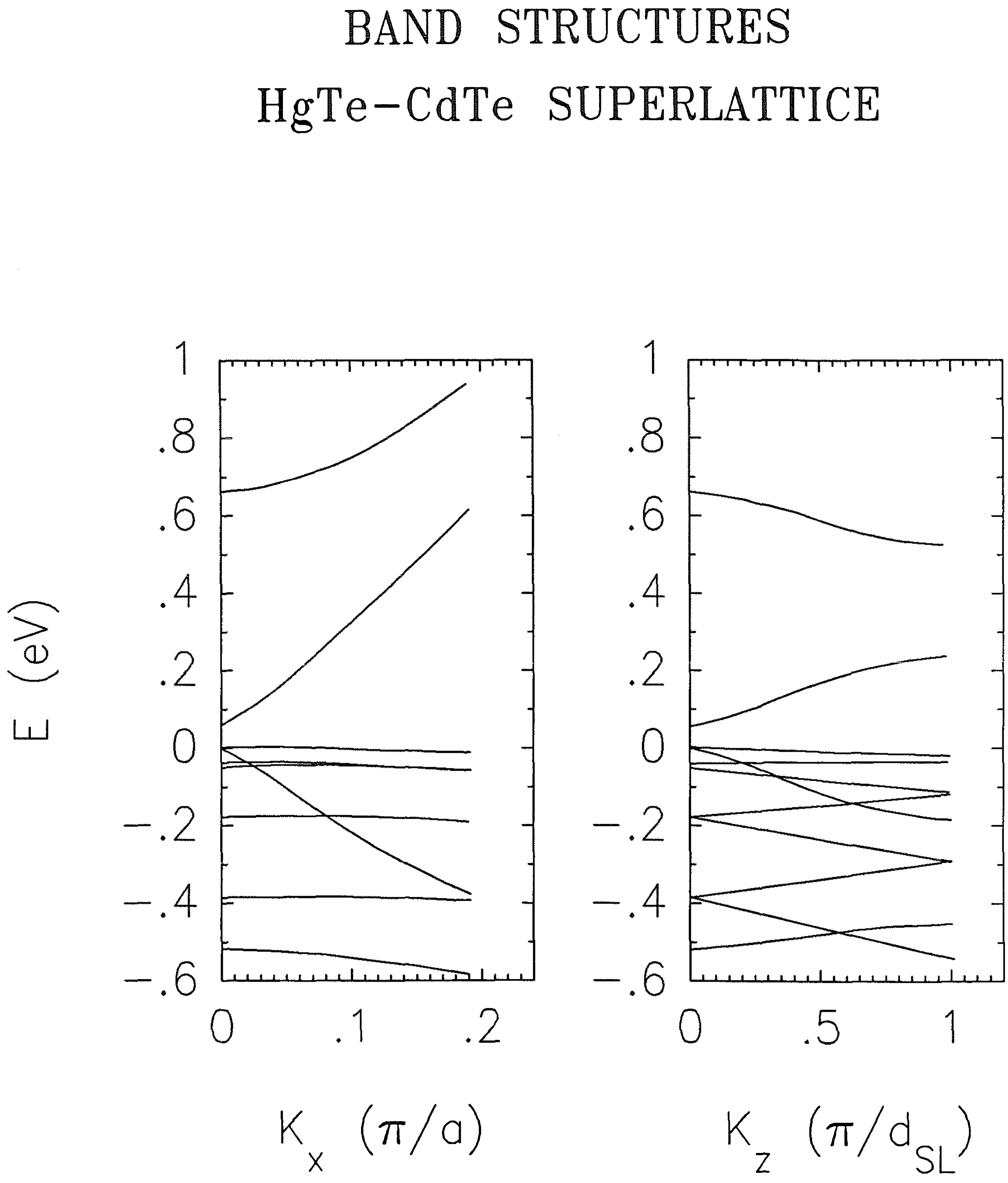

Figure 4.2: Band structure of a representative superlattice. The zero of energy is taken to be the valence band edge. Dispersion for wave vectors perpendicular to the layers k_z and for wave vectors parallel to the layers k_x are both shown.

Eq. (4.8), the dielectric functions for the superlattice and the alloy might be comparable. We have carried out numerical evaluation of dielectric functions.

The results of our study are presented in Figures (4.3) and Figure (4.4). In Figure (4.3), we have plotted the near band edge values of $\epsilon_2^{\|}(\omega)$ for a wide band gap superlattice made up of 38.5 Å thick layers of HgTe alternating with 38.5 Å thick layers of CdTe. The resulting superlattice has a band gap at 0.233 eV. The polarization of the light is parallel to the layers. For comparison, the results for an alloy with the same band gap are shown. The important result of this calculation is that the magnitude of $\epsilon_2^{\|}(\omega)$ for the superlattice is comparable to that of the alloy.

In Figure (4.4), we present the results for a superlattice containing 70.6 Å thick layers of HgTe and 70.6 Å thick layers of CdTe in one unit cell. This superlattice has a small band gap about equal to 0.107eV. The cut-off wavelength is about 12μm. The polarization of the light is parallel to the layers. The exciting results are that the superlattice has $\epsilon_2^{\|}(\omega)$ larger than that for the alloy.

To compare the absorption, we need, as mentioned, to calculate n or ϵ_1. In principle, ϵ_1 can be calculated through the use of Kramers-Kronig relation if ϵ_2 is given for all frequencies. But in fact, we do not fully know the imaginary part of the dielectric function. It can be calculated only if we know the band structure of the superlattice over the whole range of energy. We need to make rough approximation to estimate n. We assume that n of the superlattice is about equal to that of the alloy, since n does not change by orders of magnitude with semiconductor materials.

Hence, with the assumption about n, we get some idea about the absorption by calculating only ϵ_2. Optical properties of the superlattice near the band edges are such that the absorption may be comparable to or even bigger than that for the alloy.

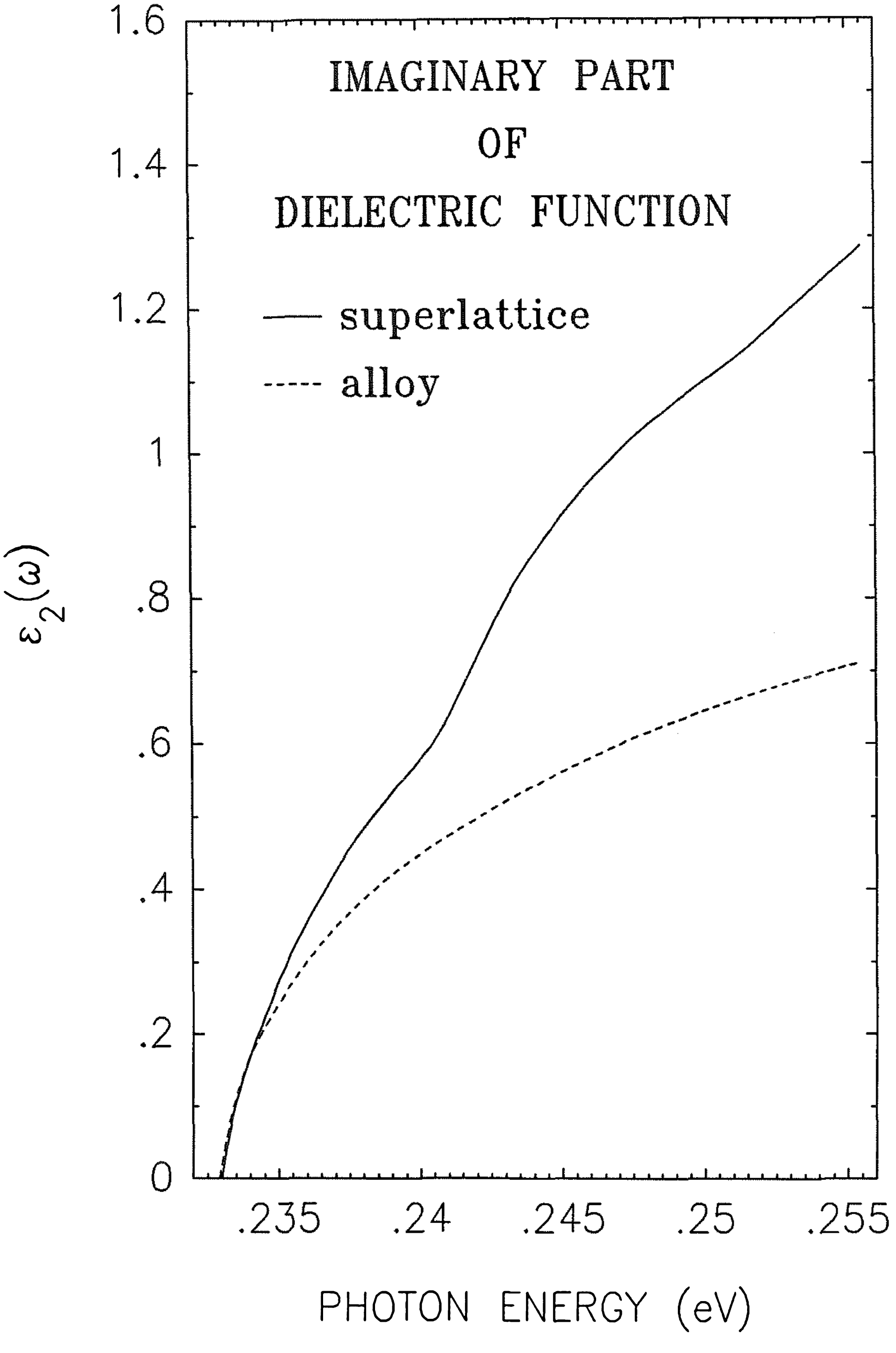

Figure 4.3: Predicted $\epsilon_2^{\parallel}$ vs. photon energy. The superlattice is made up of an alternating structure consisting of layers of HgTe 38.5 Å thick and layers of CdTe 38.5 Å thick. The superlattice has a band gap of 0.233 eV. For comparison, ϵ_2 for the alloy of the same gap is also plotted.

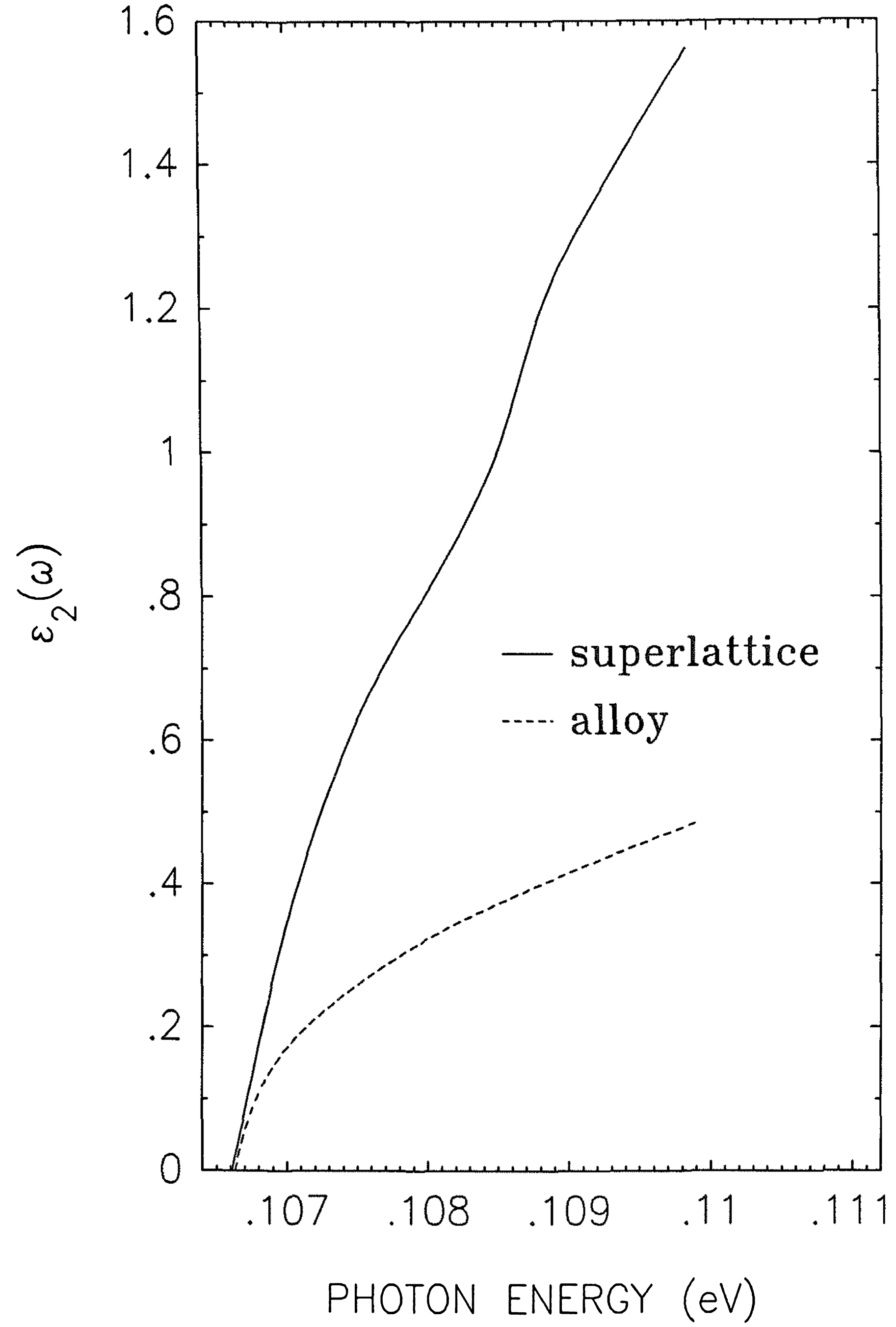

Figure 4.4: Predicted $\epsilon_2^{\parallel}$ vs. photon energy. The superlattice is made up of an alternating structure consisting of layers of HgTe 70.6 Å thick and layers of CdTe 70.6 Å thick. The superlattice has a band gap of 0.107 eV. For comparison, ϵ_2 for the alloy of the same gap is also plotted.

4.3 Band Offset and Optical Properties

In the previous section, we have assumed that the valence band offset is zero. As mentioned, the offset of HgTe valence bands with respect to those of CdTe varies from 0 to $0.5eV$. In this section, we examine the effect of variation in the band offset on the band gap and optical properties of the HgTe-CdTe superlattice. We have calculated the band gap and optical properties of the superlattice with the band offset ($\Delta E_v = E_v^{HgTe} - E_v^{CdTe}$) varying around zero.

In Figure (4.5), we show the band gap as a function of the band offset for three superlattices with unit cells composed of 50 Å HgTe and 50 Å, 50 Å HgTe and 25 Å CdTe, and 50 Å HgTe and 75 Å CdTe, respectively. As the valence band offset becomes negative, the conduction and the valence band edges move toward each other. As the band offset becomes positive, both edges move in the same direction. But the valence band edge moves more in the energy. As shown in the figure, the band gap has a maximum at $\Delta E_v = 0meV$ and decreases by a small amount with respect to a variation in ΔE_v around zero. In contrast, the variation in band gap with $\Delta E_v < 0meV$ is faster than that with $\Delta E_v > 0meV$.

In Figure (4.6), we show optical properties as a function of the band offset. Only transitions from the heavy-hole-like band to the first-conduction band are considered, since they determine near band-edge absorptions. The effective mass of the valence band is taken to be infinite compared to the effective mass of the conduction band. A is plotted versus the band offset for the superlattice with alternating layers of 50 Å HgTe and 50 Å CdTe. The electric field is taken to be parallel to the interface. It is found that A is a slowly varying function with $\Delta E_v > 0meV$ around zero. However, A decreases relatively fast as ΔE_v becomes negative. This has to do with the fact that the electron and the hole are confined in different layers, namely, HgTe and CdTe layers, respectively, in the case of negative ΔE_v. The recombination rate of the electron and the hole

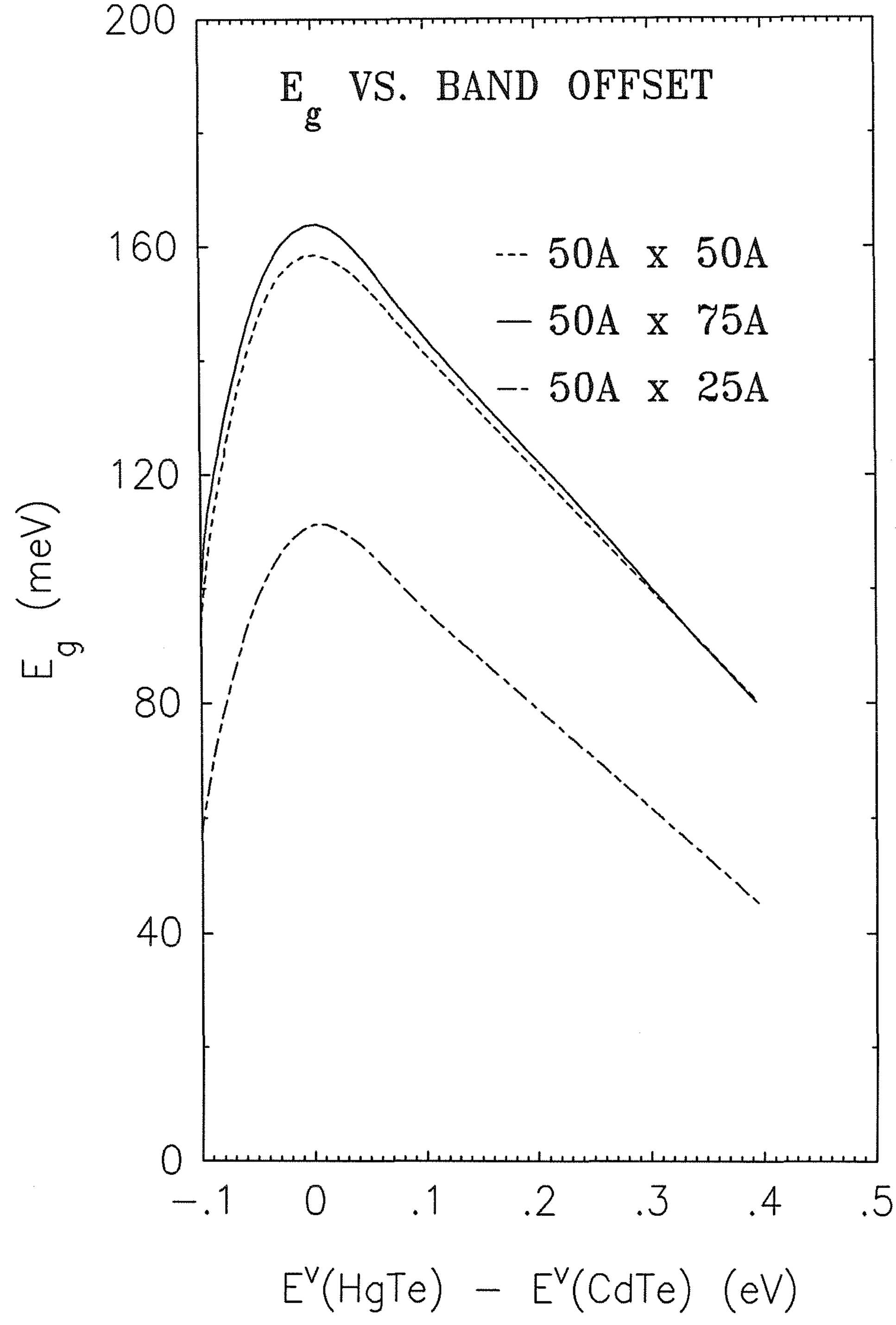

Figure 4.5: The band gap as a function of the band offset for three superlattices with unit cells composed of 50 Å HgTe and 50 Å, 50 Å HgTe and 75 Å CdTe, and 50 Å HgTe and 25 Å CdTe.

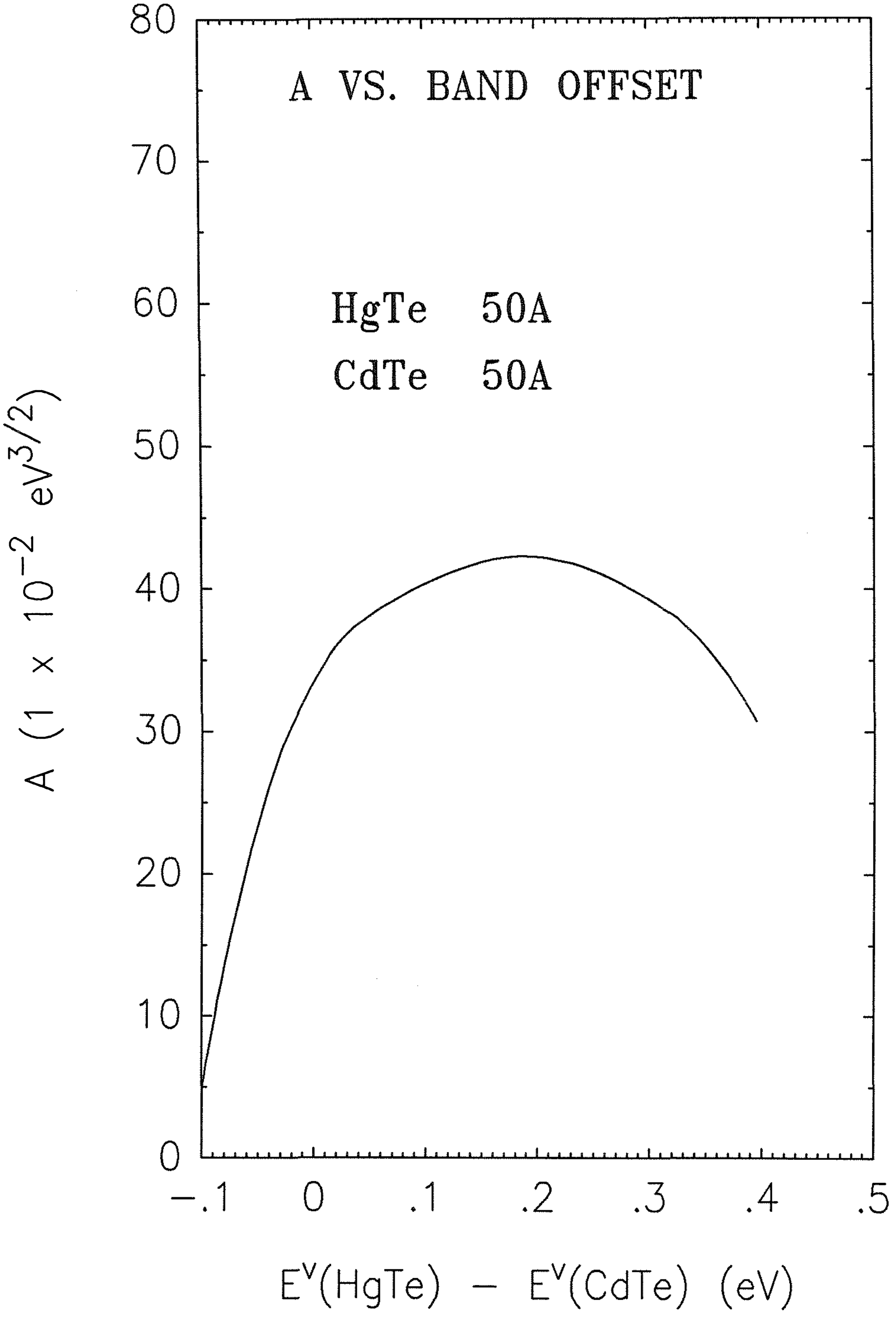

Figure 4.6: A is plotted versus the band offset for the superlattice with alternating layers of 50 Å HgTe and 50 Å CdTe. The electric field is parallel to the layers.

is decreased. This results in a small optical transition rate, and hence small ϵ_2.

4.4 Strain Effects and Optical Properties

The HgTe/CdTe superlattices have been fabricated on two different substrates, CdTe and CdZnTe. The CdZnTe have Zn concentrations which make the lattice constant of the substrate nearly match the average lattice constant of the HgTe-CdTe superlattice. In this section, we examine the role of strain in the HgTe layers in HgTe-CdTe superlattices grown on CdTe substrates. We will discuss the effects of strain on the band structure, the band gap and optical properties of the superlattice. The CdTe substrates result in the largest strain in the HgTe layers of the superlattice. The lattice constant of the overall superlattice structure is that of the CdTe. The strain is in the HgTe layers only. CdTe layers are unstrained.

In Chapter 2, we have seen that the strain in the CdTe/ZnTe superlattice pushes the light-hole band upward in the ZnTe which, having the smaller lattice constant, is under biaxial tensile stress. In a HgTe/CdTe superlattice grown on CdTe substrate, the HgTe layer, with the smaller lattice constant, is also under biaxial tensile stress. The conduction band in the HgTe actually has the light-hole band character (recall the inversion of Γ_6-symmetry and Γ_8-symmetry shown in Figure (4.1). It gets pushed upwards by the strain. Thus a finite band gap is opened up. This results in a strain-induced semimetal-semiconductor transition. As a result, some features of the superlattice band structure may change with the presence of a strain. In Figure (4.7), a strained HgTe band structure is shown. The strain is taken to be the same as that in the HgTe layer in a (111) HgTe/CdTe superlattice grown on CdTe substrate. HgTe, with the smaller lattice constant, has a positive volume dilation. With that, the Γ_8-levels,

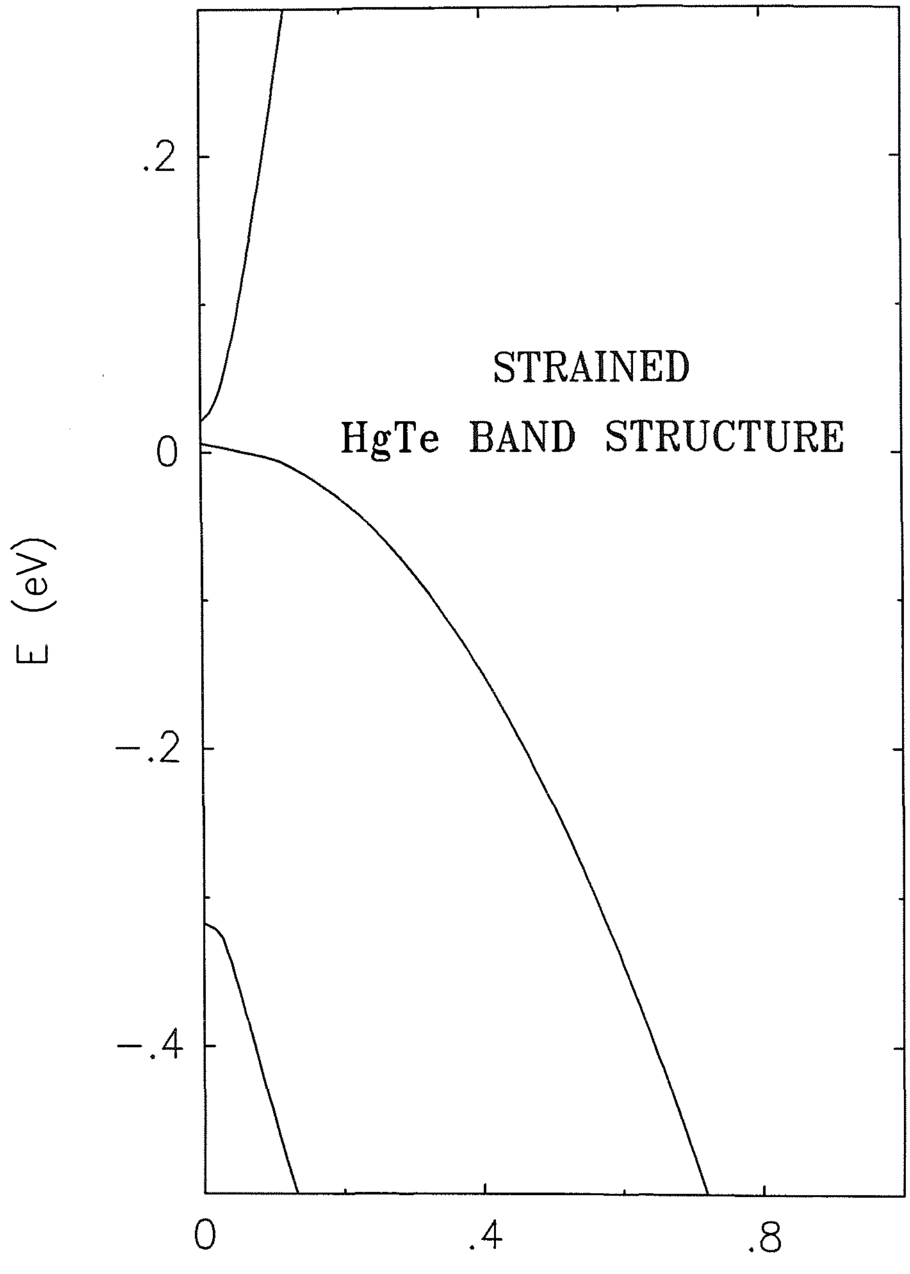

Figure 4.7: The band structure at zero $\vec{k}_{\parallel}$ for the strained HgTe. The dispersion is along the growth direction of the superlattice. The strain is that in the HgTe layer in a superlattice grown on a (111) CdTe substrate. a is the lattice constant of the bulk HgTe. The band gap is around 14meV.

being bonding orbitals in LCAO (linear combination of atomic orbitals) picture, become higher in energy. Figure (4.7) shows that the center of weight of Γ_8-states is pushed up compared to that in unstrained HgTe, which is taken to be zero in the energy scale. However, the Γ_6-levels are anti-bonding orbitals. The energy decreases with a positive volume dilation. The band gap opened up by the strain is approximately 14meV. We expect strain induces the same order of magnitude changes in superlattice band structures. They are discussed in the next paragraph.

In Figure (4.8), we show the band structures at zero $\vec{k}_{\parallel}$ for the superlattice grown on a (111) CdTe substrate. There are 180 Å of HgTe and 44 Å of CdTe in each unit cell of the superlattice. This particular superlattice was chosen, since it was the one studied by Guldner et al[5]. On the left of Figure (4.8), we show the band structure for the unstrained superlattice with zero valence band offset. The structure agrees with the result of Guldner et al[5]. The band gap is near zero. The top two valence subbands are accidentally degenerate due to the choice of zero valence band offset in our calculation. The highest valence subband is derived from $|3/2, 3/2>$ and $|3/2, -3/2>$ heavy hole bands of HgTe and CdTe, and the second valence subband is related to $|3/2, 1/2>$ and $|3/2, -1/2>$ light hole bands of HgTe and CdTe. As shown on the right of Figure (4.8), the band structure for the strained superlattice shares some common features with that of the unstrained one. The strained superlattice has a direct band gap. The band gap is about zero. The effective masses of the electron and the hole are about $0.002m_e$, and the effective mass of the heavy hole is about $2m_e$ for the motion perpendicular to the layer. The effective mass of the electron is about $0.007m_e$ for the motion parallel to the layer. These values are comparable to those for the unstrained superlattice. However, interesting differences are observed in the strained superlattice band structure. The degeneracy of the two valence

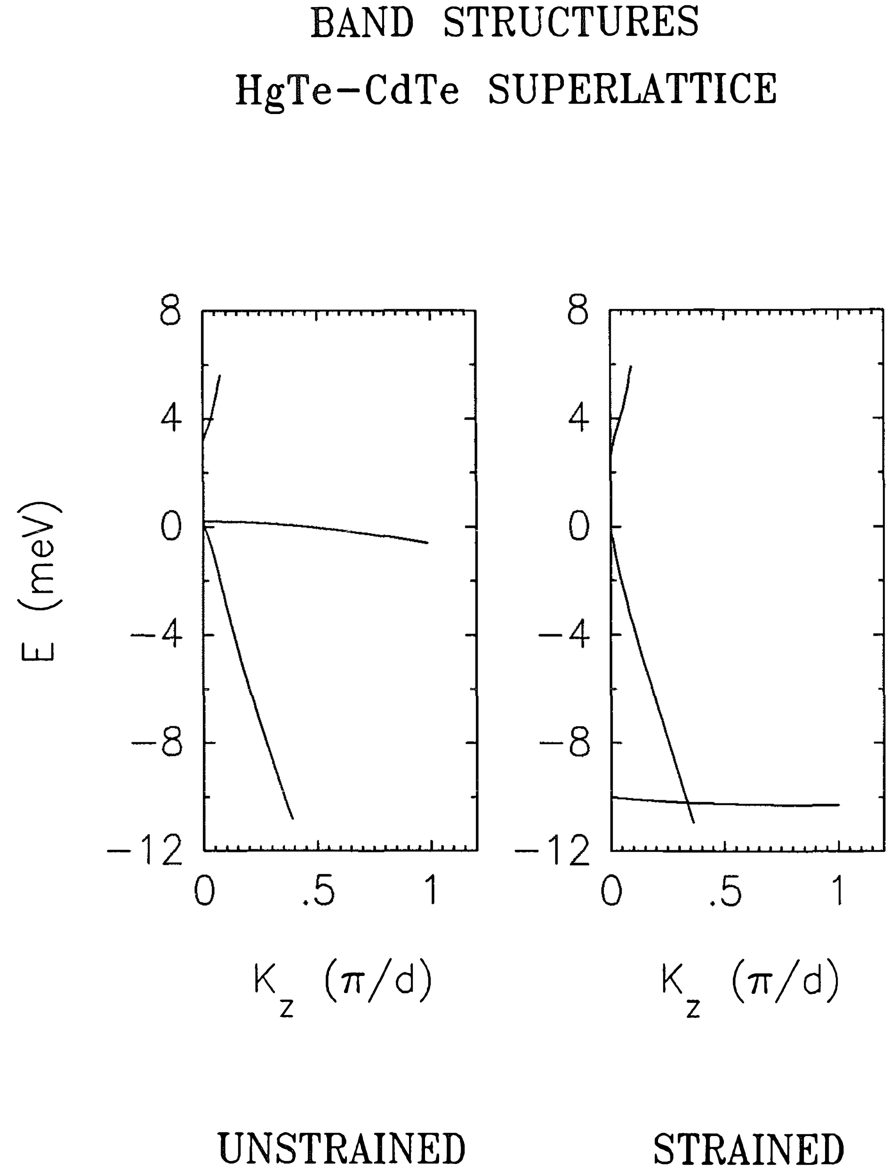

Figure 4.8: The band structure at zero $\vec{k}_{\|}$ is shown for the superlattice grown on a (111) CdTe substrate. d_{SL} is the lattice constant of the superlattice. There are 180 Å HgTe and 44 Å CdTe in each unit cell of the superlattice. On the left is the band structure for the unstrained superlattice. The band gap is about 3meV. The top two valence subbands are degenerate in our calculation. On the right is the band structure for the strained superlattice. The band gap is about 2.7meV. The separation between the top two valence subbands is 10meV.

subbands is lifted. The separation between the two valence subbands is 10meV. The upper valence subband is light-hole-like while the lower one is heavy-hole-like for wave vectors perpendicular to the layer. For the motion parallel to the layer, the effective mass of the hole of the upper valence subband is $0.05m_e$ which is larger than that of the lower one $0.006m_e$. We have also studied the band structure of the (001) strained superlattice of the same composition. It has a band structure similar to that of the (111) strained superlattice. The band gap is 2meV. The separation between the two valence subbands is 14meV. We would like to stress that the band structure plotted here for the strained superlattice is qualitatively different from that obtained under the conditions of zero strain and 40meV offset by Guldner et al[5]. Guldner et al[5] obtained an inverted valence band structure in which the upper valence band is heavy-hole-like. Consequently, the effective masses of the subbands occur in different order in the two cases. In a magneto-optical experiment, the valence band offset is determined by adjusting its value to fit various observed transitions between Landau levels. The adjustment depends on effective masses of the subbands. Therefore, the difference in the order of effective masses may lead to a new value of band offset. Interpretation of magneto-optic data with a model including strain is important for extracting the correct value.

In Figure (4.9), we present the band structures at zero $\vec{k}_{\|}$ for the (111) superlattice consisting of alternating layers of 70.6 Å of HgTe and 70.6 Å of CdTe. The band structure of the unstrained superlattice with zero valence band offset is shown on the left of Figure (4.9). The band gap is about 0.1eV. The top two valence bands are degenerate in our calculation. The band structure of the strained superlattice is shown on the right of Figure (4.9). The strained superlattice has a direct band gap. The highest valence subband is light-hole-like and the second valence subband is heavy-hole-like for the motion perpendicular to

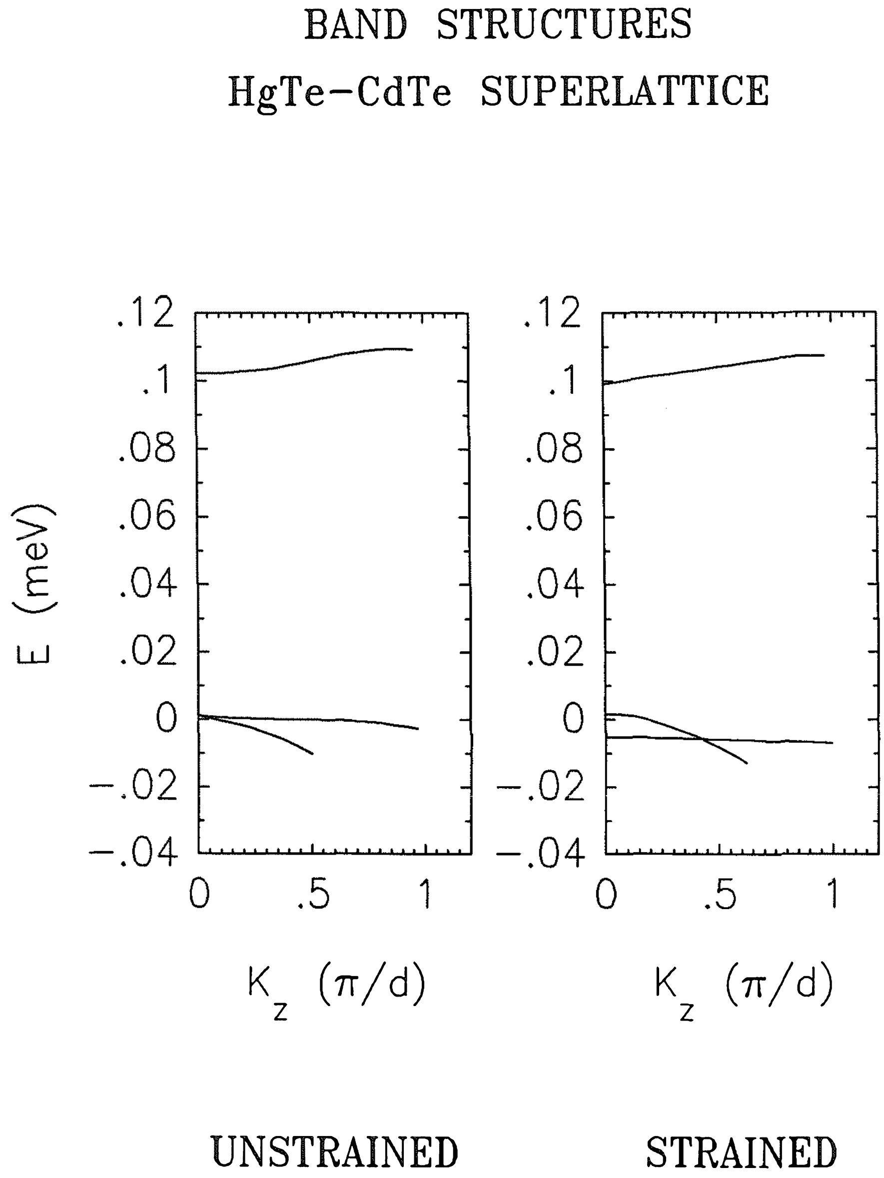

Figure 4.9: The band structures at zero $\vec{k}_{\|}$ for the (111) superlattice consisting of alternating layers of 70.6 Å HgTe and 70.6 Å CdTe. d_{SL} is the lattice constant of the superlattice. On the left is the band structure for the unstrained superlattice. The band gap is about 0.1eV. The top two valence subbands are degenerate in our calculation. On the right is the band structure for the strained superlattice. The band gap is 3meV less than that in the unstrained superlattice. The two valence subbands are separated by 7meV.

the layer. This superlattice has a band gap which is 3meV less than that in the unstrained superlattice. The two valence subbands are separated by 7meV. The effective masses of the electron for motions perpendicular and parallel to the layer are about $0.1m_e$ and $0.03m_e$, respectively. For the motion perpendicular to the layer, the hole of the first subband has an effective mass $0.06m_e$, while that of the second subband has one about m_e. For the motion parallel to the layer, the hole of the second subband has an effective mass about $0.08m_e$, while that of the first subband has a larger one about $0.5m_e$. Strain effects on the band gap are not big for a thin-layer superlattice such as the one discussed here. Shift on the order of 10meV in some of the energy bands is caused by the strain. For the (001) superlattice of the same composition, the band gap is 95meV, and the two valence subbands are separated by 12meV.

In Figure (4.10), we show $\epsilon_2^{\|}(\omega)$, the imaginary part of the dielectric constant for the electric field polarized parallel to the layers, for the superlattice whose band structure is plotted on the right of Figure (4.9). The curve shows that the superlattice is direct with $\epsilon_2^{\|}(\omega) \propto (\hbar\omega - E_g)^{1/2}$ near the band edge. At higher frequencies $\epsilon_2^{\|}(\omega)$ increases more rapidly as the transitions between the second valence band and the conduction band begins to contribute to ϵ_2. Only direct transitions are included in the calculation. Since the superlattice is direct, the largest contribution will come from the direct transitions. Hence, we expect the inclusion of indirect transitions will make a small change in the results which are obtained. Results given here are similar to those obtained in the previous calculation which assumed zero strain. We again found that $\epsilon_2^{\|}(\omega)$ of the superlattice under the strain is comparable to that of the HgCdTe alloy with the same band gap.

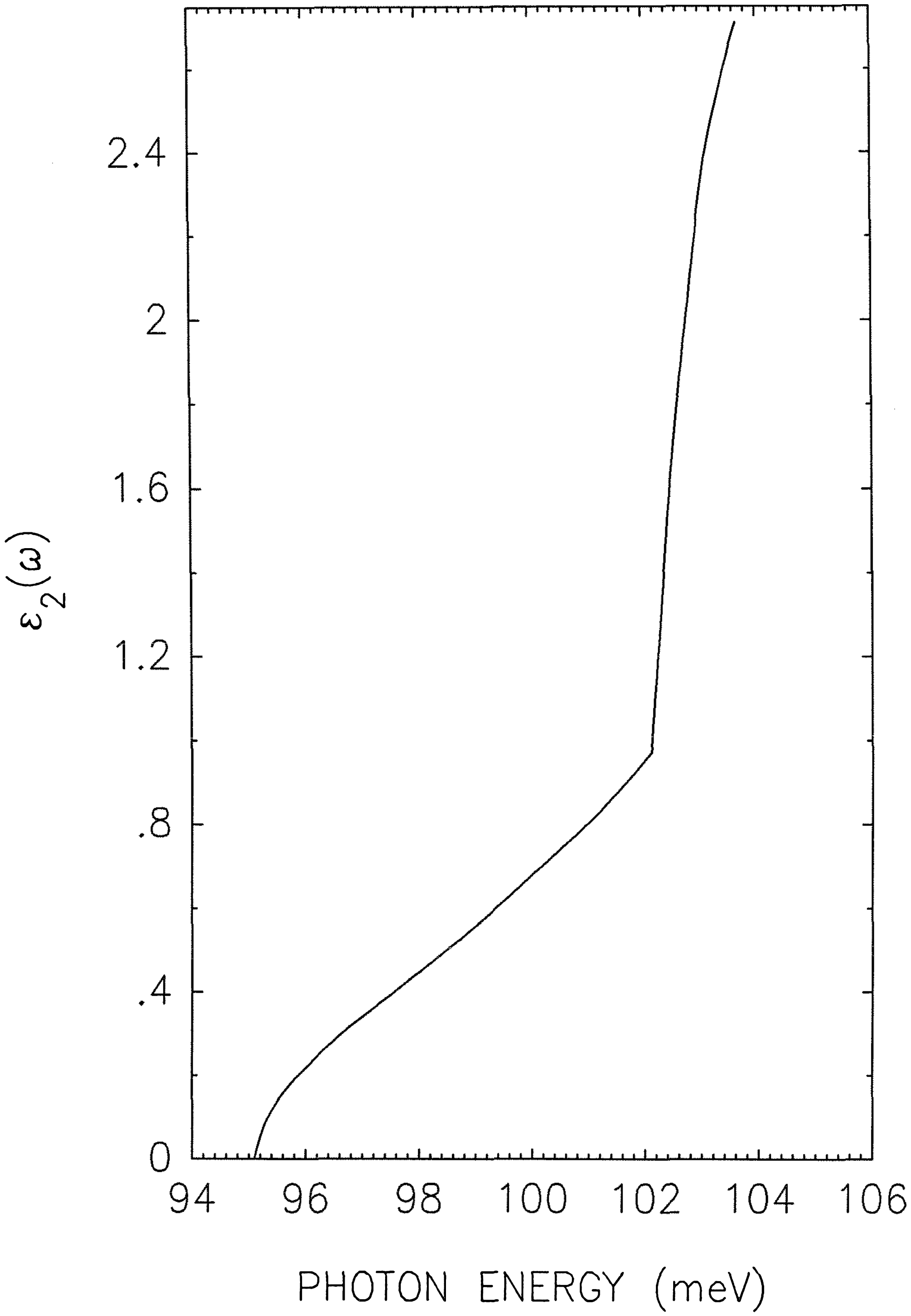

Figure 4.10: Predicted $\epsilon_2^{\|}$ vs. photon energy. The superlattice considered here is made up of an alternating structure consisting of layers of HgTe 70.6 Å thick and layers of CdTe 70.6 Å thick.

4.5 Summary

4.5.1 Optical Properties

We found that the optical matrix element for the alloy is larger but the joint density of states for the superlattice is larger. Since the optical absorption is determined by both the matrix element and the density of states, the superlattice could have absorption comparable to that for the alloy. Furthermore the fact that superlattices of various layer thicknesses may have the same band gap, implies the possibility of adjusting optical properties independent of band gap. With thicker HgTe, the optical matrix element can be increased, while with thicker CdTe, the effective mass and hence the joint density of states are increased. The optical properties of the superlattice can be tuned to be near its optimum. We have presented the comparison of the optical absorption of the superlattice with that of the $Hg_xCd_{1-x}Te$ alloy. Since we do not know $\epsilon_1(\omega)$, a crude approximation is made that n, the real part of the index of refraction, is about the same for the superlattice and for the alloy. This simplifies the comparison of the absorption down to that of $\epsilon_2(\omega)$, the imaginary part of the dielectric function. Our results show that the superlattice, with its larger joint density of states, produces $\epsilon_2^{\|}$ larger than that of the alloy with the same band gap. We therefore conclude that the superlattice might have absorptions comparable to those of the alloy.

4.5.2 Band Offset Effects

We have studied the dependence of the band gap and optical properties on the valence band offset. We found that the band gap and the optical properties of the superlattice are slowly varying functions with positive ΔE_v $(= E_v^{HgTe} - E_v^{CdTe})$ near zero. However, they vary relatively fast as ΔE_v becomes negative. In general, a large variation in the band offset may also lead to a large change in the band gap and optical properties of the HgTe-CdTe superlattice. At a negative offset, the electron and the hole are separated and the radiative recombination rate is decreased. The optical absorptions are expected to decrease.

4.5.3 Strain Effects

We have studied the influence of strain on HgTe-CdTe superlattices grown on CdTe substrates. We found that the strain makes changes in the band energies on the order of 10meV. The changes in the optical properties and band gaps of superlattices with gaps near 100meV are found to be small. However, for superlattices with thicker layers of HgTe or for transport properties, the changes in the band structure could be very important. The light-hole-like subband is pushed up above the heavy-hole subband at zero valence band offset. The majority carrier at low temperature would be light-hole-like while they would be heavy-hole-like in the unstrained superlattice. The conductivity is thus very sensitive to the appearance of strain. However, for most of the superlattices of interest for infrared detector application out to 20μm, strain effects result in small changes in the band gap and imaginary part of the dielectric constant. The band gap changes by a few meV with strain included. $\epsilon_2^{\parallel}$ curve contains a small tail corresponding to optical transitions from the light-hole-like subband to the conduction subband.

References

1. J.N. Schulman and T.C. McGill, Appl. Phys. Lett., **34**, 663 (1979).
2. D.L. Smith, T.C. McGill,and J.N. Schulman, Appl. Phys. Lett., **43**, 180 (1983).
3. J.P. Faurie, A. Million, and J. Piaguet, Appl. Phys. Lett., **41** , 713 (1982), and J. P. Faurie, Proceedings of the 1984 U. S. Workshop on the Physics and Chemistry of Mercury Cadmium Telluride, J. Vac. Sci. Technol. 55 (1985).
4. P. P. Chow and D. Johnson, Proceedings of the 1984 Workshop on the Physics and Chemistry of Mercury Cadmium Telluride, J. Vac. Sci. Technol. 67 (1985).
5. Y. Guldner, G. Bastard, J. P. Vieren, M. Voos, J. P. Faurie and A. Millon, Phys. Rev. Lett. **51**, 907(1983).
6. S. P. Kowalczyk, J. T. Cheung, E. A. Kraut, and R. W. Grant, Phys. Rev. Lett. **56**, 1605 (1986).
7. J. P. Faurie, C. Hsu, and Tran Minh Duc, Proceedings of the 1986 U. S. Workshop on the Physics and Chemistry of Mercury Cadmium Telluride, to be published in J. Vac. Sci. Technol. (1987).
8. L.J. Raubenheimer and G. Gilat, Phys. Rev. Vol. **157**, No. **3**, 586 (1967).

9. G.Y. Wu, C. Mailhiot and T.C. McGill, Appl. Phys. Lett. **46**, 72 (1985).

10. G.Y. Wu and T.C. McGill, Appl. Phys. Lett. Appl. Phys. Lett. **47**, 634 (1985).

11. G.Y. Wu and T.C. McGill, J. Appl. Phys. **58**, 3914 (1985).

12. J.O. McCaldin, T.C. McGill and C.A. Mead, Phys. Rev. Lett. **36**, 56 (1976).

13. J.N. Schulman and T.C. McGill, J. Vac. Sci. Technol., **16**, 1513 (1979).

14. W.A. Harrison, J. Vac. Sci. Technol., **14**, 1016 (1977).

15. J. Tersoff, J. Vac. Sci. Technol. **B**, Vol. 4, No. 4, 1066 (1986).

16. W.A. Harrison, J. Vac. Sci. Technol. **B**, 1068 (1986).

17. Kuech and J.O. McCaldin, J. Appl. Phys. **53** (4), 3121 (1981).

18. J.W. Matthews and A.E. Blakeslee, J. Cryst. Growth **27**, 118 (1974) ; **29**, 273(1975); **32**, 265 (1976).

19. G. C. Osbourn, Phys. Rev. **B 27**, 5126 (1983).

Chapter 5

Theoretical Study of Semimagnetic Superlattices in a Magnetic Field

5.1 Introduction

5.1.1 Semimagnetic Semiconductors

Novel Materials

The new group of semiconducting materials, semimagnetic semiconductors (SMSCs) or diluted magnetic semiconductors, has been extensively studied. SMSCs are in fact solid solutions of $A_{1-x}M_xB$ type which are formed by the substitution of the A component in an ordinary semiconductor AB by $3d$ or $4f$ M component. If the MB compound is a magnetic semiconductor, then $A_{1-x}M_xB$ solid solutions are continuously filling *the gap* between normal nonmagnetic and magnetic semiconductors. In this case $A_{1-x}M_xB$ is the missing link between AB and MB and the terminology *semimagnetic semiconductors* adequately reflects the situation.

In a zero external magnetic field (B = 0), typical SMSCs such as $Cd_{1-x}Mn_xTe$ or $Hg_{1-x}Mn_xTe$ behave like their normal nonmagnetic counterparts. They have conduction and valence band structures which depend on Cd or Hg substitution by Mn. Changing the composition x, we can modify band structures, e.g. effective masses of electrons and holes, the forbidden energy gap E_g, etc.

The qualitative difference between $Hg_{1-x}Mn_xTe$ and $Hg_{1-x}Cd_xTe$, for example, is revealed when an external magnetic field is applied ($B \neq 0$). In this case the presence of magnetic ions, through the exchange interaction J between localized magnetic moments (LMMs) and mobile band electrons, essentially affects free charge carrier behaviour. In zero-order approximation the modified band electron behaviour can be described through the introduction of the spin average $\langle S_z \rangle$ proportional to the bulk magnetization.

In magnetic semiconductors, the strongly interacting system of magnetic ions is in a magnetic state and does not respond to the external magnetic field. In contrast, magnetic ions in SMSCs respond to an applied magnetic field while their concentration in SMSCs is comparable to that in magnetic semiconductors. In this situation the M component characterized by spin polarization $\langle S_z \rangle$ plays, in an SMSC crystal, the role of an external magnetic field amplifier. This makes it possible to observe in SMSCs extremely large magneto-optical effects.

Effects of Temperature and Magnetic Field

The dependence of average spin on temperature and magnetic field makes it possible to observe in a SMSC effects due to temperature or magnetic field variation. Both temperature decrease and magnetic field increase result in an enhancement of the spin polarization $\langle S_z \rangle$.

Changing the magnetic component content x over a wide range, it is possible to observe compounds with the same crystal structure in paramagnetic and spin-glass states in succession. In general, at low temperature and high composition (x is a few tens of percent, say), spin-glass phase is formed. The origin of the spin-glass transition is the so-called lattice frustration mechanism. The topology of the fcc lattice cannot accommodate all nearest neighbors to order antiferromagnetically, and this frustration leads to a frozen but disordered state, i.e., a spin glass. In the chapter we confine our discussion to the paramagnetic state only.

The antiferromagnetic coupling among magnetic ions is also present in the paramagnetic state. But when the composition x is so small (a few thousandths, say), the magnetic ions can be assumed to be isolated. They do not interact with the surrounding magnetic ions. In the dilute region, the magnetization of the system is simply described by

$$M = -N_s g_{Mn} \mu_B \langle S_z \rangle,$$

where N_s is the number of magnetic ions per unit volume, μ_B is the Bohr magneton, and $\langle S_z \rangle$ is the thermal average of the total spin operator $\hat{S}$ of the Mn^{++} ions, given by

$$\langle S_z \rangle = -S B_s \left(\frac{g_{Mn} \mu_B S B}{kT} \right). \tag{5.1}$$

Here S = 5/2 is the total Mn^{++} spin, k is the Boltzmann constant, T is the temperature, and $B_s(Z)$ is the Brillouin function

$$B_s(Z) \equiv \frac{2S+1}{2S} \coth \left(\frac{2S+1}{2S} Z \right) - \frac{1}{2S} \coth \left(\frac{Z}{2S} \right). \tag{5.2}$$

In the paramagnetic region with interactions among magnetic ions, the magnetization is empirically described by a Brillouin function

$$\langle S_z \rangle = -S_0 B_{5/2} \left(\frac{5}{2} \frac{g \mu_B B}{k(T+T_0)} \right), \tag{5.3}$$

where S_0 is the effective magnetic moment per spin and T_0 is the effective temperature. They have been tabulated as functions of x and T^{15}.

Electron in a Magnetic Field

When an external magnetic field $\vec{B}$ is applied in z-direction, the Hamiltonian is modified. The theory detailing the motion of an electron in a magnetic field has been described in Chapter 3. The momentum operator $\vec{p}$ is to be replaced with

$$\vec{p} \rightarrow \vec{p} + \frac{e\vec{A}}{c},$$

where $\vec{A}$ is the vector potential of the magnetic field:

$$\vec{A} = (-By, 0, 0), \tag{5.4}$$

in Landau gauge. The presence of magnetic field affects the orbital motion of an electron. The crystal Hamiltonian no longer has translational symmetry in y-direction. But the translational symmetry is preserved both in x-direction and in z-direction. In addition, there is the spin-field interaction term in the Hamiltonian:

$$\frac{e\hbar}{2mc}\vec{\sigma} \cdot \vec{B}. \tag{5.5}$$

This term induces spin-splitting of energy levels. The exchange interaction H_ϵ does not change the symmetry of the Hamiltonian within *virtual crystal approximation* and *mean field approximation.* The energy levels are labeled by k_x, k_z, and N. Here, k_x is the wave vector associated with the translational symmetry in x-direction. N is the Landau level index describing the quantization of orbital motion. k_z is the wave vector associated with the translational symmetry in z-direction.

With no magnetic field, the crystal has a band structure typical of a zinc-blende structure. Each band is doubly degenerate. The heavy-hole and the light-hole bands are degenerate at the zone center. With a magnetic field, the two-fold degeneracy is lifted. Within effective-mass approximation, the energy levels of the conduction band of a nonmagnetic semiconductor can be approximated by

$$\begin{aligned} E_n^{\uparrow} &= E_c + (N + \frac{1}{2})\hbar\omega_c + \frac{1}{2}g_c\mu_B B, \\ E_n^{\downarrow} &= E_c + (N + \frac{1}{2})\hbar\omega_c - \frac{1}{2}g_c\mu_B B, \end{aligned} \tag{5.6}$$

where $\omega_c = eB/m_c c$, the cyclotron frequency, E_c is the band edge, and g_c is the g-factor. The second term in Eq. (5.6) induces Landau level shift, which pushes the energy level upwards. The third term induces spin-splitting, which lowers the energy of states with $\uparrow$ spin when g_c is negative, as is in CdTe. In a semimagnetic semiconductor, spin-splitting is enhanced by the exchange interaction. In Chapter 3, we saw that in the Hamiltonian matrix $(\Pi_a)_{11}$ contains a term $XN_m\alpha\langle S_z\rangle/2$ and $(\Pi_b)_{11}$ contains $-XN_m\alpha\langle S_z\rangle/2$ due to the presence of the magnetic ions. In consequence, the energy levels of the conduction band of a semimagnetic semiconductor are approximately described by

$$\begin{aligned} E_n^{\uparrow} &= (N + \frac{1}{2})\hbar\omega_c + \frac{1}{2}g_c\mu_B B - \frac{1}{2}XN_m\alpha\langle S_z\rangle, \\ E_n^{\downarrow} &= (N + \frac{1}{2})\hbar\omega_c - \frac{1}{2}g_c\mu_B B + \frac{1}{2}XN_m\alpha\langle S_z\rangle. \end{aligned} \tag{5.7}$$

In CdMnTe, the second term and the exchange term in Eq. (5.7) have opposite signs. Depending on the magnitude of average spin, the exchange term could be larger than the second term in magnitude. This might effectively reverse the sign of g-factor. As to the valence bands, due to the degeneracy of valence bands at the zone center, the quantized energy levels of the valence bands are more complicated. But generally speaking, each band form Landau levels which are spin-split. The spin-splitting is also enhanced by the exchange interaction.

On the whole, the band gap of the material is narrowed by spin-splitting of the levels, while the orbital motion quantization tends to enlarge the band gap. The two effects compete with each other. Generally, the enhanced spin-splitting in a semimagnetic material dominates over the Landau level shift. However, in a narrow-gap material, the small effective mass results in large Landau level shift which could appreciably decrease the narrowing of the band gap.

The two effects have different temperature dependence. The Landau level shift does not depend on the temperature at all. However, the spin-splitting has a strong temperature dependence. An increase in temperature tends to randomize the orientation of localized magnetic moments. Therefore, as temperature increases, spin-splitting becomes reduced. Landau level shift is going to win out at some point. Since Landau level shift increases the energy of an electronic level, the band gap begins to widen at a sufficiently high temperature.

The two effects also have different magnetic field dependence. As the intensity of magnetic field increases, magnetic spins are aligned and saturated at some point. Beyond that point the spin-splitting is nearly constant until the point is reached at which the $\vec{\sigma} \cdot \vec{B}$ term in the Hamiltonian is comparable to the exchange interaction H_ϵ. Beyond that point, the spin-splitting, dominated by the $\vec{\sigma} \cdot \vec{B}$ term, again increases with the intensity of field. As to the Landau level shift, it keeps increasing with the intensity of field. When the magnetic field is so large that magnetic breakdown occurs and the cyclotron radius is comparable to the lattice constant, the energy band picture is no longer valid. In such case Eq.(5.6) does not hold which is based upon the use of effective-mass approximation. However, we restrict our attention to the case where effective-mass approximation is valid.

5.1.2 Semimagnetic Superlattices

Because the introduction of a superlattice provides more degrees of freedom in devising a material with prescribed properties, it is natural to extend the study of SMSCs to the field of semimagnetic semiconductor superlattices (SMSCSLs). This way we are able to adjust a number of properties of materials such as optical properties and band gap by the application of a magnetic field and/or by changing layer thicknesses.

The growth of high-quality $Cd_{1-x}Mn_xTe/Cd_{1-y}Mn_yTe$ superlattices and $Hg_{1-x}Mn_xTe$ epilayers has recently been demonstrated using molecular beam epitaxy techniques[1,2,3,4,5]. Growth has been achieved with both a [111] and [100] growth axis[6]. These materials are particularly interesting because of the presence of the magnetic Mn^{++} ion. The $Cd_{1-x}Mn_xTe/Cd_{1-y}Mn_yTe$ superlattice has been proposed as magnetically tunable laser materials. The $Hg_{1-x}Mn_xTe/Cd_{1-y}Mn_yTe$ superlattice has the potential for being magnetically tunable IR materials. The strong exchange interaction between the localized $3d$ electrons of the Mn^{++} ions and itinerant band electrons gives rise to large Zeeman splittings of the energy bands. Magneto-optic studies of these superlattice systems have recently been performed[7,8,9]. Magnetic field dependence of the luminescence has been seen. Laser emission has been observed from these superlattices[10]. The energy of the stimulated emission peak has been shifted by application of a magnetic field.

To study the superlattice, we use the theoretical method which has been discussed in detail in Chapter 3. We employ the superlattice k.p theory of band structures of semimagnetic semiconductor superlattices. Each eigenstate is labeled by three quantum numbers: k_x, N, and Q. Here, k_x is the in-plane wave vector associated with the translational symmetry in x-direction. N is the Landau level index. Q is the superlattice wave vector associated with the superlattice translational symmetry in the growth direction.

In the case of a superlattice, the magnetic field affects the energy levels in the same way as in the case of a bulk crystal. The Landau level shift tends to increase the band gap while the spin-splitting tends to reduce the band gap.

In the following, we present our first theoretical study of the electronic properties of superlattices formed from semimagnetic semiconductors. In Section (5.2), we present the results for $Cd_{1-x}Mn_xTe$ superlattices formed by layering materials with different values of x. The $Cd_{0.8}Mn_{0.2}Te/Cd_{0.7}Mn_{0.3}Te$ system is explicitly considered. In Section 5.3, we present the results for $Hg_{1-x}Mn_xTe/Cd_{1-y}Mn_yTe$ superlattices. The $Hg_{0.95}Mn_{0.05}Te/Cd_{0.78}Mn_{0.22}Te$ system is considered explicitly. In Section 5.4, we summarize our study of the two semimagnetic superlattices.

5.2 $Cd_{1-x}Mn_xTe/Cd_{1-y}Mn_yTe$ Superlattices

In this section, we present our study of $Cd_{1-x}Mn_xTe/Cd_{1-y}Mn_yTe$ superlattices. Specifically $Cd_{0.8}Mn_{0.2}Te/Cd_{0.7}Mn_{0.3}Te$ superlattices were chosen. The strain effects due to the lattice constant difference of the two constituent materials ($\sim 2\%$) are neglected in order to illustrate only the effects of magnetic field and temperature on the band structure of the superlattice. The band gap of $Cd_{0.8}Mn_{0.2}Te$ is 1.88eV and that of $Cd_{0.7}Mn_{0.3}Te$ is 2.04eV. The valence band offset is taken to be zero in accordance with observed strong luminescence from the superlattice. The reasons are in the following. Strong luminescence is attributed to the increased radiative recombination rate, which indicates that electrons and holes are both confined in $Cd_{0.8}Mn_{0.2}Te$ layers. Hence ΔE_v is at most equal to ΔE_g, which is equal to 0.16eV. In addition, the common anion rule also predicts a small valence band offset. Therefore, although there has not been any direct measurement of the band offset, we assume the valence band offset is zero in the calculation. The superlattice is taken to be (001) grown.

In Figure (5.1), we show the lowest conduction band and highest valence band energy levels at $Q_z = 0$ for a $Cd_{0.8}Mn_{0.2}Te/Cd_{0.7}Mn_{0.3}Te$ superlattice consisting of six molecular layers of each constituent material for three cases: no magnetic field, a magnetic field of 5T neglecting exchange interaction (at high spin temperature) and a magnetic field of 5T including the exchange interaction (at zero spin temperature[19]). At B = 0, the conduction band states are 2-fold degenerate and the valence band states are 4-fold degenerate. (Because the valence band offset is taken to be zero and lattice mismatch is neglected, there is no splitting of the heavy- and light-hole bands.) For the B = 5T and high spin temperature case, all degeneracies are broken, the conduction band states move to higher energy and the valence band states move to lower energy. However, the size of the splittings and the motion of the levels are quite small. (The splittings of the two conduction band states and the highest two valence band states are so small that they are not resolved in Figure(5.1).) For the B = 5T and zero temperature case, much larger splittings, due to the exchange interaction, occur and the bandgap of the superlattice is decreased by the magnetic field. The states are labeled according to the primary characters of the corresponding wave functions. All states shown are made up primarily of n = 0 harmonic oscillator eigenfunctions. The states labeled *Su* has primarily |S 1/2> atomic character, *Sd* has primarily |S −1/2 > character, *HHd* has primarily |3/2 − 3/2 > character, *LHd* has primarily |3/2 − 1/2 > character, *LHu* has primarily |3/2 1/2 > character and *HHu* has primarily |3/2 3/2 > character. The unlabeled lines indicate the energy levels of states made up primarily from n = 1 harmonic oscillator functions. The positions of states made primarily from higher harmonic oscillator functions are not shown. It is clear from Figure (5.1) that the magnetic field splittings in the superlattice are dominated by the exchange interaction. The relative change in the bandgap is $\approx$ 2.5%.

In Figure (5.2), the derivative of the bandgap with magnetic field of the $Cd_{0.8}Mn_{0.2}Te/Cd_{0.7}Mn_{0.3}Te$ superlattice at small magnetic field and zero temperature[19] is shown as a function of the number of molecular layers of the X = 0.2 alloy for three ratios of the superlattice layer thicknesses. Also shown, for comparison,

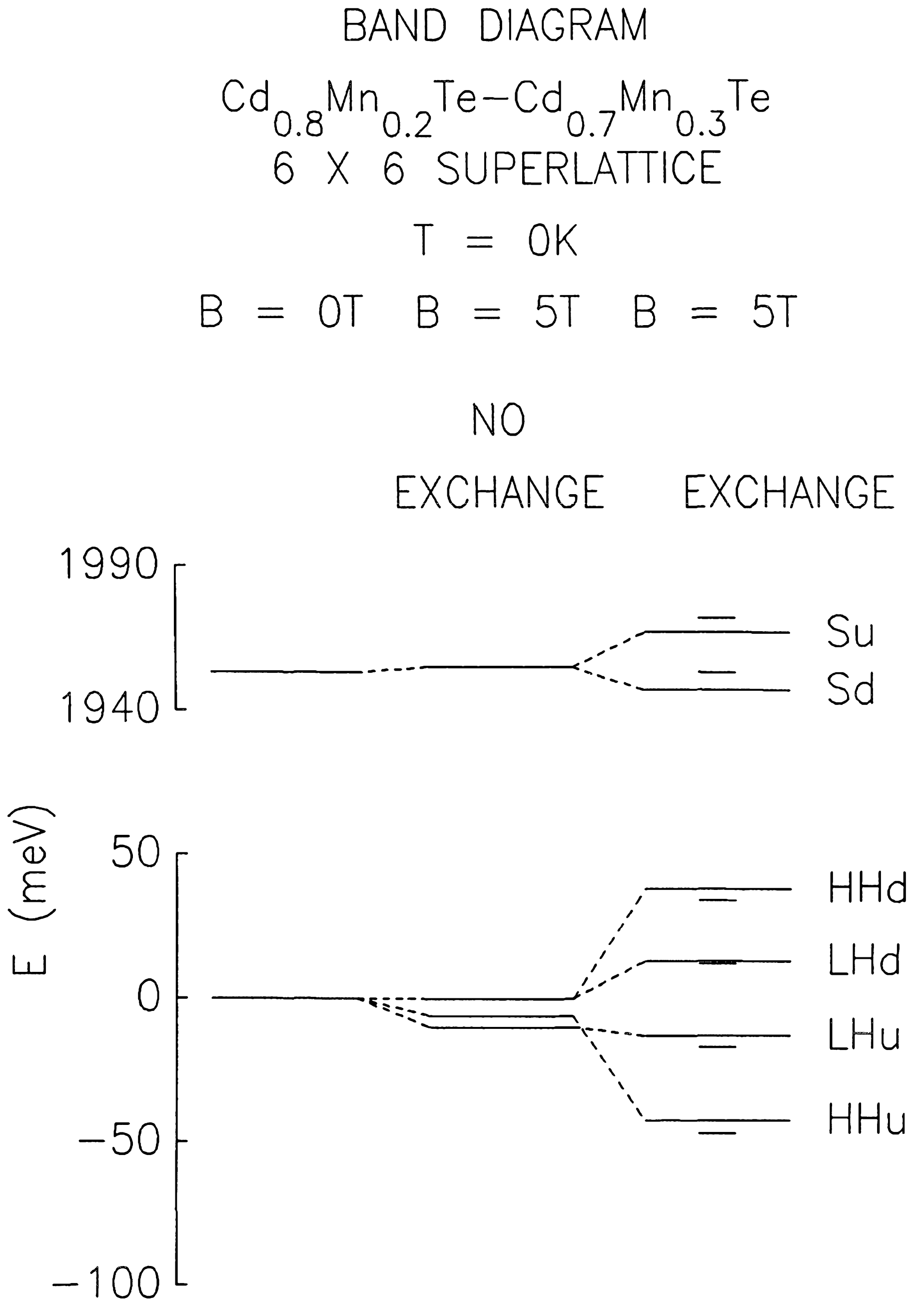

Figure 5.1: Energy levels of the lowest conduction band and highest valence band states at $Q_z = 0$ for a $Cd_{0.8}Mn_{0.2}Te/Cd_{0.7}Mn_{0.3}Te$ superlattice consisting of six molecular layers of each constituent material for three cases: no magnetic field, a magnetic field of 5T neglecting exchange interaction and a magnetic field of 5T including the exchange interaction.

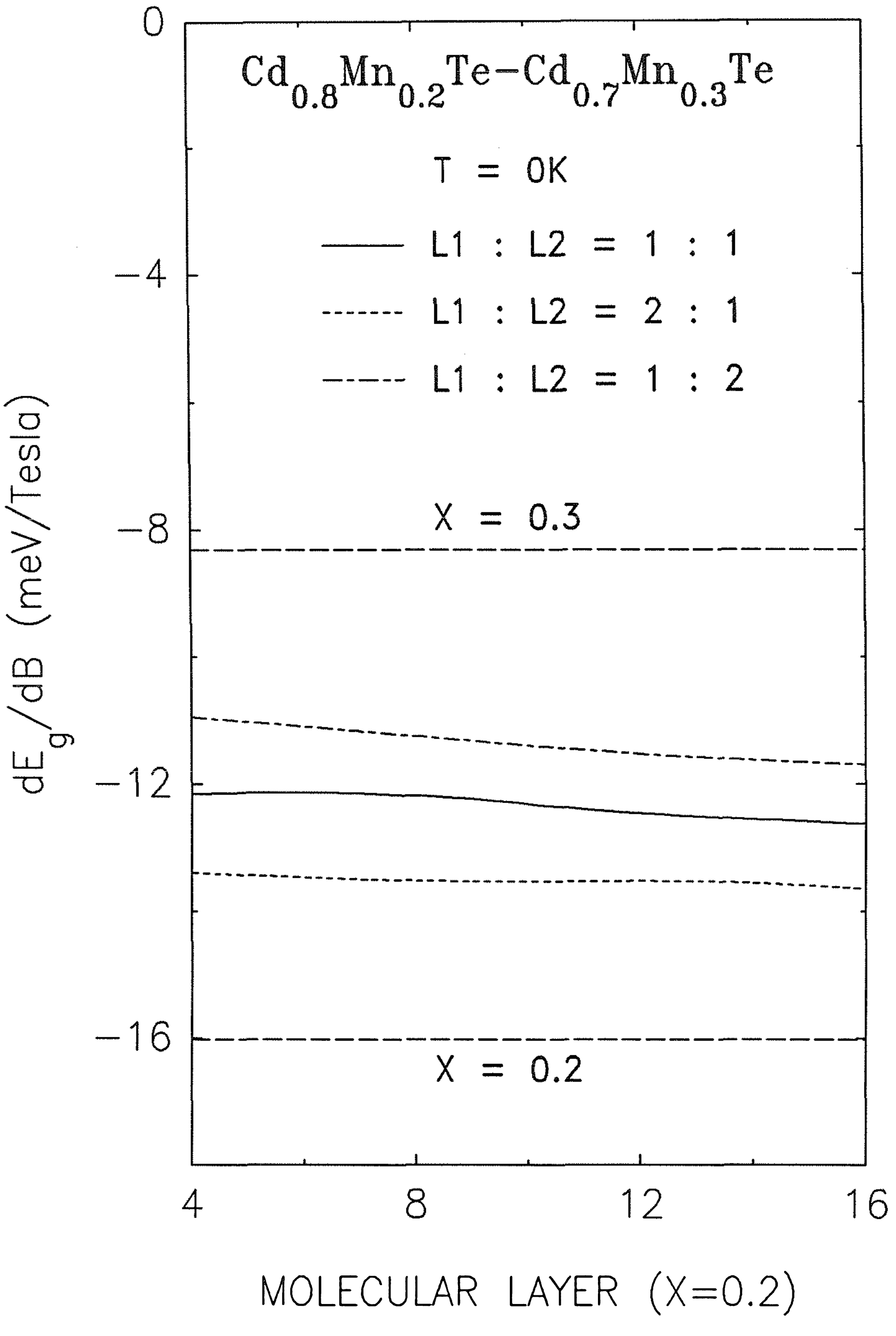

Figure 5.2: The derivative of the $Cd_{0.8}Mn_{0.2}Te/Cd_{0.7}Mn_{0.3}Te$ superlattice bandgap with magnetic field as a function of the X = 0.2 alloy layer thickness for three layer thickness ratios. The corresponding derivatives for the X = 0.2 and X = 0.3 alloys are shown as straight lines.

are the corresponding derivatives for the two constituent alloys. First, notice that the derivative of the $X = 0.3$ alloy is less than that of the $X = 0.2$ alloy. This occurs, according to the results of Ref. (14), because of stronger antiferromagnetic coupling in the $X = 0.3$ alloy. That is, the net Mn^{++} spin (absolute value of the composition times the average spin $X<S_z>$) is larger in the $X = 0.2$ alloy than in the $X = 0.3$ alloy at zero temperature and small magnetic fields. The derivatives in the superlattice lie between those of the alloys. For the thin layer superlattices, the results are simply averaged. That is, the 1:1 superlattice result is half way between the $X = 0.2$ and $X = 0.3$ alloys; the 2:1 superlattice is 1/3 and the 1:2 superlattice is 2/3 of the way between the $X = 0.2$ and $X = 0.3$ alloys. For thin superlattices, the electron and hole wavefunctions are not well confined by energy barriers. Indeed, the only barrier for holes is due to the exchange interaction itself, like the "spin superlattices" of Ref. (21). As the superlattice layer thicknesses increase, the magnitude of the derivative increases, moving toward the value of the $X = 0.2$ alloy. This occurs because the carrier wavefunctions are better confined in the $X = 0.2$ alloy in the thicker superlattices. The effect is not very large, however, because the barrier for holes is small and the exchange interaction is larger for holes than for the electrons. However, if the valence band offset is positive (i.e., the valence band edge of $Cd_{0.8}Mn_{0.2}Te$ is higher than that of $Cd_{0.7}Mn_{0.3}Te$) and not nearly zero, then the holes will be rather confined to $Cd_{0.8}Mn_{0.2}Te$ layers. The superlattice curves will not be so flat and they will approach to the $X = 0.2$ curve more rapidly with the increase in layer thickness. On the other hand, if the valence band offset should be negative (i.e., the valence band edge of $Cd_{0.8}Mn_{0.2}Te$ is lower than that of $Cd_{0.7}Mn_{0.3}Te$) and not nearly zero, then holes would be confined to $Cd_{0.7}Mn_{0.3}Te$ layers. The superlattices results would approach to the $X = 0.3$ curve, instead, with the increase in layer thickness.

In Figure (5.3), we show the change in bandgap with magnetic field at three magnetic fields for a $Cd_{0.8}Mn_{0.2}Te/Cd_{0.7}Mn_{0.3}Te$ superlattice consisting of eight molecular layers of each alloy as a function of inverse temperature[19]. The arrows indicate the zero temperature asymptotes. The bandgap reduction is due to the exchange interaction of the band electrons with localized 3d electrons on Mn^{++}. At low temperatures the Mn^{++} spins align in the direction opposite to the magnetic field, leading to a net interaction with the band electrons. At higher temperatures, the Mn^{++} spins are randomized and there is no net exchange interaction with band electrons (within mean field theory). From the figure, one sees that the strength of the net exchange interactions decreases rapidly with increasing temperature for temperatures above 5K. In fact, the band gap is expected to increase at sufficiently high temperature because the change in the band gap will be dominated by the Landau level shift alone, which enlarges the band gap. Also notice that, the three cases have different aymptotic values at low temperature limit. Even at zero temperature, the antiferromagnetic coupling still prevents local magnetic moments from all being aligned in the same direction. The degree of alignment depends upon the intensity of applied magnetic field. The larger the magnetic field, the more the number of aligned spins. This explains why the asymptotic values are different. With a sufficiently large magnetic field, the antiferromagnetic coupling among magnetic ions would be broken and all the moments would be aligned in the same direction. The graph shows that the degree of alignment at zero temperature does not increase in proportion to the strength of magnetic field. The degree of alignment of magnetic ions, with the magnetic field increasing from 10T to 15T, is not improved as much as with the field increasing from 5T to 10T. It implies that the use of a magnetic field around 10T may be most economic while a full band gap reduction is nearly achieved at low temperature.

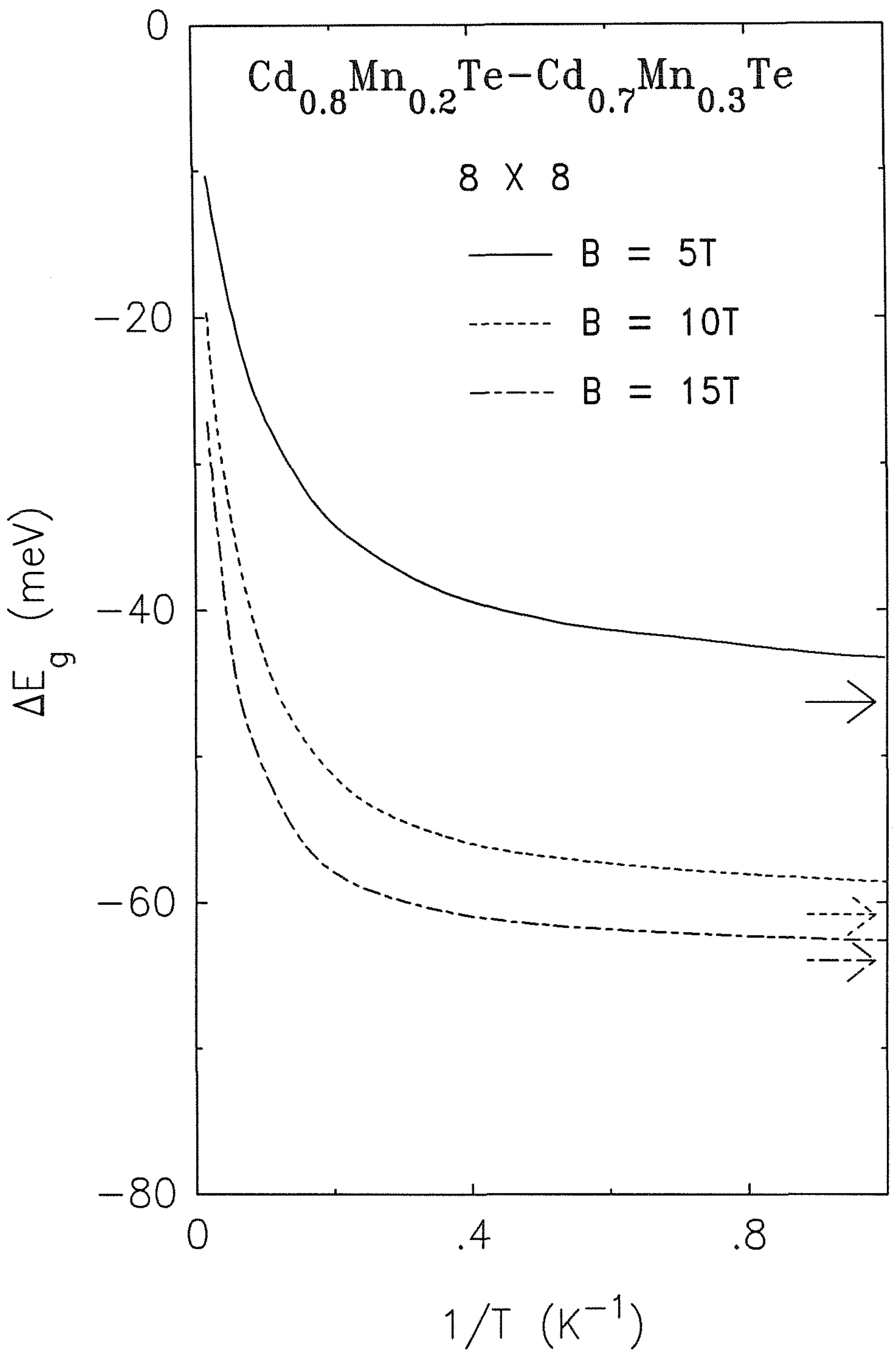

Figure 5.3: Change in bandgap of the 8 x 8 $Cd_{0.8}Mn_{0.2}Te/Cd_{0.7}Mn_{0.3}Te$ superlattice as a function of inverse temperature and three magnetic fields. Arrows indicate the zero temperature asymptotes.

5.3 $Hg_{1-x}Mn_xTe/Cd_{1-y}Mn_yTe$ Superlattices

In this section, we are going to present results of our study of another interesting system: $Hg_{0.95}Mn_{0.05}Te/Cd_{0.78}Mn_{0.22}Te$ superlattices. The specific concentation of Mn^{++} was chosen such that the two consitituent materials are lattice-matched. The $Hg_{0.95}Mn_{0.05}Te$ has a band structure similar to that of HgTe. The conduction band and the valence band both belong to Γ_8-symmetry. The p-s gap is $-0.1eV$. The $Cd_{0.78}Mn_{0.22}Te$ has a band structure similar to that of CdTe. The p-s gap is $1.9eV$. Therefore, the $Hg_{0.95}Mn_{0.05}Te/Cd_{0.78}Mn_{0.22}Te$ superlattice is expected to have a band gap varying from 0 to 1.9eV. This feature makes it very attractive in the consideration of magnetically tunable infrared material.

In Figure (5.4), we show the energy levels at $Q_z = 0$ for a $Hg_{0.95}Mn_{0.05}Te/Cd_{0.78}Mn_{0.22}Te$ superlattice consisting of fifteen molecular layers of each constituent material[19]. The valence band offset is taken to be zero tentatively. The dependence of magnetic effects on the value of valence band offset is shown in later figures. At B = 0, the conduction band states are 2-fold degenerate and the valence band states are 4-fold degenerate due to choices of zero valence band offset and zero strain. For the B = 5T and high spin temperature case, all degeneracies are broken, the conduction band states move to higher energy and the valence band states move to lower energy. For the B = 5T and zero spin temperature case, much larger splittings, due to the exchange interaction, occur and the bandgap of the superlattice is decreased by the magnetic field. The states are labeled according to the primary wave function characters they carry. We note that the conduction band states with a strong $|3/2 \quad 1/2>$ ($|3/2 -1/2>$) character also carry a $|S \ 1/2>$ ($|S \ -1/2>$) character of comparable magnitude. However, the exchange integrals for light-hole and S characters have opposite signs with the exchange integral for the light-hole states being larger in magnitude than that for the S states[15]. Since order of the splitting is determined by the light-

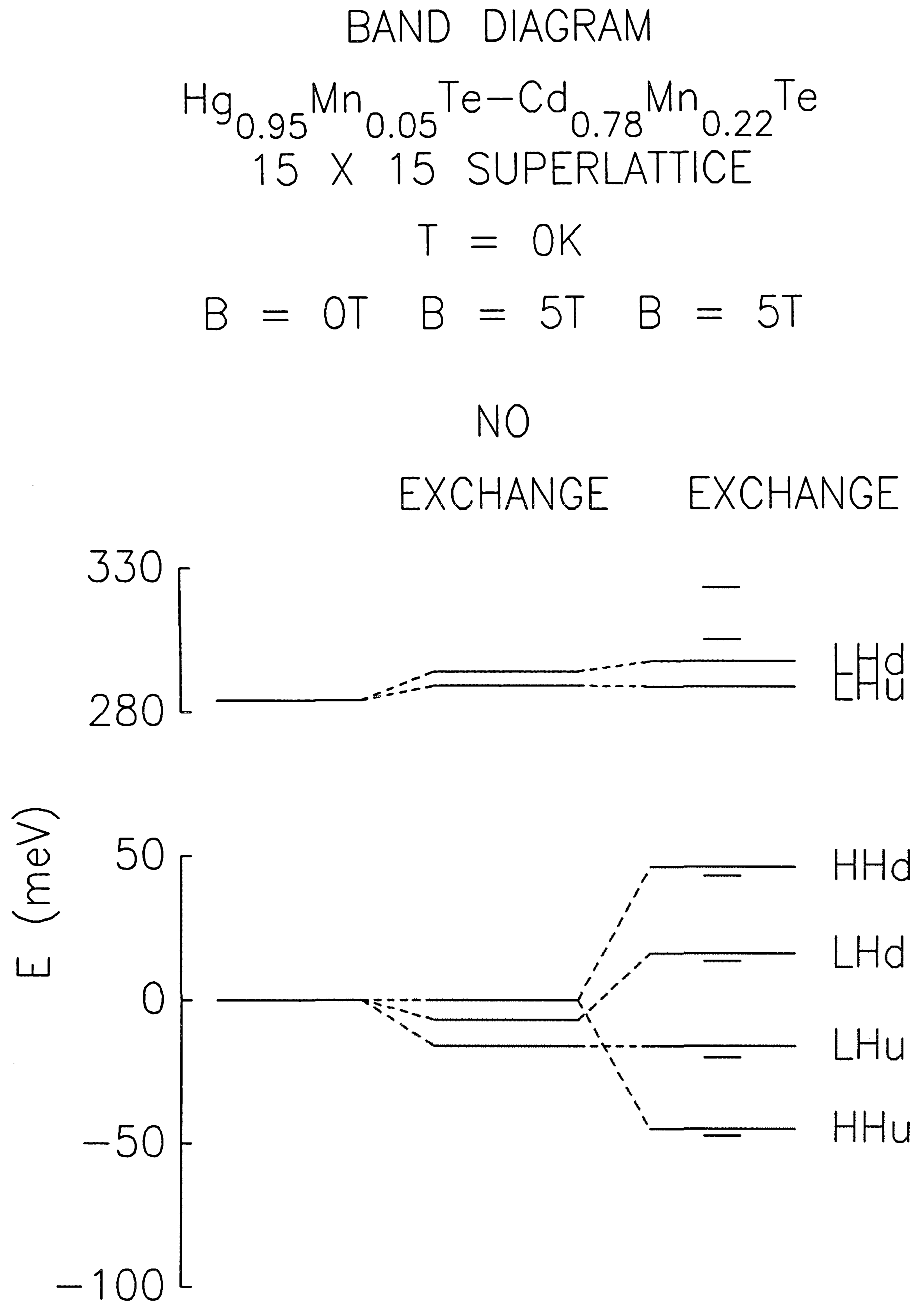

Figure 5.4: Energy levels of the lowest conduction band and highest valence band states at $Q_z = 0$ for a $Hg_{0.95}Mn_{0.05}Te/Cd_{0.78}Mn_{0.22}Te$ superlattice consisting of fifteen molecular layers of each constituent material for three cases: no magnetic field, a magnetic field of 5T neglecting exchange interaction and a magnetic field of 5T including the exchange interaction.

hole character, we label the conduction band states showing only their light-hole character. We find that the Landau level shift of the conduction band states is larger than that in $Cd_{0.8}Mn_{0.2}Te/Cd_{0.7}Mn_{0.3}Te$ since the lighter electron effective mass here gives rise to a larger cyclotron frequency which, in turn, induces a larger Landau level shift. The splittings of valence band states are similar to those in $Cd_{0.8}Mn_{0.2}Te/Cd_{0.7}Mn_{0.3}Te$. However, because the bandgap here is smaller, the relative change in the bandgap is larger and is $\approx 10\%$.

The above analysis of wave function characters of each state is very important for evaluation of the superlattices as IR detectors. The optical absorption is determined by the electronic transition rate induced by the harmonic field of the light. Hence, $\langle c|p|v\rangle$, which is the optical transition matrix element, determines the strength of the absorption. The only nonzero elements are those whose *bra* and *ket* states have same spin (since the momentum operator is spin-diagonal) and opposite symmetries (since the momentum operator has odd symmetry). For the system considered here, the matrix element for the lowest transition is primarily determined by $\langle LHu|p|HHd\rangle$ and $\langle Su|p|HHd\rangle$, both of which are very small compared to that for the transition from the top valence band level to the second conduction band level. The latter depends on the matrix elements $\langle LHd|p|HHd\rangle$ and $\langle Sd|p|HHd\rangle$. While $\langle LHd|p|HHd\rangle$ is nearly zero, $\langle Sd|p|HHd\rangle$ is finite. In light of this, the optical gap is the energy difference between the top valence band state and the second conduction band state while the thermal gap is the difference between the top valence band state and the bottom conduction band state. This need to be taken into account in the consideration of noise problem.

In Figure (5.5), we show the change in bandgap with magnetic field at three magnetic fields for a $Hg_{0.95}Mn_{0.05}Te/Cd_{0.78}Mn_{0.22}Te$ superlattice consisting of fifteen molecular layers of each alloy as a function of inverse temperature[19]. The arrows indicate the zero temperature asymptotes. At low temperatures the Mn^{++}

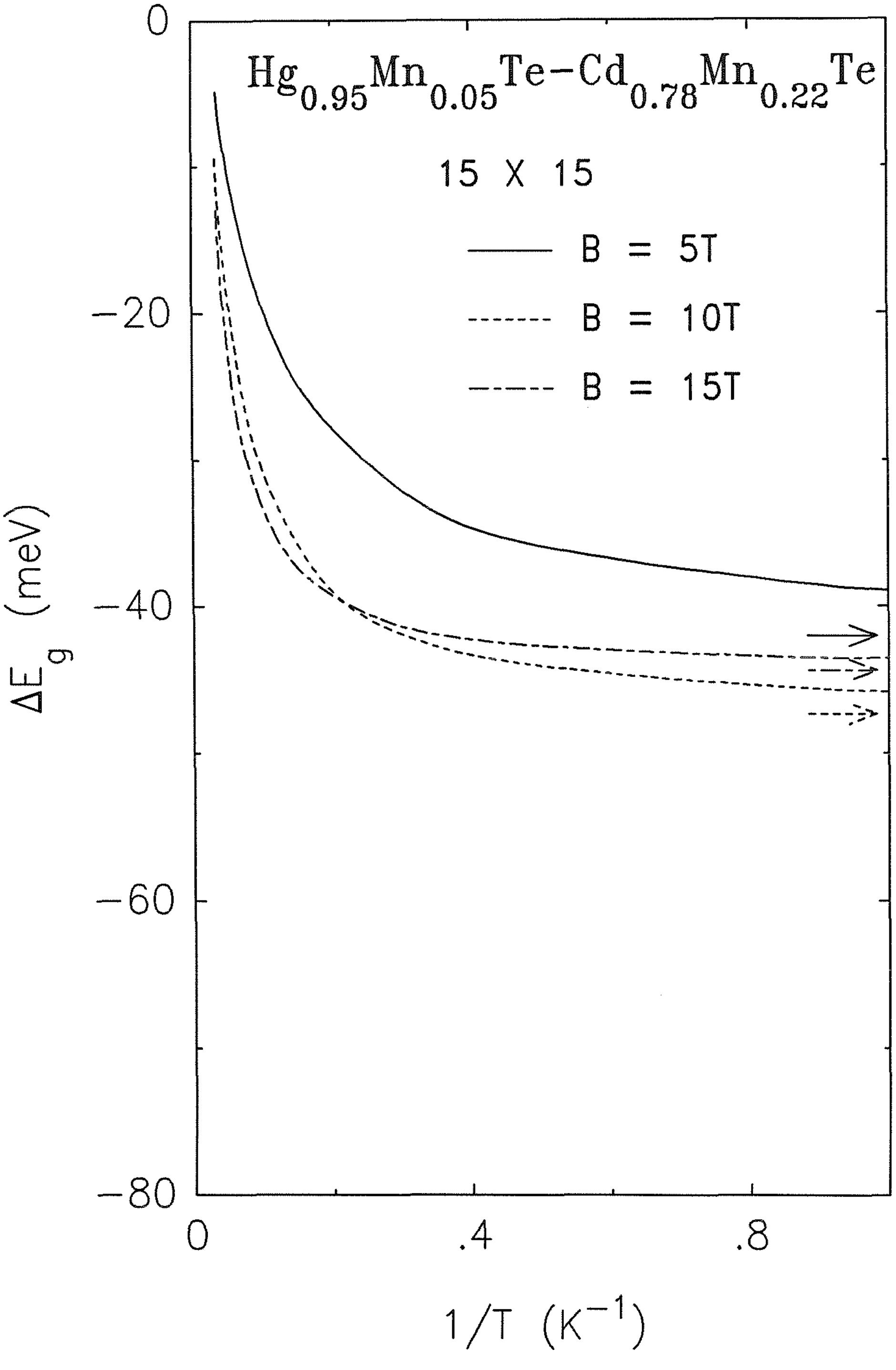

Figure 5.5: Change in bandgap of the 15 x 15 $Hg_{0.95}Mn_{0.05}Te/Cd_{0.78}Mn_{0.22}Te$ superlattice as a function of inverse temperature and three magnetic fields. Arrows indicate the zero temperature asymptotes.

spins align in the direction opposite to the magnetic field, leading to a net interaction with the band electrons. At higher temperatures, the Mn^{++} spins are randomized and there is no net exchange interaction with band electrons (within mean field theory). From the figure, one sees that the strength of the net exchange interactions decreases rapidly with increasing temperature for temperatures above 5K. Notice the intersection at about 5K of the two curves for B = 10T and B = 15T. Below 5K, because of Mn^{++} spin saturation, the reduction in the bandgap resulting from the enhanced spin splitting is about the same at both magnetic fields. However, at B = 15T the Landau level shift is larger and results in a bit smaller net decrease in the bandgap. Above 5K, the spins are not saturated and the larger magnetic field of 15T gives rise to a larger net spin of Mn^{++} and hence, a larger spin splitting. As a result, the two curves cross each other.

In Figure (5.6), we show the change in bandgap as a function of valence band offset at three magnetic fields at zero temperature[19] for a $Hg_{0.95}Mn_{0.05}Te/Cd_{0.78}Mn_{0.22}Te$ superlattice consisting of fifteen molecular layers of each alloy. The bandgaps are about maximum around zero valence band offset. As the valence band offset decreases from zero, both the valence and conduction band edges move toward each other. This results in a rapid drop in the bandgap. As the valence band offset increases from zero, both band edges move in the same direction but the valence band edge does faster. This results in a slow decrease in the bandgap. The results for B = 5T and B = 10T are close to each other due to the fact that the spin splittings are about the same at both fields at zero temperature.

In Figure (5.7), we show the bandgap as a function of magnetic field at zero temperature[19] for a $Hg_{0.95}Mn_{0.05}Te/Cd_{0.78}Mn_{0.22}Te$ superlattice consisting of fifteen molecular layers of each alloy for three values of valence band offset. The

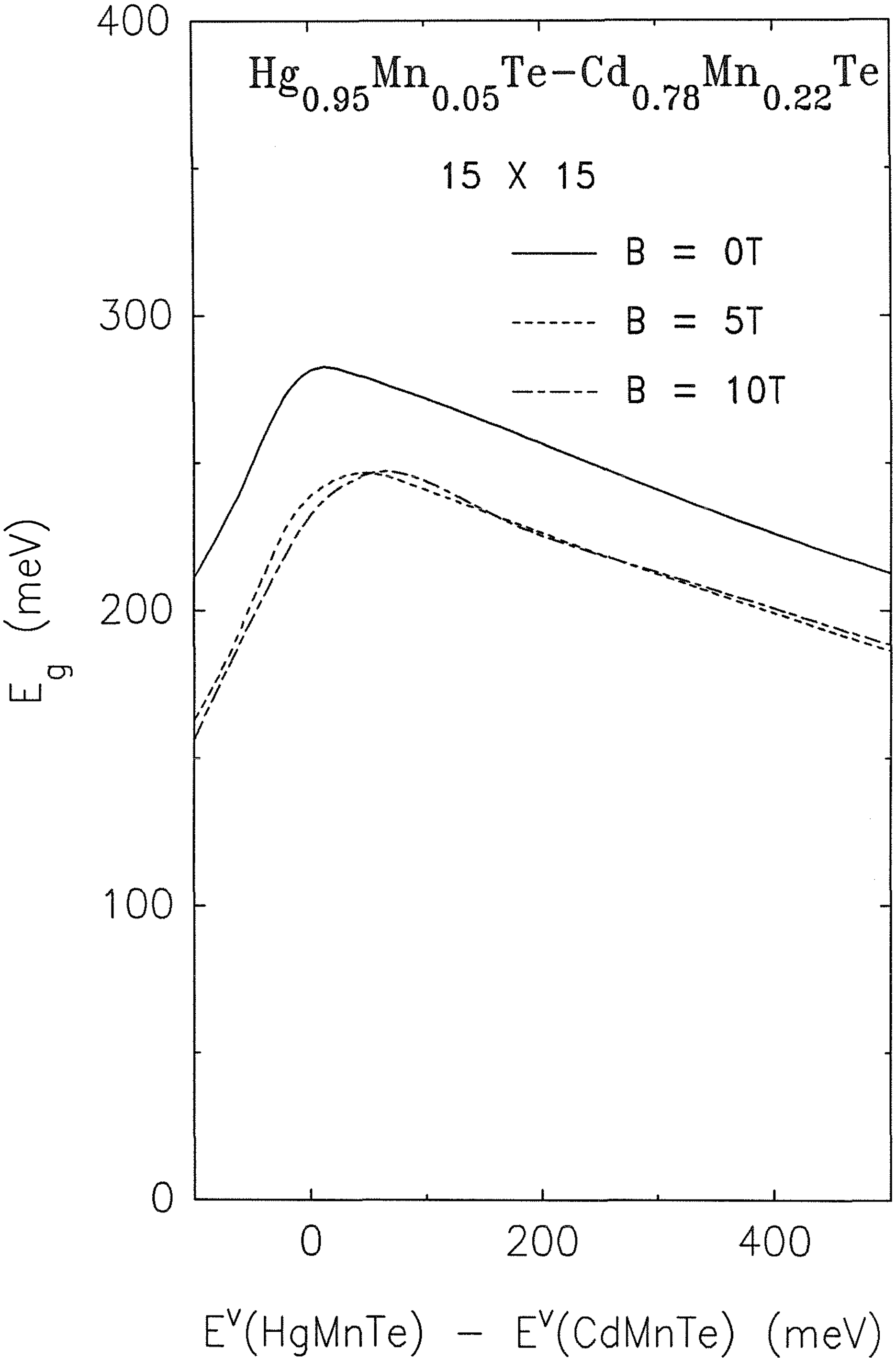

Figure 5.6: Bandgap of the 15 x 15 $Hg_{0.95}Mn_{0.05}Te/Cd_{0.78}Mn_{0.22}Te$ superlattice as a function of the valence band offset at zero temperature for three magnetic fields.

curves become flat as we increase the magnetic field, and hence Landau level shift, which opposes reducing the bandgap. The derivatives of the bandgap with magnetic field at low magnetic field are also shown. At negative valence band offset, the hole is confined in the $Cd_{0.78}Mn_{0.22}Te$ layer where the exchange interaction is larger due to the higher concentartion of Mn^{++} it contains. When the valence band offset becomes positive, the hole is confined in $Hg_{0.95}Mn_{0.05}Te$ where the exchange interaction is smaller due to the lower concentration of Mn^{++} it contains. Consequently, the magnitude of the derivative decreases as the valence band offset increases from negative to positive value. Also notice that, as the intensity of magnetic field increases, the band gap curve becomes more flat. This means that localized spins begin to be saturated and hence the spin-splitting tends to be nearly constant. The band gap therefore does not change as rapid as at low magnetic field.

5.4 Summary

In summary, we have made our first theoretical study of electronic properties of semimagnetic superlattices. The magnetic field is taken to be perpendicular to the layers of superlattices. We have assumed both mean field theory and virtual crystal approximation. Effective-mass approximation has been made in the calculation. Changes in band structures of semimagnetic superlattices have been investigated.

In the wide-gap system, the valence band offset was chosen in accordance with the experiments. In the narrow-gap system, values of effective spin and temperature describing antiferromagnetic cluster formation were obtained by linear extrapolation and/or interpolation extracted from the table for CdMnTe. Some uncertainty is expected to be caused by these choices. We have specifically calcu-

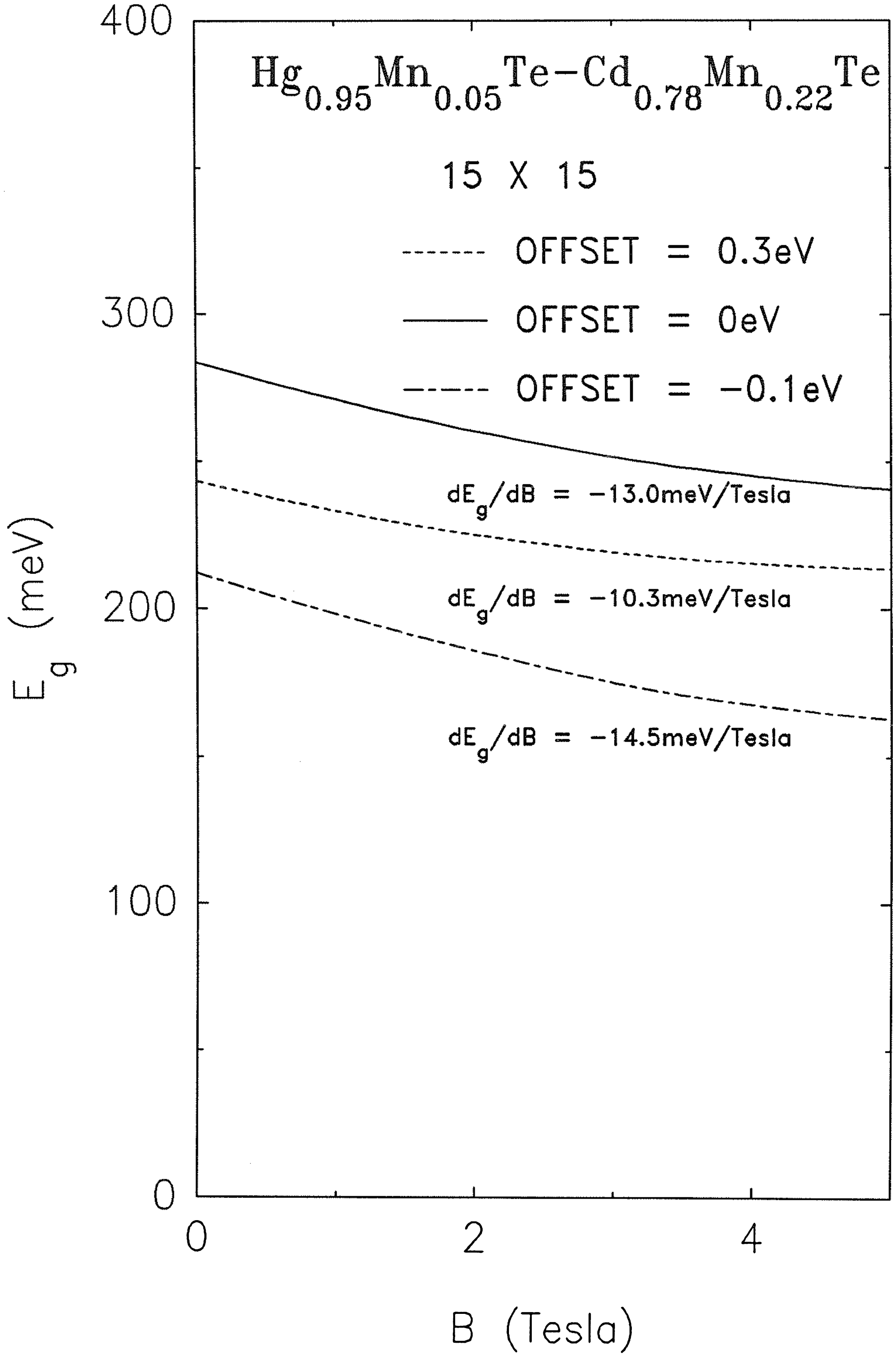

Figure 5.7: Bandgap of the 15 x 15 $Hg_{0.95}Mn_{0.05}Te/Cd_{0.78}Mn_{0.22}Te$ superlattice as a function of magnetic field for three valence band offsets.

lated dependences of the band gap on the layer thickness, temperature, magnetic field and valence band offset for $Hg_{0.95}Mn_{0.05}Te/Cd_{0.78}Mn_{0.22}Te$ and $Cd_{0.8}Mn_{0.2}Te/Cd_{0.7}Mn_{0.3}Te$ superlattices. The exchange interaction is dominant in $Cd_{0.8}Mn_{0.2}Te/Cd_{0.7}Mn_{0.3}T$ superlattices. But the Landau level shift is also important in $Hg_{0.95}Mn_{0.05}Te/Cd_{0.78}Mn_{0.22}Te$ superlattices. Above 5K, the orientations of Mn^{++} spins are randomized, the exchange interaction is small and hence, the bandgap reduction is small. In $Cd_{0.8}Mn_{0.2}Te/Cd_{0.7}Mn_{0.3}T$ system, the valence band offset is small. As a result, holes are not strongly confined in the small band gap ($X = 0.2$ alloy) material layers and the magnetic properties of the superlattice are similar to that of an alloy. In $Hg_{0.95}Mn_{0.05}Te/Cd_{0.78}Mn_{0.22}Te$ system, the bandgap is maximum around zero band offset. The change in the bandgap at low field is found to decrease with the offset varying from negative to positive value, since the site of hole confinement shifts from $Cd_{0.78}Mn_{0.22}Te$ to $Hg_{0.95}Mn_{0.05}Te$ layers. The fraction of change in the bandgap is larger in the narrow-gap material ($\approx 10\%$) than that in the wide-gap material ($\approx 2.5\%$) at a low temperature (such as 5K) and a large magnetic field (such as 5T).

References

1. L. A. Kolodziejski, T. Sakamoto, R. L. Gunshor and S. Datta, Appl. Phys. Lett. **44**, 799 (1984).
2. L. A. Kolodziejski, T. C. Bonsett, R. L. Gunshor, S. Datta, R. B. Bylsma, W. M. Becker and N. Otsuka, Appl. Phys. Lett. **45**, 440 (1984).
3. R. N. Bicknell, R. Yanka, N. C. Giles-Taylor, D. K. Banks, E. L. Buckland and J. F. Schetzina, Appl. Phys. Lett. **45**, 92 (1984).
4. A. Petrou, J. Warnock, R. N. Bicknell, N. C. Giles-Taylor and J. F. Schetzina, Appl. Phys. Lett. **46**, 692 (1985).
5. J. P. Faurie, J. Reno, S. Sivananthan, I. K. Sou, X. Chu, M. Boukerche, and P. S. Wijewarnasuriya, J. Vac. Sci. Technol. A **4**, 2067 (1986).
6. L. A. Kolodziejski, R. L. Gunshor, N. Otsuka, X. C. Zhang, S. K. Chang and A. V. Nurmikko, Appl. Phys. Lett. **47**, 882 (1985).
7. X. C. Zhung, S. K. Chang, A. V. Nurmikko and L. A. Kolodziejski, R. L. Gunshor and S. Datta, Phys. Rev. **B31**, 4056 (1985).
8. X. C. Zhung, S. K. Chang, A. V. Nurmikko, D. Heiman, L. A. Kolodziejski, R. L. Gunshor and S. Datta, Solid State Commun. **56** , 255 (1985).

9. A. V. Nurmikko, X. C. Zhung, S. K. Chang, L. A. Kolodziejski, R. L. Gunshor and S. Datta, J. of Luminescence **34**, 89 (1985).
10. E. D. Isaacs, D. Heiman, J. J. Zayhowski, R. N. Bicknell and J. F. Schetzina, Appl. Phys. Lett. **48**, 275 (1986).
11. D. L. Smith and C. Mailhiot, Phys. Rev. **B33**, 8345(1986); C. Mailhiot and D. L. Smith, Phys. Rev. **B33**, 8360 (1986).
12. M. Jaczynski, J. Kossut, and R. R. Galazka, Phys. Stat. Solids, (b) **88**, 73 (1978).
13. G. Bastard, C. Rigaux, Y. Guldner, J. Mycielski and A. Mycielski, J. Phys. (Paris) **39**, 87 (1978).
14. J. A. Gaj, R. Planel and G. Fishman, Solid State Commun. **29**, 435 (1979).
15. I. I. Lyapilin and I. M. Tsidil'kovskii, Sov. Phys. Usp. **28**(5), 349 (1985). In the calculation, we extend the table of effective temperature and spin given by them with a linear interpolation and/or extrapolation extracted from the table for CdMnTe given in Ref. (14).
16. P. Lawaetz, Phys. Rev. **B10**, 3460 (1971).
17. N. B. Brandt and V. V. Moshchalkov, Adv. in Phys. **33**, 193 (1984).
18. J. K. Furdyna, J. Vac. Sci. Technol. A **4**, 2002 (1986).
19. We neglect the possible formation of a spin glass phase.
20. M. H. Weiler, R. L. Aggarwal and B. Lax, Phys. Rev. **B17**, 3269 (1978).
21. M. von Ortenberg, Phys. Rev. Lett. **49**, 1041 (1982).

Chapter 6

Barrier Phonon-Assisted Inelastic Tunneling in a GaAs-AlAs-GaAs-AlAs-GaAs Structure

6.1 Introduction

This chapter deals with the inelastic electronic tunneling assisted by barrier phonons in a double barrier structure involving GaAs and AlAs. Semiconductor heterostructures involving GaAs and AlAs have been the subject of both theoretical and experimental studies. In GaAs-AlAs-GaAs-AlAs-GaAs structures, AlAs layers act as energy barriers while the middle GaAs layer acts as a well. We will consider GaAs-AlAs-GaAs-AlAs-GaAs double barrier structures which are specifically doped as n-i-i-i-n. In other words, the GaAs electrodes are n-type while the AlAs barriers and the GaAs well are undoped. Observations of resonant tunneling of electrons through double-barrier structures have been reported[1]. Tsu and Esaki[2] have theoretically treated the general case of electronic tunneling through multiple barriers. In the double-barrier case, resonant tunneling was shown by them to give rise to a current maximum (J_p) at the voltage bias (V_a) where the fermi sea of an electrode is aligned in energy with any of the quasi-bound states in the GaAs well. The current drops very rapidly at other voltages. Under such circumstances, the two AlAs barriers act as if they were put together to form a single barrier and block the propagation of the electron. Subsequent works have refined the theory for calculating the barrier transmission (T) and current-voltage (J-V_a) characteristics. Mukheriji and Nag[3] allowed for complexities of the band structure in momentum space such as nonparabolicity. Vessel, Lee and Lockwood[4] considered the difference in mass from layer to layer and took into account the fact that GaAs and AlAs layer could have arbitrary potential energy profiles due to contributions from space charge. In the self-consistent analysis, Ohnishi et al have included the Hartree potential in the calculation of resonant tunneling current[5]. The peak current they calculated agrees with the measured value. However, the measured valley current is greater than the theoretical value by one order of magnitude. The increased valley current cannot be understood within their model[5]. However, all the above theories have assumed conservation of the electronic energy and the momentum parallel to the layer. In other words, only elastic tunneling has been considered. But, in the recent study of GaAs-AlAs-GaAs structure, Collins, Lambe and McGill[6] reported the observation of inelasic tunneling of electrons. In such tunneling, the excitation of AlAs phonons could take away finite amount of energy and momentum from the tunneling electron. Hence, the total energy and the transverse momentum of the tunneling electron are no longer conserved. This involves many-body effects. As we shall show, they could enhance the current off resonance by orders of magnitude in Tsu-Esaki model. This suggests the importance of the inclusion of inelastic tunneling in calculations such as the self-consistent analysis of Ohnishi et al. However, inelastic tunneling has not been included in any of the theories previously mentioned. In this chapter, we present the first theoretical study of the effects on the tunneling current in a double barrier structure due to the electron-phonon interaction. The transfer Hamiltonian method proposed by Bardeen[7] originally for the treatment of the tunneling of electrons through a single barrier structure is extended to calculate phonon-induced inelastic tunneling in a double barrier structure. For illustration, we shall consider the zero temperature case where only phonon emission is possible. In this case, with proper approximations, we obtain analytical expressions which shed some light on the important effects of inelastic tunneling. These effects change I-V characteristics for a double barrier structure.

In Section (6.2), we describe the theory of elastic tunneling. In Section (6.3), we present the theory of inelstic tunneling assisted by barrier phonons. In Section (6.4), we compare I-V characteristics with only elastic tunneling included with that with both elastic and inelstic tunneling included. In Section (6.5), we summarize the study.

6.2 Theory of Elastic Tunneling

In this section, we will discuss analytically the I-V charateristics with only elastic tunneling included. Only the order of magnitude of a quantity will be considered. We define the elastic tunneling as a process in which the energy E and the in-plane wave vector $k_{\|}$ of the tunneling electron are both conserved:

$$\begin{aligned} \Delta E &= 0, \\ \Delta k_{\|} &= 0. \end{aligned}$$

If either one of them is violated, we call it an inelastic tunneling process.

In Figure (6.1), the Γ (i.e. $\vec{k}=0$) conduction band edge diagram is shown. The barrier height (the conduction band off-set) is taken to be 55% of $(E_g^{AlAs} - E_g^{GaAs})$, the band gap difference[9]. We consider only symmetric structures. We assume the voltage drop across each barrier is half of V_a, the voltage bias. The square-barrier approximation is adopted. The dashed line shows the lowest quasi-bound level E_1. With the effective mass approximation, the three-dimensional wave equation may be seperated into transverse and longitudinal parts. The transverse part simply describes the in-plane propagation of a free electron with the effective mass m^*. Hence ψ_t, the transverse part of the wave function, is

$$\psi_t = \frac{1}{\sqrt{A}} \exp(ik_{\|}r_{\|}), \tag{6.1}$$

where A is the cross section area of the structure. The total wave function ψ_l for an incident electron in the left electrode is

$$\psi_l = \psi_t[\exp(ik_l x) + R\exp(-ik_l x)],$$

while the wave function in the right electrode is

$$\psi_r = \psi_t[T\exp(ik_r x)], \tag{6.2}$$

where k_l and k_r are longitudinal wave vectors of the electron in the left and right electrode, respectively. R and T are the reflection and transmission amplitudes. To understand the transport properties, we may simply solve the quantum mechanics for the double barrier system illustrated in Figure (6.1). By matching the wave functions and their derivatives at each discontinuity, the problem is solved. Thus R and T are obtained. It can be verified that we have an approximate expression for T at the resonance energy i.e., $E = E_1$

$$TT^* \sim 1, \tag{6.3}$$

while off the resonance energy i.e., $E \neq E_1$

$$TT^* \sim \exp[-2(\kappa_l + \kappa_r)d], \tag{6.4}$$

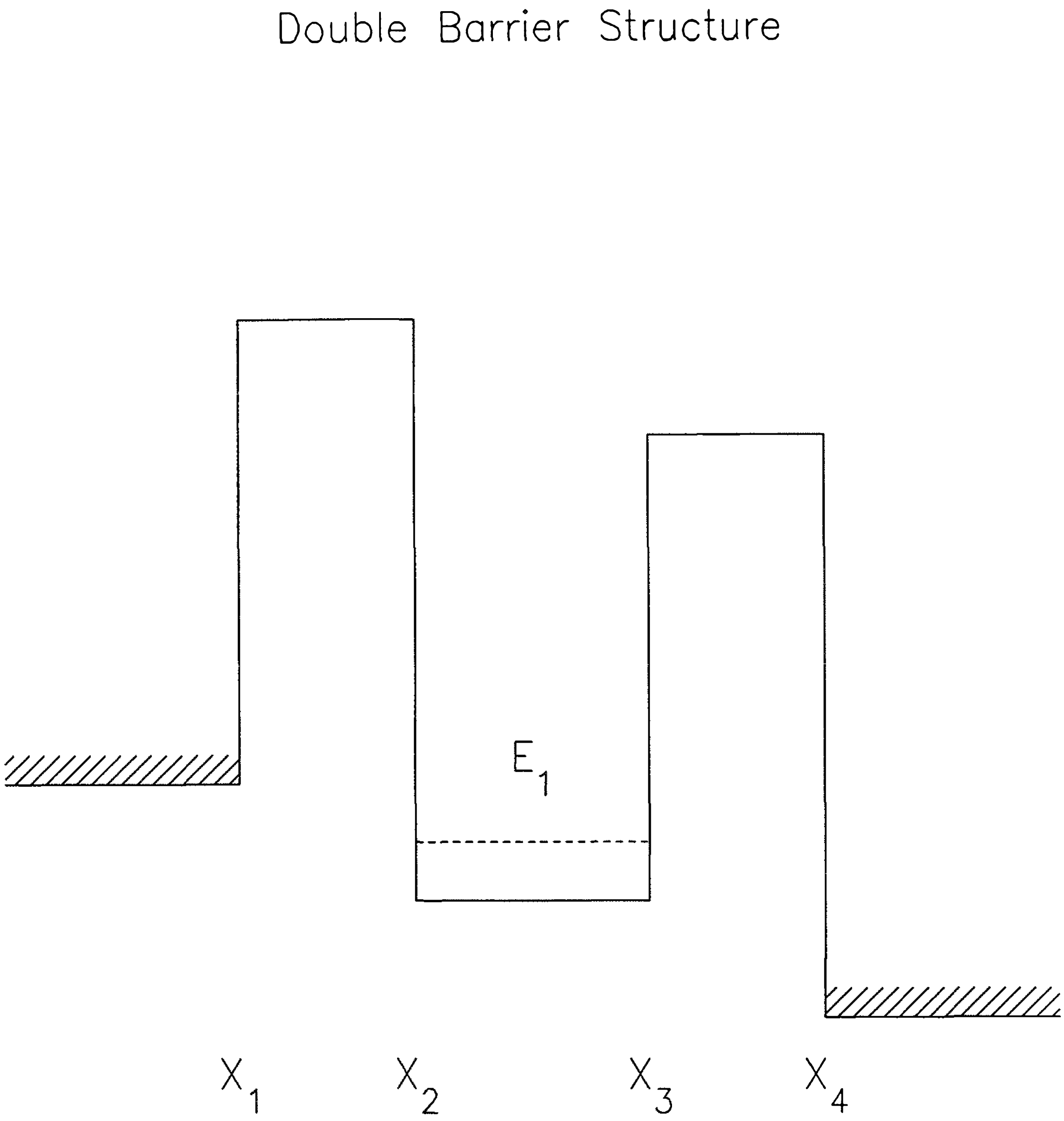

Figure 6.1: The Γ (i.e. $\vec{k} = 0$) conduction band edge diagram of a double barrier structure. The positions of the four interfaces are X_1, X_2, X_3, and X_4. The lowest quasi-bound level is represented by E_1. The two barriers are equally thick. The thickness is equal to d.

where d is the barrier thickness. $i\kappa_l(i\kappa_r)$ is the imaginary wave vectors in the left(right) barrier. In a GaAs-AlAs-GaAs-AlAs-GaAs device, the barrier height is about 1eV while the fermi energy E_f is about a few tens of meV for a dopant density $\sim 10^{18}cm^{-3}$. Hence, the electronic energy is always lower than the barrier height. The wave vector in the barrier is always imaginary.

Note that according to Eq. (6.3) and Eq. (6.4), the ratio of the transmission at resonance to that off resonance is

$$\frac{TT^*_{on}}{TT^*_{off}} \approx \exp[2(\kappa_l + \kappa_r)d].$$

This expression shows that the ratio increases exponentially with the barrier thickness. It shows how rapidly the transmission drops as the energy of the incident electron deviates from that of the quasi-bound level.

It is also useful to work out the resonance width. The width of the resonance is inversely proportional to the lifetime for which the electron stays in the well. The lifetime, in turn, is inversely proportional to the leakage rate $\exp(-2\kappa d)$, where κ is the smaller one of κ_l and κ_r (in practice, $\kappa_l \approx \kappa_r$ in our calculation). Therefore, by dimensional argument, the width of the resonance is

$$\delta E \sim E_1 \exp(-2\kappa d). \tag{6.5}$$

Knowing the width and the transmission at and off resonance will allow us to represent the transmission approximately by a Dirac-δ function with a proper pre-factor. From Eq. (6.3), Eq. (6.4) and Eq. (6.5), we model the transmission TT^* by

$$TT^* \approx E_1 \exp(-2\kappa d)\delta(E_\perp + eV_a/2 - E_1), \tag{6.6}$$

where $E_\perp$ is the energy correponding to the perpendicular motion of the tunneling electron. In fact, this expression agrees with that obtained in the WKB approximation.

The above approximate expressions are very useful for the estimation of current flowing in the tunneling device at a certain bias. In the following, we will employ them to calculate the current density at and off resonance. To find the net tunneling current, we need to consider electronic tunneling both from the left and from the right Fermi sea. The net current density is

$$J = \frac{e}{4\pi^3\hbar}\int d^2k_{\parallel}\int_0^{\infty} dk_l \int_0^{\infty}[f(E) - f(E')]TT^*\frac{\partial E}{\partial k_l}, \tag{6.7}$$

where $f(E)$ is Fermi distribution function. E is the energy of the incident electron with respect to the conduction band edge of the left barrier and E' is the energy of the transmitted electron with respect to the conduction band edge of the right electrode. They are related by

$$E' = E + eV_a. \tag{6.8}$$

At low temperature, Eq. (6.7) reduces to

$$J \approx \frac{em^*}{2\pi^2\hbar^3}\int_0^{E_F}(E_F - E_l)TT^* dE_l. \tag{6.9}$$

When the bias is such that the left Fermi sea is aligned in energy with the quasi-bound level, the current reaches its maximum. Putting Eq. (6.6) in Eq.(6.9), we obtain the peak current density J_p

$$J_p \approx \frac{em^*}{2\pi^2\hbar^3}E_1 E_F \exp(-2\kappa d). \tag{6.10}$$

On the other hand, when the bias is off the resonance value, putting Eq. (6.4) in Eq. (6.9) results in the valley value J_v

$$J_v \approx \frac{em^*}{2\pi^2\hbar^3}\left[\frac{E_F}{2}\right]^2 \exp(-4\kappa d). \tag{6.11}$$

From Eq. (6.10) and Eq. (6.11), we obtain the ratio of the peak value to the valley value

$$\frac{J_p}{J_v} \approx \frac{E_1}{E_F}\exp(2\kappa d). \tag{6.12}$$

Thus, the ratio increases exponentially with the barrier thickness.

6.3 Theory of Inelastic Tunneling

We use the transfer Hamiltonian method proposed by Bardeen[7]. We extend the method to treat the inelastic tunneling of an electron through the excitation of an AlAs phonon.

Parameters specifying the device in question are given in the following. The cross section area is A. Each electrode has the length L. The effective mass of the electron is taken to be m^* whether in GaAs or AlAs. The left barrier and the right barrier are taken to be equally thick: $d_1 = d_2 = d$. w is the width of the well. The voltage bias V_a is such that the lowest quasi-bound level E_1 is lower in energy than the conduction band edge of the left electrode (see Figure (6.1)). We choose the states ψ_r and ψ_l so that ψ_r is matched to the correct solution for $x \geq x_2$ but decays in the region $x \leq x_1$ instead of satisfying the wave equation, and, similarly, ψ_l continues to decay for $x \geq x_2$. Then ψ_r is a correct solution for the Hamiltonian H for $x \geq x_1$ and ψ_l is correct for $x \leq x_2$. With WKB approximation, we have

$$\begin{aligned}
\psi_l(x) &= \sqrt{\frac{2}{AL}} e^{ik_\| x_\|} \sin(k_l x + \gamma_l), \qquad x \leq x_1, \\
\psi_l(x) &= \sqrt{\frac{k_l}{\kappa_l}} \frac{e^{ik_\| x_\|} e^{-\kappa_l (x - x_1)}}{\sqrt{2AL}} \\
&= \frac{e^{ik_\| x_\|}}{\sqrt{AL}} \chi_l(x), \qquad x \geq x_1, \qquad (6.13)
\end{aligned}$$

where k_l is the wave vector of the electron in the left electrode, $i\kappa_l$ is the imaginary wave vector in the left barrier, and $\chi_l(x)$ is defined in the equation. Similarly,

$$\begin{aligned}
\psi_r(x) &= \sqrt{\frac{2}{AL}} e^{ik_\| x_\|} \sin(k_r x + \gamma_r), \qquad x \geq x_4, \\
\psi_r(x) &= \sqrt{\frac{2}{AL}} \sqrt{\frac{k_r}{\kappa_r}} \frac{e^{ik_\| x_\|} e^{-\kappa_r (x - x_1)}}{\sqrt{[\sin(k_w w)]^2 e^{-2\kappa_2 d_2} + [4\cos(k_w w)]^2 e^{2\kappa_2 d_2}}} \\
&= \sqrt{\frac{1}{AL}} e^{ik_\| x_\|} \chi_r, \qquad x \leq x_2, \qquad (6.14)
\end{aligned}$$

where k_r is the wave vector in the right electrode, $i\kappa_r$ is the imaginary wave vector in the left barrier, k_w is the wave vector in the well, $i\kappa_2$ is the imaginary wave vector in the right barrier, and $\chi_r(x)$ is defined in the equation. The electron-phonon coupling in the left AlAs barrier gives arise to the interaction Hamiltonian

$$H_{ep}^{a} = iD_{\Gamma}(\frac{\hbar q}{2\rho v_s V_{AlAs}})(a_{\vec{q}\lambda}^{+} e^{i\vec{q}\cdot\vec{r}} + a_{\vec{q}\lambda} e^{-i\vec{q}\cdot\vec{r}}) \tag{6.15}$$

for the deformation-potential (DP) coupling due to the longitudinal acoustical (LA) phonon mode $\vec{q}\lambda$, where $\vec{q}$ is the phonon wave vector and λ specifies the polarization[1]. Here, D_Γ is the deformation potential for Γ-valley electrons, ρ is the density, v_s is the sound velocity in AlAs and V_{AlAs} is the volume of the left barrier. On the other hand,

$$H_{ep}^{o} = \frac{4\pi i}{q}[\frac{\hbar\omega}{8\pi V_{AlAs}}(\frac{1}{\epsilon_\infty} - \frac{1}{\epsilon_0})]^{1/2}(a_{\vec{q}\lambda}^{+} e^{-i\vec{q}\cdot\vec{r}} - a_{\vec{q}\lambda} e^{i\vec{q}\cdot\vec{r}}) \tag{6.16}$$

for the polar (PO) coupling due to the longitudinal optical (LO) phonon mode $\vec{q}\lambda$[1]. ϵ_0 and ϵ_∞ are the dielectric constants at zero and optical frequencies, respectively. Other kinds of electron-phonon coupling, piezoelectric coupling for example, are much weaker and much less important[1]. They are not considered here. According to Fermi's golden rule, the transition rate of an electron from the left electrode to the right electrode, with the excitation of one AlAs phonon, is given by

$$w_{lr} = (\frac{2\pi}{\hbar})|M_{lr}|^2\delta(\epsilon_l + eV_a - \epsilon_r - \hbar\omega), \tag{6.17}$$

where $\hbar\omega$ is the phonon energy, and ϵ_l and ϵ_r are the kinetic energies of the electron in the left and right electrode, respectively. Here, the matrix element M_{lr} is given by

$$M_{lr} =< \Psi_i|H_{ep}|\Psi_f >, \tag{6.18}$$

where Ψ_i and Ψ_f are the initial and final states. The temperature is taken to be zero to simplify our analysis. At zero temperature, only phonon emission needs to be considered. The inelastic tunneling current is

$$J_{in} = \frac{4\pi e}{\hbar} \sum_{\vec{q}\lambda} \sum_{\vec{k}} \sum_{\vec{k'}} |M|^2 f(\epsilon_k)[1 - f(\epsilon_{k'})]\delta(\epsilon_k + eV_a - \epsilon_{k'} - \hbar\omega) \tag{6.19}$$

at zero temperature. The general expression for J_{in} at a finite temperature may be derived with the use of many-body theory. Bennett et al[8] have given the derivation of the formula for the single barrier case. We do not attempt to treat finite temperature case, however. Replacing $\sum$ with $\int$, we have (see Appendix B)

$$\begin{aligned} J_{in} &= \frac{4\pi e}{\hbar} A \sum_{\lambda} \int \frac{d^3q}{(2\pi)^3} |U_q|^2 \int \frac{d^3k}{(2\pi)^3} \int \frac{d^3k'}{(2\pi)^3} |T(q_\perp; k_\perp, k'_\perp)|^2 f(\epsilon_k)[1 - f(\epsilon_{k'})] \\ &\times \quad \delta(\vec{k}_{\|} - \vec{k'}_{\|} - \vec{q}\|)(2\pi)^2 \delta(\epsilon_k + eV_a - \epsilon_{k'} - \hbar\omega), \end{aligned}$$

where T is the overlap integral

$$T(q_\perp; k_\perp, k'_\perp) = \int_{x_1}^{x_2} e^{iq_\perp x} \chi_l^* \chi_r dx. \tag{6.20}$$

Suppose now the electron is scattered into the quasi-bound level, then ψ_r in the left barrier would be enhanced by the exponential factor $e^{\kappa_2 d_2}$. This can be verified by setting $\cos(k_w w)$ to zero in Eq. (6.14) when near resonance. This would in turn increase T by the same factor. Therefore, the contribution to the inelastic current for such a process would dominate over others without taking the resonant level in the tunneling. It turns out that for PO coupling, we have

$$\begin{aligned} J_{in} \quad &\geq \quad \frac{2Aem^{*2}d_1^2}{(2\pi)^3 \hbar^5 \kappa_0^2} e^{-2\kappa_0 d_1} e^{E_1/V_b} \frac{E_1}{2} \times \\ & \quad \frac{2}{\pi} e^2 \hbar\omega \frac{k_F^4}{q_0} (1/\epsilon_0 - 1/\epsilon_\infty) tan^{-1}(1/q_0 d_1). \end{aligned} \tag{6.21}$$

For DP coupling, we have

$$\begin{aligned} J_{in} \quad &\geq \quad \frac{2Aem^{*2}d_1^2}{(2\pi)^3 \hbar^5 \kappa_0^2} e^{-2\kappa_0 d_1} e^{E_1/V_b} \frac{E_1}{2} \frac{\pi k_F^4}{2\pi^2} \frac{D_\Gamma^2 \hbar}{2\rho v_s} \times \\ & \quad \{d_1^{-1}(d_1^{-2} + q_0^2)^{1/2} + q_0^2 \sinh^{-1}[(q_0 d_1)^{-1}]\}. \end{aligned} \tag{6.22}$$

Here, E_b is the zero bias barrier height, $\kappa_0 = \sqrt{2m^*E_b/\hbar^2}$, $V_b = 2E_b/\kappa_0 d_1$, and q_0 satisfies $\hbar^2 q_0^2/2m^* = eV_a/2 - \hbar\omega - E_1$. Derivation of the above equations is described in Appendix B.

6.4 Comparison of Elastic and Inelastic Tunneling

In this section, we compare contributions to the current from the elastic and the inelastic process. We consider only the inelastic process induced by PO coupling or DP coupling. Inelastic processes induced by other couplings will further increase the inelastic current. Therefore, the inelastic current we are concerned with here is a lower bound of the actual value. However, even without a complete knowledge of the inelastic current, we can still demonstrate the dramatic change in order of magnitude of the current which is due to inelastic processes.

In Figure (6.2), we plot the lower limit of J_{in}/J_e, the ratio of inelastic current to elastic current, versus barrier thickness for biased symmetric structures with $w = 50\,\text{Å}$, $E_f = 50\text{meV}$ and $V_a = 0.4\text{V}$. Both LO and LA phonon-induced effects are shown. For thin barrier cases where $d = 20\,\text{Å}$, polar coupling induces inelastic current comparable to the elastic current. As can be seen, deformation potential coupling has much smaller effects than polar coupling. The reason is that the PO coupling is much stronger than the DP coupling. We may neglect the contribution from DP coupling in comparison to that from PO coupling. Effects of both coupling increase as barrier becomes wider, due to the exponential enhancement in the right wave function ψ_r. For the thick barrier case where $d = 40\,\text{Å}$, polar coupling even gives rise to an inelastic current which is a thousand times as large as the elastic one.

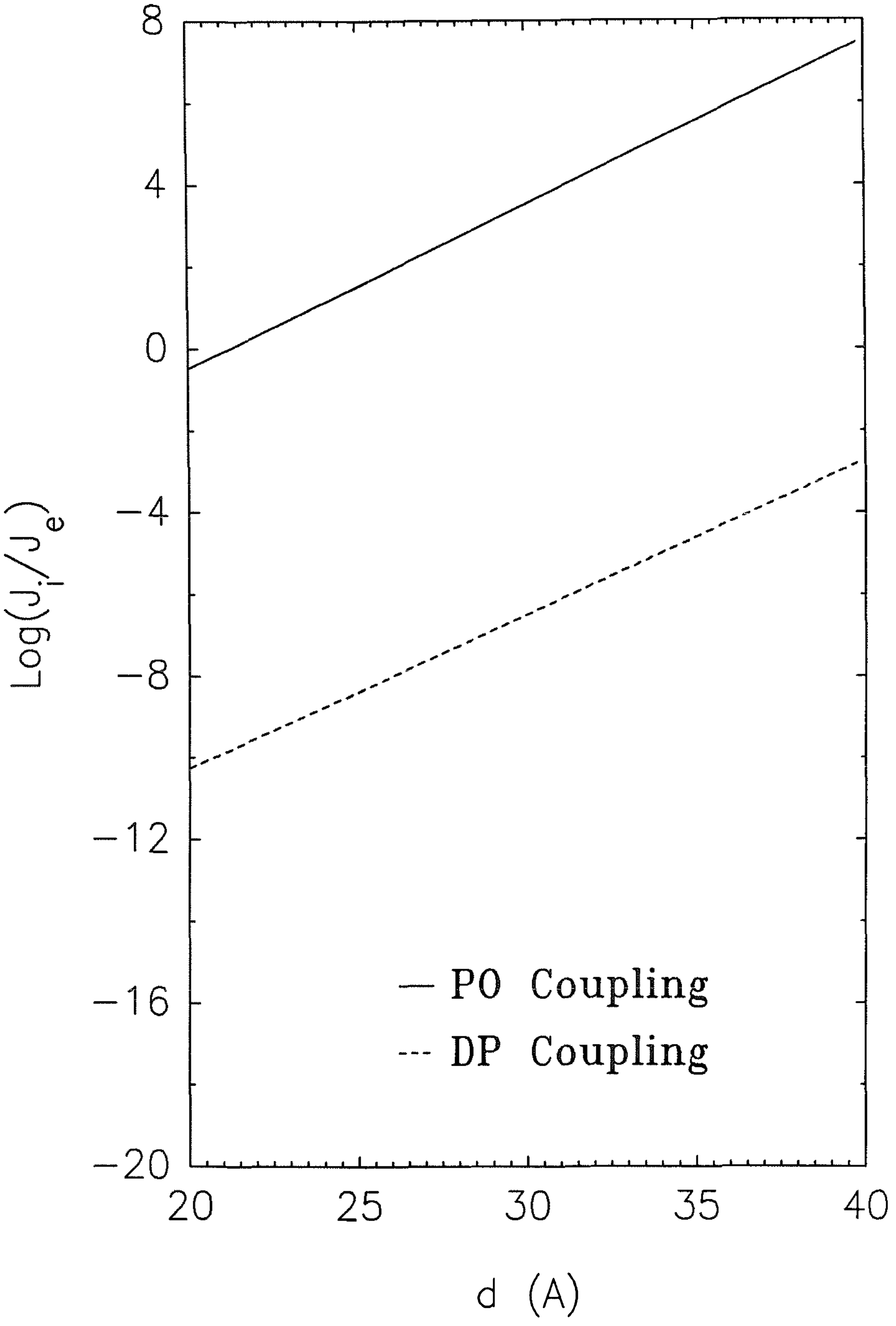

Figure 6.2: The lower limit of J_{in}/J_e, the ratio of inelastic current to elastic current, versus barrier thickness for biased symmetric structures with $w = 50\,\text{Å}$, $E_f = 50\text{meV}$ and $V_a = 0.4\text{Volts}$. $E_1 \approx 150meV$ with respect to the conduction band edge of the GaAs well. Both LO and LA phonon-induced effects are shown.

In Figure (6.3), we plot the upper limit of the ratio of the resonant current, which occurs at $V_a = 0.3V$, to the current at $V_a = 0.4V$, which occurs off resonance, versus barrier thickness. The dotted line is obtained with Tsu-Esaki model[2], which includes only elastic process. In that case, the ratio shown here is equal to the peak to valley ratio of the J-V curve. The solid line is obtained with inelastic tunneling included. The peak current is mostly due to the elastic tunneling, since, at resonance, the elastic current is much larger than the inelastic current. The current off resonance is largely due to the inelastic tunneling, since the inelastic current is much larger than the elastic current, as shown in Figure (6.2). The ratios shown by the two curves are comparable for thin barrier cases. However, as the barrier becomes thicker, the solid curve only varies slowly, since both J_{on} and J_{off} have same exponential dependence (see Eq. (6.3) and Eq. (6.21)). For barrier thickness equal to 40 Å, magnitudes of the two ratios differ by seven in the natural log scale. The theory with the inelastic process included predicts a much smaller value of ratio for thick barrier cases.

In Figure (6.4), the upper bound of the ratio are shown versus Fermi energy for the symmetric structure with $d = 40$ Å and $w = 50$ Å. The solid curve includes contribution from the inelastic process and the dashed curve includes only contribution from the elastic process. The curves are shown for the region from $E_f = 5$meV to $E_f = 50$meV corresponding to dopant density from $10^{17}/cm^3$ to $10^{18}/cm^3$ currently used in the tunneling experiment. We see that both curves behave similarly as Fermi energy changes. The difference between them is maintained through the Fermi energy range of interest. This shows the importance of the inelastic process for both low and high doping cases.

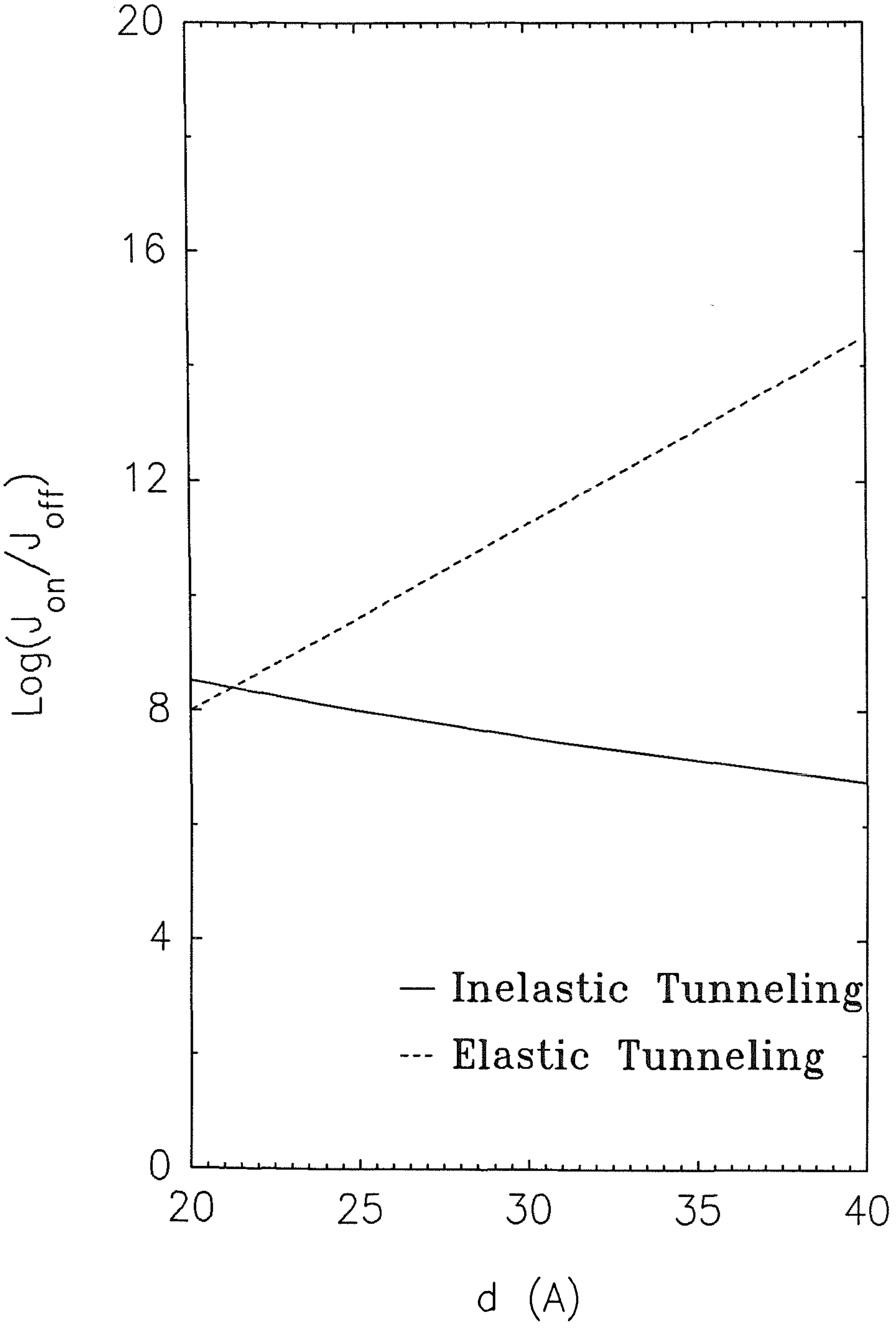

Figure 6.3: The upper bound of the peak current at $V_a = 0.3V$ (at resonance) to the current at $V_a = 0.4V$ (off resonance) versus barrier thickness with and without the inelastic part of the current included for biased symmetric structures with $w = 50\,\text{Å}$, and $E_f = 50\text{meV}$.

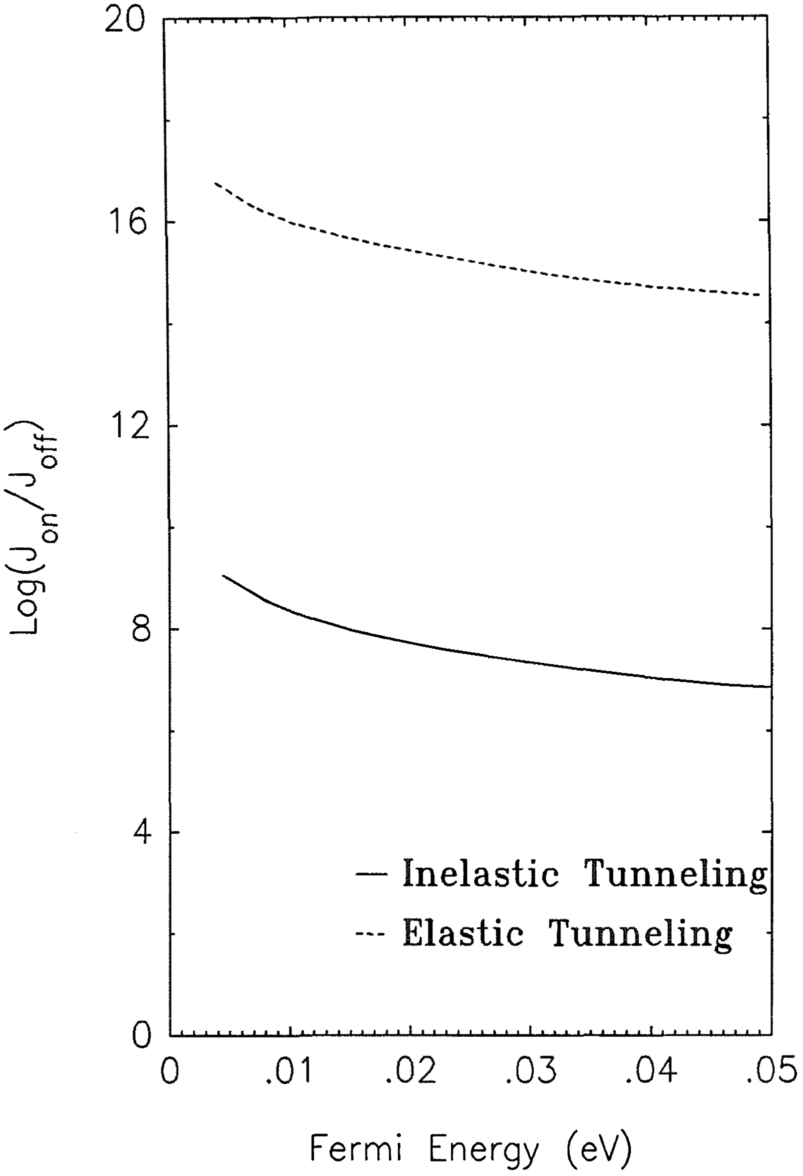

Figure 6.4: The upper bound of the ratio of the peak current to that at $V_a = 0.4V$ for the elastic and inelastic processes are shown versus fermi energy for the symmetric structure with $d = 40\,\text{Å}$ and $w = 50\,\text{Å}$. The curves are shown for the region from $E_f = 5$meV to $E_f = 50$meV corresponding to dopant density from $10^{17}/cm^3$ to $10^{18}/cm^3$ currently used in the tunneling experiment. The solid curve includes contribution from the inelastic process. The dashed curve includes only contribution from the elastic process.

6.5 Summary

In summary, the inclusion of the inelastic tunneling in the theory for double barrier structures is very important. We have studied specifically the inelastic tunneling induced by phonons. Two types of coupling have been considered. The polar optical coupling is much stronger than the deformation potential coupling, and hence the current induced by PO coupling is much larger than that by DP coupling. Because of similar reason, we expect the effect of piezoelectric (PE) coupling is also negligibile in comparison to that of PO coupling.

The electron-phonon interaction induces a channel through which the electron can tunnel much more readily than through the elastic channel. With the excitation of a barrier phonon, the electron can utilize the quasi-bound level to tunnel through the barrier. The *inelastic resonant tunneling* enhances the current off resonance by orders of magnitude. The effects are best reflected in the big difference between the magnitudes of current ratios which are predicted, with and without inclusion of electron-phonon coupling, in the simple model of Tsu and Esaki[2]. We expect the inclusion of inelastic processes to be important in any refined theory such as the self-consistent analysis of Ohnishi[5]. In our analysis, the difference under some circumstance can be as large as seven in the natural log scale. The study of the particular phonon-induced inelastic tunneling indicates the importance of general inelastic tunneling in a double barrier structure. Other mechanisms such as impurity scattering could also be critical to current transport in a double barrier structure.

References

1. L. L. Chang, L. Esaki, and R. Tsu, Appl. Phys. Lett., **24**, 593 (1974).
2. R. Tsu and L. Esaki, Appl. Phys. Lett., Vol 22, No. 11, 562 (1973).
3. D. Mukherji and B. R. Nag, Phys. Rev. **B 12**, 4338 (1975).
4. M. O. Vessell, Johnson Lee, and H. F. Lockwood, J. Appl. Phys. **54**(9), 5206 (1983).
5. H. Ohnishi, T. Inata, S. Muto, N. Naoki, and A. Shibatomi, Appl. Phys. Lett. **49** (19), 1248 (1986).
6. R. T. Collins, J. Lambe, T. C. McGill, and R. D. Burnham, Appl. Phys. Lett. **44**, 532 (1984).
7. J. Bardeen, Phys. Rev. Letters 6:57 (1961).
8. A. J. Bennett, C. B. Duke, and S. D. Silverstein, Phys. Rev. Vol 176, No. 3, 969 (1968).
9. J. Batey, and S. L. Wright, J. Appl. Phys. **59**, 200 (1986).

Appendix A

$\vec{k} \cdot \vec{p}$ Theory for Semimagnetic Semiconductor Superlattices: Derivations and Matrices

A.1 Introduction

In this appendix, we derive the effective-mass Hamiltonian. We also give Hamiltonian matrix and current density matrices involved in the calculation of band structures of *semimagnetic semiconductor superlattices.*

In Section (A.2), we derive effective-mass Hamiltonian equation for a semimagnetic semiconductor under the influence of a magnetic field. In Section (A.3), we describe the Hamiltonian matrix for a zinc-blende structure. In Section (A.4), we give the current density matrices.

A.2 Derivation of Effective-Mass Equation

The Hamiltonian H_l of constituent material l in the presence of a magnetic field $\vec{B}$, which is taken to be in z-direction, is

$$\begin{aligned} H_l &= \frac{(\vec{P}+e\vec{A}/c)^2}{2m} + \langle V\rangle + [V_l - \langle V\rangle] + \frac{\hbar}{4m^2c^2}\left[\nabla V \times (\vec{P}+\frac{e}{c}\vec{A})\right]\cdot\vec{\sigma} \\ &\quad + \frac{e\hbar}{2mc}\vec{\sigma}\cdot\vec{B} + H_\epsilon, \end{aligned} \tag{A.1}$$

where $\vec{A}$ is the vector potential of magnetic field $\vec{B}$, and H_ϵ is the exchange interaction between a band electron and localized d-level electrons, which is treated within mean-field approximation.

For each constituent material, we want to solve

$$H_l\Phi_l = E_l\Phi_l \tag{A.2}$$

with perturbation theory. Basis functions for perturbation calculation are taken to be eigenstates U_β of the reference Hamiltonian H_R at $\vec{k}=0$, which is

$$H_R = \frac{\vec{P}^2}{2m} + \langle V\rangle. \tag{A.3}$$

Within effective-mass approximation,

$$\Phi_l = \sum_\beta C_\beta f_\beta(\vec{r})U_\beta(\vec{r})$$

with normalization

$$\int_{unit\ cell} U_\beta^*(\vec{r})U_\beta(\vec{r})d^3r = \int_\Omega f_\beta^*(\vec{r})f_\beta(\vec{r})d^3r = 1. \tag{A.4}$$

The $f_\beta(\vec{r})$'s are slowly varying on the scale of a unit cell. In other words, $f_\beta(\vec{k}) \approx 0$ when $|\vec{k}| \approx |\vec{G}|$. We Fourier-analyze $f_\beta(\vec{r})$ and write

$$f_\beta(\vec{r}) = \sum_{\vec{k}} f_\beta(\vec{k})e^{i\vec{k}\cdot\vec{r}}, \tag{A.5}$$

Then, substituting Eq. (A.1), Eq. (A.4), and Eq. (A.5) into Eq. (A.2), we now have

$$\sum_\beta\sum_{\vec{k}} C_\beta f_\beta(\vec{k})e^{i\vec{k}\cdot\vec{r}}\{\frac{(\vec{k}+e\vec{A}/c)^2}{2m} + \frac{\vec{P}^2}{2m} + \frac{(\vec{k}+e\vec{A}/c)\cdot\vec{P}}{m}$$

$$
\begin{aligned}
&+\langle V\rangle + [V_l - \langle V\rangle] + \frac{\hbar}{4m^2c^2}(\nabla V \times \vec{P})\cdot\vec{\sigma} \\
&+\frac{\hbar}{4m^2c^2}\left[\nabla V \times (\vec{k} + \frac{e}{c}\vec{A})\right]\cdot\vec{\sigma} + \frac{e\hbar}{2mc}\vec{\sigma}\cdot\vec{B} + H_\epsilon\}U_\beta(\vec{r}) \\
= \;& E_l\sum_\beta\sum_{\vec{k}} C_\beta f_\beta(\vec{k})e^{i\vec{k}\cdot\vec{r}}U_\beta(\vec{r}). \qquad\qquad (A.6)
\end{aligned}
$$

The derivation of the effective-mass equation for $f_\beta(\vec{r})$ involves lengthy manipulations. We shall only sketch important steps. Multiplying Eq. (A.6) by $U_{\beta'}(\vec{r})e^{i\vec{k}'\cdot\vec{r}}$, then integrating over all space, a set of simultaneous equations are obtained for $\vec{k}$-space amplitudes $f_\beta(\vec{k})$'s. In the derivation, the approximation is used that $f_\beta(\vec{k}) \approx 0$ when $|\vec{k}| \approx |\vec{G}|$. We then go back to $\vec{r}$-space by multiplying the $\vec{k}$-space equations by $e^{i\vec{k}'\cdot\vec{r}}$ and summing over $\vec{k}'$. We thus end up with the equation

$$
\begin{aligned}
&\sum_\beta\{\epsilon_\beta\delta_{\beta\beta'} + \frac{(\vec{P}+e\vec{A}/c)^2}{2m}\delta_{\beta\beta'} + \\
&\frac{(\vec{P}+e\vec{A}/c)}{m}\cdot\langle U_{\beta'}|\vec{P} + \frac{\hbar}{4mc^2}(\vec{\sigma}\times\nabla V)|U_\beta\rangle + \\
&\langle U_{\beta'}|V_l - \langle V\rangle|U_\beta\rangle + \langle U_{\beta'}|\frac{\hbar}{4m^2c^2}(\nabla V \times \vec{P})\cdot\vec{\sigma}|U_\beta\rangle \\
&+\frac{e\hbar}{2mc}\langle U_{\beta'}|\vec{\sigma}\cdot\vec{B}|U_\beta\rangle + \langle U_{\beta'}|H_\epsilon|U_\beta\rangle\}C_\beta f_\beta(\vec{r}) \\
= \;& E_l C_{\beta'}f_{\beta'}(\vec{r}). \qquad\qquad (A.7)
\end{aligned}
$$

Next, we shall reduce the dimension of the above simultaneous equations in the spirit of Löwdin perturbation theory. We divide the amplitudes $f_\beta(\vec{r})$'s into two sets corresponding to the near-in states and far-out states. We label them by "d" and "α", respectively. In the following, the use of perturbation theory will allow us to decouple equations for "d" states from those for "α" states. We now rewrite Eq. (A.7) in terms of the new labels. For $f_d(\vec{r})$'s

$$
\begin{aligned}
&\sum_d\Bigg[\epsilon_d\delta_{dd'} + \frac{(\vec{P}+e\vec{A}/c)^2}{2m}\delta_{dd'} + \\
&\frac{(\vec{P}+e\vec{A}/c)}{m}\cdot\langle U_{d'}|\vec{P} + \frac{\hbar}{4mc^2}(\vec{\sigma}\times\nabla V)|U_d\rangle + \\
&\langle U_{d'}|V_l - \langle V\rangle|U_d\rangle + \langle U_{d'}|\frac{\hbar}{4m^2c^2}(\nabla V \times \vec{P})\cdot\vec{\sigma}|U_d\rangle +
\end{aligned}
$$

$$\begin{aligned}
&\frac{e\hbar}{2mc}\langle U_{d'}|\vec{\sigma}\cdot\vec{B}|U_d\rangle + \langle U_{d'}|H_\epsilon|U_d\rangle\Big] C_d f_d(\vec{r}) + \\
&\sum_\alpha \Big[\frac{(\vec{P}+e\vec{A}/c)}{m}\cdot\langle U_{d'}|\vec{P}+\frac{\hbar}{4mc^2}(\vec{\sigma}\times\nabla V)|U_\alpha\rangle + \\
&\langle U_{d'}|V_l-\langle V\rangle|U_\alpha\rangle\Big]\, C_\alpha f_\alpha(\vec{r}) \\
= \;& E_l C_{d'} f_{d'}(\vec{r}). \qquad \text{(A.8)}
\end{aligned}$$

For $f_\alpha(\vec{r})$'s, we similarly have

$$\begin{aligned}
&\sum_\alpha \Big[\epsilon_\alpha\delta_{\alpha\alpha'} + \frac{(\vec{P}+e\vec{A}/c)^2}{2m}\delta_{\alpha\alpha'} + \\
&\frac{(\vec{P}+e\vec{A}/c)}{m}\cdot\langle U_{\alpha'}|\vec{P}+\frac{\hbar}{4mc^2}(\vec{\sigma}\times\nabla V)|U_\alpha\rangle + \\
&\langle U_{\alpha'}|V_l-\langle V\rangle|U_\alpha\rangle + \langle U_{\alpha'}|\frac{\hbar}{4m^2c^2}(\nabla V\times\vec{P})\cdot\vec{\sigma}|U_\alpha\rangle + \\
&\frac{e\hbar}{2mc}\langle U_{\alpha'}|\vec{\sigma}\cdot\vec{B}|U_\alpha\rangle + \langle U_{\alpha'}|H_\epsilon|U_\alpha\rangle\Big] C_\alpha f_\alpha(\vec{r}) + \\
&\sum_d \Big[\frac{(\vec{P}+e\vec{A}/c)}{m}\cdot\langle U_{\alpha'}|\vec{P}+\frac{\hbar}{4mc^2}(\vec{\sigma}\times\nabla V)|U_d\rangle + \\
&\langle U_{\alpha'}|V_l-\langle V\rangle|U_d\rangle\Big]\, C_d f_d(\vec{r}) \\
= \;& E_l C_{\alpha'} f_{\alpha'}(\vec{r}). \qquad \text{(A.9)}
\end{aligned}$$

In Eq. (A.8) and Eq. (A.9) we keep matrix elements of the momentum operator $\vec{P}$ and pseudopotential difference $\Delta V_l \equiv V_l - \langle V\rangle$ between d-states and α-states. Other terms which couple d-states with α-states, being small, have been dropped. In Eq. (A.8) and Eq. (A.9), the coupling of f_d with f_α appears explicitly.

We now look for solutions made up mostly of the d-states, i.e., those which contain $C_d f_d(\vec{r})$'s as zeroth-order terms and $C_\alpha f_\alpha(\vec{r})$'s as first-order terms. With this in mind, we will decouple Eq. (A.8) from Eq. (A.9). First, we solve Eq. (A.9) for $C_\alpha f_\alpha(\vec{r})$'s in terms of $C_d f_d(\vec{r})$'s. It turns out that, with E_l replaced by ϵ^0, the average energy for the near-in states,

$$\begin{aligned}
C_\alpha f_\alpha(\vec{r}) \;=\;& \frac{1}{\epsilon_0-\epsilon_\alpha}\sum_d \Big[\frac{(\vec{P}+e\vec{A}/c)}{m}\cdot\langle U_\alpha|\vec{P}+\frac{e}{c}\vec{A}|U_d\rangle + \\
&\langle U_\alpha|\Delta V_l|U_d\rangle\Big]\, C_d f_d(\vec{r}). \qquad \text{(A.10)}
\end{aligned}$$

Putting Eq. (A.10) back in Eq. (A.8), we obtain for $C_d f_d(\vec{r})$'s the *effective-mass equation*

$$
\begin{aligned}
&\sum_d \Pi_{d'd;l} C_d f_d(\vec{r}) \\
\equiv\ & \sum_d \Bigg[(\epsilon_d \delta_{dd'} + (\vec{P} + \frac{e}{c}\vec{A}) \cdot \overline{\overline{D}} \cdot (\vec{P} + \frac{e}{c}\vec{A}) + \frac{(\vec{P} + e\vec{A}/c)}{m} \cdot \overline{V} + \langle U_{d'} | \Delta V_l | U_d \rangle \\
& + \sum_\alpha \frac{\langle U_{d'} | \Delta V_l | U_\beta \rangle \langle U_\beta | \Delta V_l | U_d \rangle}{\epsilon_0 - \epsilon_\beta} + \frac{\hbar}{4m^2c^2} \langle U_{d'} | (\nabla V \times \vec{P}) \cdot \vec{\sigma} | U_d \rangle \\
& + \frac{e\hbar}{2mc} \langle U_{d'} | \vec{\sigma} \cdot \vec{B} | U_d \rangle + \langle U_{d'} | H_\epsilon | U_d \rangle \Bigg] C_d f_d(\vec{r}) \\
=\ & E_l C_{d'} f_{d'}(\vec{r}),
\end{aligned}
$$

where

$$
\overline{\overline{D}} \equiv \frac{\delta_{dd'}}{2m} + \frac{1}{m^2} \sum_\alpha \frac{\langle U_{d'} | \vec{P} | U_\alpha \rangle \langle U_\alpha | \vec{P} | U_d \rangle}{\epsilon_0 - \epsilon_\alpha},
$$

and

$$
\begin{aligned}
\overline{V} \equiv\ & \langle U_{d'} | \vec{P} | U_d \rangle + \sum_\alpha \frac{\langle U_{d'} | \vec{P} | U_\alpha \rangle \langle U_\alpha | \Delta V | U_d \rangle}{\epsilon_0 - \epsilon_\alpha} + \\
& \frac{\langle U_{d'} | \Delta V | U_\alpha \rangle \langle U_\alpha | \vec{P} | U_d \rangle}{\epsilon_0 - \epsilon_\alpha}.
\end{aligned}
\tag{A.11}
$$

$\Pi_{dd';l}$ is defined in Eq. (A.11). Π_l is called the *effective-mass Hamiltonian matrix.* In Eq. (A.11), there are no terms explicitly coupling f_d with f_α.

A.3 Hamiltonian matrix

In this section, we give explicitly matrix elements of submatrices Π_a, Π_b, and Π_c of Π for the zinc-blende structure. Since they are all Hermitian, only upper triangular matrices will be given.

Matrix elements of Π_a are in the following:

$$
(\Pi_a)_{11} = 2CsA'(N + \frac{1}{2}) + Cs(N + 1) + (A' + \frac{1}{2})Ck_z^2 +
$$

$$
\begin{aligned}
& \epsilon_c + \Delta\epsilon_c + \frac{1}{2} X N_m \alpha \langle S_z \rangle , \\
(\Pi_a)_{12} &= i P \sqrt{s}\, \hat{a}^\dagger + C \sqrt{s} B k_z \hat{a} , \\
(\Pi_a)_{13} &= i P \sqrt{s/3}\, \hat{a} - i C \sqrt{s/3} B k_z \hat{a}^\dagger , \\
(\Pi_a)_{14} &= P \sqrt{2s/3}\, \hat{a} - C \sqrt{2s/3} B k_z \hat{a}^\dagger , \\
(\Pi_a)_{22} &= -Cs \left[(\gamma_1 + \gamma_2)(N + \frac{1}{2}) + \frac{3}{2}\kappa \right] + (\gamma_2 - \frac{1}{2}\gamma_1) C k_z^2 + \\
& \epsilon_v + \Delta\epsilon_v + \frac{1}{2} X N_m \beta \langle S_z \rangle , \\
(\Pi_a)_{23} &= -\frac{1}{2} C s \sqrt{3} \left[(\gamma_2 - \gamma_3) \hat{a}^{\dagger 2} + (\gamma_2 + \gamma_3) \hat{a}^2 \right] , \\
(\Pi_a)_{24} &= i C s \sqrt{3/2} \left[(\gamma_2 - \gamma_3) \hat{a}^{\dagger 2} + (\gamma_2 + \gamma_3) \hat{a}^2 \right] , \\
(\Pi_a)_{33} &= -Cs \left[(\gamma_1 - \gamma_2)(N + \frac{1}{2}) - \frac{1}{2}\kappa \right] - (\gamma_2 + \frac{1}{2}\gamma_1) C k_z^2 + \\
& \epsilon_v + \Delta\epsilon_v - \frac{1}{6} X N_m \beta \langle S_z \rangle , \\
(\Pi_a)_{34} &= i C s \sqrt{2} \left[\gamma_2 (N + \frac{1}{2}) - \frac{1}{2}\kappa - \frac{1}{2} \right] - i \sqrt{2} \gamma_2 C k_z^2 - \\
& i \frac{\sqrt{2}}{3} X N_m \beta \langle S_z \rangle , \\
(\Pi_a)_{44} &= -Cs \left[\gamma_1 (N + \frac{1}{2}) - \kappa - \frac{1}{2} \right] - \frac{1}{2} \gamma_1 C k_z^2 - \Delta + \\
& \epsilon_v + \Delta\epsilon_v + \frac{1}{6} X N_m \beta \langle S_z \rangle . \qquad \text{(A.12)}
\end{aligned}
$$

Matrix elements of Π_b are in the following:

$$
\begin{aligned}
(\Pi_b)_{11} &= 2CsA'(N + \frac{1}{2}) + CsN + (A' + \frac{1}{2}) C k_z^2 + \\
& \epsilon_c + \Delta\epsilon_c - \frac{1}{2} X N_m \alpha \langle S_z \rangle , \\
(\Pi_b)_{12} &= i P \sqrt{s}\, \hat{a} - i C \sqrt{s} B k_z \hat{a}^\dagger , \\
(\Pi_b)_{13} &= i P \sqrt{s/3}\, \hat{a}^\dagger + i C \sqrt{s/3} B k_z \hat{a} , \\
(\Pi_b)_{14} &= P \sqrt{2s/3}\, \hat{a}^\dagger + i C \sqrt{2s/3} B k_z \hat{a} , \\
(\Pi_b)_{22} &= -Cs \left[(\gamma_1 + \gamma_2)(N + \frac{1}{2}) - \frac{3}{2}\kappa \right] + (\gamma_2 - \frac{1}{2}\gamma_1) C k_z^2 + \\
& \epsilon_v + \Delta\epsilon_v - \frac{1}{2} X N_m \beta \langle S_z \rangle , \\
(\Pi_b)_{23} &= -\frac{1}{2} C s \sqrt{3} \left[(\gamma_2 + \gamma_3) \hat{a}^{\dagger 2} + (\gamma_2 - \gamma_3) \hat{a}^2 \right] ,
\end{aligned}
$$

$$\begin{aligned}
(\Pi_b)_{2\,4} &= i\,Cs\sqrt{3/2}\left[(\gamma_2+\gamma_3)\hat{a}^{\dagger 2}+(\gamma_2-\gamma_3)\hat{a}^2\right],\\
(\Pi_b)_{3\,3} &= -Cs\left[(\gamma_1-\gamma_2)(N+\frac{1}{2})+\frac{1}{2}\kappa\right]-(\gamma_2+\frac{1}{2}\gamma_1)Ck_z^2+\\
&\quad \epsilon_v+\Delta\epsilon_v+\frac{1}{6}XN_m\beta\langle S_z\rangle,\\
(\Pi_b)_{3\,4} &= i\,Cs\sqrt{2}\left[\gamma_2(N+\frac{1}{2})+\frac{1}{2}\kappa+\frac{1}{2}\right]-i\,\sqrt{2}\gamma_2Ck_z^2+\\
&\quad i\frac{\sqrt{2}}{3}XN_m\beta\langle S_z\rangle,\\
(\Pi_b)_{4\,4} &= -Cs\left[\gamma_1(N+\frac{1}{2})+\kappa+\frac{1}{2}\right]-\frac{1}{2}\gamma_1Ck_z^2-\Delta\\
&\quad \epsilon_v+\Delta\epsilon_v-\frac{1}{6}XN_m\beta\langle S_z\rangle.
\end{aligned}\tag{A.13}$$

Matrix elements of Π_c are in the following:

$$\begin{aligned}
(\Pi_c)_{1\,3} &= \sqrt{\frac{2}{3}}Pk_z-\frac{1}{\sqrt{6}}CsB(\hat{a}^{\dagger 2}-\hat{a}^2),\\
(\Pi_c)_{1\,4} &= \frac{i}{\sqrt{3}}Pk_z-\frac{i}{2\sqrt{3}}CsB(\hat{a}^{\dagger 2}-\hat{a}^2),\\
(\Pi_c)_{2\,3} &= i\,C(\sqrt{6s})\gamma_3k_z\hat{a},\\
(\Pi_c)_{2\,4} &= -C(\sqrt{3s})\gamma_3k_z\hat{a},\\
(\Pi_c)_{3\,1} &= \sqrt{\frac{2}{3}}Pk_z,\\
(\Pi_c)_{3\,2} &= -i\,C(\sqrt{6s})\gamma_3k_z\hat{a},\\
(\Pi_c)_{3\,4} &= -3C(\sqrt{s})\gamma_3k_z\hat{a}^\dagger,\\
(\Pi_c)_{4\,1} &= -\frac{i}{\sqrt{3}}Pk_z,\\
(\Pi_c)_{4\,2} &= -C(\sqrt{3s})\gamma_3k_z\hat{a},\\
(\Pi_c)_{4\,3} &= -3C(\sqrt{s})\gamma_3k_z\hat{a}^\dagger.
\end{aligned}\tag{A.14}$$

We give the expressions of Δ, ϵ_c, Δ, ϵ_v, B, P, A$'$, γ_1, γ_2, γ_3, and κ which appear in Π matrix elements:

$$\begin{aligned}
\Delta\epsilon_c &= \langle S|\Delta V|S\rangle+\sum_{j\in\Gamma_1}\frac{|\langle S|\Delta V|U_j\rangle|^2}{\epsilon_c-\epsilon_j},\\
\Delta\epsilon_v &= \langle X|\Delta V|X\rangle+\sum_{j\in\Gamma_{15}}\frac{|\langle X|\Delta V|U_j\rangle|^2}{\epsilon_v-\epsilon_j},
\end{aligned}$$

$$\begin{aligned}
P &= \frac{-i\hbar}{m}\left[\langle S|P_z|Z\rangle + \sum_{j\in\Gamma_{15}} \frac{\langle S|P_z|U_j\rangle\langle U_j|\Delta V|Z\rangle}{\epsilon_0-\epsilon_j} + \right. \\
&\qquad \left. \sum_{j\in\Gamma_1} \frac{\langle S|P_z|U_j\rangle\langle U_j|\Delta V|Z\rangle}{\epsilon_0-\epsilon_j}\right], \\
A' &= \frac{1}{m}\sum_{j\in\Gamma_{15}} \frac{|\langle S|P_z|U_j\rangle|^2}{\epsilon_c-\epsilon_j}, \\
B &= \frac{2}{m}\sum_{j\in\Gamma_{15}} \left[\frac{\langle S|P_x|U_j\rangle\langle U_j|P_y|Z\rangle}{\epsilon_0-\epsilon_j}\right], \\
\gamma_1 &= -(F+2G+2H_1+2H_2)/3-1, \\
\gamma_2 &= -(F+2G-H_1-H_2)/6, \\
\gamma_3 &= -(F-G+H_1-H_2)/6, \\
\kappa &= -(F-G-H_1+H_2)/6-1/3,
\end{aligned}$$

where F, G, H_1 and H_2 are interband matrix elements:

$$\begin{aligned}
F &= \frac{1}{m}\sum_{j\in\Gamma_1} \frac{|\langle Z|P_z|U_j\rangle|^2}{\epsilon_v-\epsilon_j}, \\
G &= \frac{1}{2m}\sum_{j\in\Gamma_{12}} \frac{|\langle Z|P_z|U_j\rangle|^2}{\epsilon_v-\epsilon_j}, \\
H_1 &= \frac{1}{m}\sum_{j\in\Gamma_{15}} \frac{|\langle X|P_y|U_j\rangle|^2}{\epsilon_v-\epsilon_j}, \\
H_2 &= \frac{1}{m}\sum_{j\in\Gamma_{25}} \frac{|\langle X|P_y|U_j\rangle|^2}{\epsilon_v-\epsilon_j}.
\end{aligned} \tag{A.15}$$

Unfortunately, the symbol "B" here denotes, in accordance with the convention, a second-order purturbation matrix element rather than the magnetic field. Values of the above parameters are calculated with the knowledge of the empirical pseudopotential form factors and eigenfunctions of the reference Hamiltonian H_R.

A.4 Current Density Matrices

The current density matrix element between two bulk eigenstates is

$$\begin{aligned} & \int dy_0' \langle dk^A_{j^*,n} | j_z(\vec{r}_0) | d'k^B_{j',n'} \rangle_A \\ = & \frac{1}{N_x N_z \Omega} e^{i(k^B_{j'} - k^A_j) Z_0} \frac{1}{\hbar} \left[(H_2^a)_{dd'} (k_j^a + k_{j'}^b) \delta_{nn'} + (H_1^a)_{dd'} \delta_{nn'} \right. \\ & \left. - \triangle_{dd'} \delta_{m(d,n) m(d',n')} \right], \end{aligned}$$

where

$$\begin{aligned} \triangle_{dd'} = & \frac{\hbar}{m} \sum_\alpha \left[\frac{\langle U_d | P_z | U_\alpha \rangle \langle U_\alpha | \Delta V^B | U_{d'} \rangle}{\epsilon_0 - \epsilon_\alpha} \right. \\ & \left. + \frac{\langle U_d | \Delta V^A | U_\alpha \rangle \langle U_\alpha | P_z | U_{d'} \rangle}{\epsilon_0 - \epsilon_\alpha} \right]. \end{aligned} \tag{A.16}$$

Here, $m(d,n)$ represents the index of the harmonic oscillator function in $|dk_{j,n}\rangle$.

To calculate the matrix $\int dy_0' \langle d'k^A_{j',n'} | j_z(\vec{r}_0) | dk^A_{j^*,n} \rangle$, we simply set the last term in Eq. (A.16) to zero. The matrix $\int dy_0' \langle d'k^B_{j',n'} | j_z(\vec{r}_0) | dk^B_{j^*,n} \rangle$ is similarly calculated. The matrix $\int dy_0' \langle d'k^B_{j',n'} | j_z(\vec{r}_0) | dk^A_{j^*,n} \rangle$ is found by taking the complex conjugate of $\int dy_0' \langle dk^A_{j^*,n} | j_z(\vec{r}_0) | d'k^B_{j',n'} \rangle$. In the following we give nonzero $\triangle_{dd'}$ explicitly:

$$\begin{aligned} \langle U_1 | \triangle | U_6 \rangle &= \frac{-2}{\sqrt{6}} \ominus, \\ \langle U_6 | \triangle | U_1 \rangle &= \frac{2}{\sqrt{6}} \oplus, \\ \langle U_2 | \triangle | U_5 \rangle &= \frac{-2}{\sqrt{6}} \ominus, \\ \langle U_5 | \triangle | U_2 \rangle &= \frac{2}{\sqrt{6}} \oplus, \\ \langle U_1 | \triangle | U_8 \rangle &= \frac{-i}{\sqrt{3}} \ominus, \\ \langle U_8 | \triangle | U_1 \rangle &= \frac{-i}{\sqrt{3}} \oplus, \\ \langle U_2 | \triangle | U_7 \rangle &= \frac{-i}{\sqrt{3}} \ominus, \\ \langle U_7 | \triangle | U_2 \rangle &= \frac{-i}{\sqrt{3}} \oplus, \end{aligned}$$

$$
\begin{aligned}
\langle U_3|\triangle|U_5\rangle &= \frac{-1}{\sqrt{3}}\odot, \\
\langle U_5|\triangle|U_3\rangle &= \frac{1}{\sqrt{3}}\odot, \\
\langle U_3|\triangle|U_7\rangle &= \frac{2i}{\sqrt{6}}\odot, \\
\langle U_7|\triangle|U_3\rangle &= \frac{2i}{\sqrt{6}}\odot, \\
\langle U_4|\triangle|U_6\rangle &= \frac{1}{\sqrt{3}}\odot, \\
\langle U_6|\triangle|U_4\rangle &= \frac{-1}{\sqrt{3}}\odot, \\
\langle U_4|\triangle|U_8\rangle &= \frac{-2i}{\sqrt{6}}\odot, \\
\langle U_8|\triangle|U_4\rangle &= \frac{-2i}{\sqrt{6}}\odot,
\end{aligned}
\tag{A.17}
$$

where

$$
\begin{aligned}
\oplus &= -2\frac{i\hbar}{m}\sum_{\alpha\in\Gamma_1}\left[\frac{\langle Z|P_z|U_\alpha\rangle\langle U_\alpha|\Delta V^A|S\rangle}{\epsilon_0-\epsilon_\alpha}\right], \\
\ominus &= 2\frac{i\hbar}{m}\sum_{\alpha\in\Gamma_{15}}\left[\frac{\langle S|P_z|U_\alpha\rangle\langle U_\alpha|\Delta V^A|Z\rangle}{\epsilon_0-\epsilon_\alpha}\right], \\
\odot &= 2\frac{i\hbar}{m}\sum_{\alpha\in\Gamma_{15}}\left[\frac{\langle X|P_y|U_\alpha\rangle\langle U_\alpha|\Delta V^A|Z\rangle}{\epsilon_v-\epsilon_\alpha}\right].
\end{aligned}
\tag{A.18}
$$

By letting $\odot = 0$, the function $\delta_{m(d,n),m(d',n')}$ in Eq. (A.16) becomes $\delta_{nn'}$. Hence,

$$
\begin{aligned}
&\int dy_0'\langle dk^A_{j^*,n}|j_z(\vec{r}_0)|d'k^B_{j',n'}\rangle_A \\
&= \frac{1}{N_xN_z\Omega}e^{i(k^B_{j'}-k^A_j)Z_0}\frac{1}{\hbar}\left[(H_2^a)_{dd'}(k_j^a+k_{j'}^b)+(H_1^a)_{dd'}-\triangle_{dd'}\right]\delta_{nn'}.
\end{aligned}
\tag{A.19}
$$

Appendix B

Derivation of Inelastinc Tunneling Current in a GaAs-AlAs-GaAs-AlAs-GaAs Structure

B.1 Introduction

In this appendix, we derive the expression for inelastic tunneling current in a GaAs-AlAs-GaAs-AlAs-GaAs structure. The inelastic tunneling considered here is induced by barrier phonon excitation. Upper limits of the tunneling current will be given. In Section (B.2), we present the derivation.

B.2 Derivation

We start with the expression for the current:

$$J_{in} = \frac{4\pi e}{\hbar} \sum_{\vec{q}\lambda} \sum_{\vec{k}} \sum_{\vec{k\prime}} |M|^2 f(\epsilon_k)[1 - f(\epsilon_{k\prime})]\delta(\epsilon_k + eV_a - \epsilon_{k\prime} - \hbar\omega) \tag{B.1}$$

at zero temperature. Replacing $\sum$ with $\int$, we have

$$\begin{aligned} J_{in} &= \frac{4\pi e}{\hbar} A \sum_{\lambda} \frac{V_{AlAs}}{(2\pi)^3} \int d^3q \frac{V}{(2\pi)^3} \int d^3k \frac{V}{(2\pi)^3} \int d^3k' |M|^2 f(\epsilon_k)[1 - f(\epsilon_{k'})] \\ &\times \quad \delta(\vec{k}_{\|} - \vec{k'}_{\|} - \vec{q}_{\|})(2\pi)^2 \delta(\epsilon_k + eV_a - \epsilon_{k'} - \hbar\omega) \\ &= \frac{4\pi e}{\hbar} A \sum_{\lambda} \int \frac{d^3q}{(2\pi)^3} |U_q|^2 \int \frac{d^3k}{(2\pi)^3} \int \frac{d^3k'}{(2\pi)^3} |T(q_{\perp}; k_{\perp}, k'_{\perp})|^2 f(\epsilon_k)[1 - f(\epsilon_{k'})] \\ &\times \quad \delta(\vec{k}_{\|} - \vec{k'}_{\|} - \vec{q}\|)(2\pi)^2 \delta(\epsilon_k + eV_a - \epsilon_{k'} - \hbar\omega). \end{aligned} \tag{B.2}$$

Here, we have

$$U_q = 4\pi e[\hbar\omega(1/\epsilon_0 - 1/\epsilon_{\infty})/8\pi]^{1/2}/q, \tag{B.3}$$

for polar optical coupling of an electron with an optical phonon, and

$$U_q = D_{\Gamma}(\hbar q/2\rho v_s)^{1/2}, \tag{B.4}$$

for deformation-potential coupling of an electron and an acoustical phonon. T is the overlap integral

$$T(q_{\perp}; k_{\perp}, k'_{\perp}) = \int_{x_1}^{x_2} e^{iq_{\perp}x} \chi_l^* \chi_r dx. \tag{B.5}$$

Substituting the expressions for χ_l and χ_r, we obtain

$$\begin{aligned} |T|^2 &= \frac{2k_r k_l}{m^* \kappa_r \kappa_l} e^{-\kappa_T d_1} \frac{\cosh(\kappa_D d_1) - \cos(q_{\perp} d_1)}{\kappa_D^2 + q_{\perp}^2} \times \\ & \frac{1}{[\sin(k_w w)]^2 e^{-2\kappa_2 d_2} + [4\cos(k_w w)]^2 e^{2\kappa_2 d_2}}, \end{aligned} \tag{B.6}$$

where $\kappa_D = \kappa_l - \kappa_r$ and $\kappa_T = \kappa_l + \kappa_r$. For the electron with its energy near the resonant level, the factor

$$\frac{1}{[\sin(k_w w)]^2 e^{-2\kappa_2 d_2} + [4\ cos(k_w w)]^2 e^{2\kappa_2 d_2}} \tag{B.7}$$

in $|T|^2$ can be approximated by a δ function

$$\frac{E_1}{2} \delta(\epsilon_{k'_{\perp}} - \frac{eV_a}{2} - E_1), \tag{B.8}$$

where E_1 is the energy of the first quasi-bound level in the well which is approximately equal to $\pi^2\hbar^2/2m^*w^2$.

Now, following Bennett et al[1], we make the approximation

$$\frac{\cosh(\kappa_D d_1) - \cos(q_\perp d_1)}{\kappa_D^2 + q_\perp^2} \approx \frac{1}{2}d_1^2 \tag{B.9}$$

asumming both $\kappa_D d_1$ and $q_\perp d_1$ are small. For the cases where the assumption of $k_D d_1$ being small does not hold, the approximation underestimates the value of $|T|^2$ and therefore J_{in}. Furthermore, to be consistent with the assumption that $q_\perp d_1$ is small, we shall confine the calculation of the integral over $q_\perp$ in such domain that $|q_\perp| \leq d_1^{-1}$. In so doing, we again underestimate J_{in}. However, for mose cases of interest, the former approximation would result in reasonable estimate of order of magnitude of J_{in}.

In the calculation of the integral of j_{in}, κ_T is evaluated by expanding κ_l and κ_r about the zero energies of the two electrodes. We assume the effective barrier heights seen by the electron are $E_{b;L} = E_b - eV_a/4$ for the left barrier, and $E_{b;R} = E_b + eV_a/4$ for the right barrier, for a symmetric structure with zero bias barrier height E_b. Then

$$\kappa_T \approx 2\kappa_0 - (\epsilon_{k_\perp} + \epsilon_{k'_\perp} - eV_a/2)\kappa_0/2E_b, \tag{B.10}$$

where

$$\begin{aligned}
\epsilon_{k_\perp} &= \hbar^2 k_\perp^2/2m^*,\\
\epsilon_{k'_\perp} &= \hbar^2 k'^2_\perp/2m^*,\\
\kappa_0 &= \sqrt{2m^*E_b/\hbar^2}.
\end{aligned} \tag{B.11}$$

After we integrate over d^3k', we get

$$\begin{aligned}
j_{in} &= \frac{2Aem^{*2}d_1^2}{(2\pi)^3\hbar^5\kappa_0^2}e^{-2\kappa_0 d_1}e^{E_1/V_b}\sum_\lambda \int \frac{d^3q}{(2\pi)^3}|U_q|^2 \int d^2k_\| \int_0^\infty d\epsilon_{k\perp}e^{\epsilon_{k\perp}/V_b}\\
&\times \frac{E_1}{2}\delta(\epsilon_k + eV_a/2 - \hbar\omega - \hbar^2(\vec{k}_\| - \vec{q}_\|)^2/2m^* - E_1)f(\epsilon_k),
\end{aligned} \tag{B.12}$$

where $V_b = 2E_b/\kappa_0 d_1$. Using the fact that $e^{2\epsilon_{k\perp}/V_b} \approx 1$ for interesting cases, and integrating over $d\epsilon_{k\perp}$, we obtain

$$\begin{aligned} j_{in} &= \frac{2Aem^2_{AlAs}d_1^2}{(2\pi)^3\hbar^5\kappa_0^2} e^{-2\kappa_0 d_1} e^{E_1/V_b} \sum_\lambda \int \frac{d^3q}{(2\pi)^3}|U_q|^2 \int d^2k_\parallel \\ &\times \frac{E_1}{2}\Theta\{[k_F^2 + q_0^2 - (\vec{k}_F - \vec{q}_\parallel)^2] - [k_\parallel^2 + q_0^2 - (\vec{k}_\parallel - \vec{q}_\parallel)^2]\}, \quad \text{(B.13)} \end{aligned}$$

where q_0 satisfies $\hbar^2 q_0^2/2m^* = eV_a/2 - \hbar\omega - E_1$. Θ is the step function. The integral over $d^2k_\parallel$ can be treated as follows:

$$\begin{aligned} \int k_\parallel dk_\parallel \int_0^{2\pi} d\phi(...) &= 2\int k_\parallel dk_\parallel \int_{-1}^{1} \frac{d[\cos(\phi)]}{\sin(\phi)}(...) \\ &\geq 2\int k_\parallel dk_\parallel \int_{-1}^{1} d[\cos(\phi)](...) \qquad \text{(B.14)} \end{aligned}$$

since the integrand is nonnegative. The integral over $d\phi$ on the right side of the inequality can be evaluated analytically and results in a function $G(k_\parallel, q_\parallel)$. Thus we are left with an integral over d^3q and $dk_\parallel$

$$\int d^3q|U_q|^2 \int k_\parallel dk_\parallel G(k_\parallel, q_\parallel) \approx 2\int dq_\perp |U(q_\parallel = q_0, q_\perp)|^2 k_F^4. \qquad (B.15)$$

For PO coupling, we have

$$\begin{aligned} J_{in} &\geq \frac{2Aem^{*2}d_1^2}{(2\pi)^3\hbar^5\kappa_0^2} e^{-2\kappa_0 d_1} e^{E_1/V_b} \frac{E_1}{2} \times \\ &\quad \frac{2}{\pi} e^2\hbar\omega \frac{k_F^4}{q_0}(1/\epsilon_0 - 1/\epsilon_\infty) tan^{-1}(1/q_0 d_1). \qquad \text{(B.16)} \end{aligned}$$

For DP coupling, we have

$$\begin{aligned} J_{in} &\geq \frac{2Aem^{*2}d_1^2}{(2\pi)^3\hbar^5\kappa_0^2} e^{-2\kappa_0 d_1} e^{E_1/V_b} \frac{E_1}{2} \frac{\pi k_F^4}{2\pi^2} \frac{D_\Gamma^2\hbar}{2\rho v_s} \times \\ &\quad \{d_1^{-1}(d_1^{-2} + q_0^2)^{1/2} + q_0^2 \sinh^{-1}[(q_0 d_1)^{-1}]\}. \qquad \text{(B.17)} \end{aligned}$$

References

1. A. J. Bennett, C. B. Duke, and S. D. Silverstein, Phys. Rev. Vol 176, No. 3, 969 (1968).